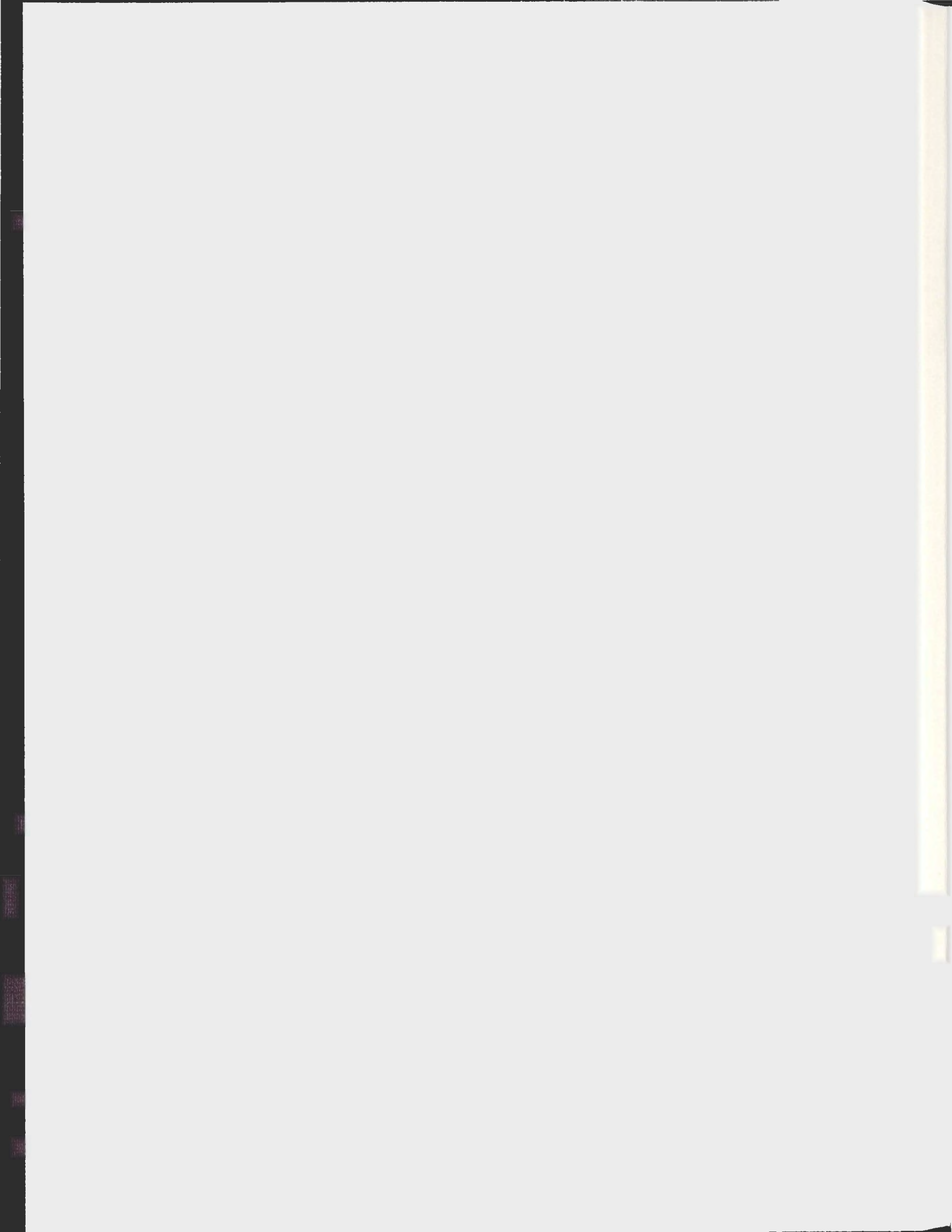


SEISMIC BEAMFORMING

SHERVIN GHOLAM AZAD



SEISMIC BEAMFORMING

by

© Shervin Gholam Azad

A Thesis submitted to the

School of Graduate Studies

in partial fulfillment of the requirements for the degree of

Master of Science

Department of Earth Sciences

Faculty of Science

Memorial University of Newfoundland

November 9, 2012

St. John's

Newfoundland

Abstract

The mining industry currently faces decreasing numbers of mineral discoveries at shallow depths. As a result, mining companies are intent on finding new methods to discover deposits which lie deeper (>500 m) and are out of reach of other conventional geophysical techniques. The possibility of adapting seismic techniques to incorporate mineral exploration has recently been considered. The use of seismic beam-forming could potentially significantly diminish exploration costs for deeper targets. An approach to decreasing the cost of the seismic technique is to significantly decrease the source cost by relaxing the imaging requirement of complete azimuthal illumination of the target. In this work, we employ a method to beam-form scattered energy and optimally detect and map geological targets. For each subsurface grid point, we compute a delay and sum operation that is designed to focus diffraction energy, assuming that the point is a candidate for causing a diffraction event. We demonstrate the benefits of this approach by applying it to both synthetic and real seismic data in which targets at different depths are present. Overall, the results obtained from both synthetic and real field data show that seismic beam-forming could be an effective method for locating ore deposits. Successful application of this method could prove successful in reducing exploration costs.

Acknowledgement

This dissertation would not have been possible without the guidance and the help of several individuals who in one way or another contributed and extended their valuable assistance in the preparation and completion of this study. First and foremost, my utmost gratitude to my supervisor Dr.Charles Hurich for providing me with the opportunity continuing my studies at Memorial University and allowing me the freedom to explore this new area of seismology.

I would like to thank Dr.Sharon Deemer for all her technical advice. I would also like to thank Dr.Phil Bording for giving me the initial opportunity to study at Memorial University.

Last but not the least; I would like to thank my parents and my wife Parvaz for their endless support.

Contents

Contents.....	i
List of Figures.....	v
List of Symbols.....	x
Introduction.....	1
1.1. Application of Seismology in Mineral Exploration	1
1.1.1. Seismic Exploration for Minerals – Special Considerations	3
1.2. Thesis Objective	3
1.3. Thesis organization.....	4
Array Design	6
2.1. Introduction.....	6
2.2. Array Application.....	6
2.3. Array Resolution	7
2.4. Spatial Aliasing.....	8
2.5. Near-field and Farfield Region	8
2.5.1. Far-field Array Response	10
2.6. Potential Array Configuration	10
2.7. Description of MATLAB Code	11
2.8. Simulation.....	12
2.9. Comparison of Different Arrays Based on Number of Receivers.....	21
2.10. Summary	22
Beam-Forming.....	23
3.1 Introduction.....	23
3.2 Conventional Beam-forming	23
3.2.1 Time-domain Beam-forming	25
3.2.2 Frequency-Domain Beam-forming.....	26
3.3 Near-field Beamformer	28
3.3.1 Diffraction.....	29
3.3.1.1 Diffraction Equation	31
3.3.2 Characteristics of Diffraction.....	32
3.4 Description of the Method.....	34

3.4.1	Explaining the Method in Detail.....	35
3.4.2	Identifying the Matrix Elements Relevant to the Diffraction.....	37
3.4.2.1	First Example	38
3.4.2.2	Coincident source-target and offset source-target Example	41
3.4.3	Temporal Samples	42
3.5	Criteria for Evaluating the Beamformer	43
3.5.1	Degree of Localization.....	44
3.5.2	Beamwidth	44
3.5.2.1	Beam-width vs Target Size	44
3.5.2.2	Beam-width vs Depth.....	45
3.5.2.3	Fresnel zone vs Depth	46
3.4	Difference between Migration and this Method	47
3.7	Summary	48
	Beam-former Performance	49
4.1.	Introduction.....	49
4.2.	Synthetic Data Generation	49
4.2.1.	Processing of the Data.....	50
4.2.1.1	Trace Muting	50
4.2.1.2	Band-pass Filtering.....	50
4.2.2	Description of MATLAB Code	51
4.2.3	Synthetic Data Generation and MATLAB Code for Vertical Seismic Profiling DATA.....	52
4.3	Evaluation of the Beam-formers Response for Surface Profiling.....	53
4.3.1.	Studied Parameters.....	53
4.3.2.	Test 1: Source and target at the centre of the array.....	54
4.3.3.	Test 2: Target offset from the source which is at the centre of the array	58
4.3.4.	Source is at the centre of, the shapes and sizes of the target are variable.....	60
4.3.4.1.	Test 3: Rectangular target(400 by 50).....	61
4.3.4.2.	Test 4: Square Scatterer (200 by 200 m).....	63
4.3.4.3.	Test 5: Triangle Model.....	65
4.3.4.4.	Test 6: Lens-Shape Scatterer with 40 Degrees Dip	67
4.3.5.	Horizontal & Vertical Detection Abilities of Beam-former.....	69
4.3.5.1.	Test 7: 600 m Horizontal Distance	69

4.3.5.2.	Test 8: 200 m Horizontal Distance	73
4.3.5.3.	Test 9: 50 m Distance	75
4.3.5.4.	Test 10: 50 m Vertical Distance	77
4.3.5.5.	Test 11: 30 m Vertical Distance	79
4.3.6.	Gap Along the Array Line.....	81
4.3.6.1.	Test 12: Random Gaps Along the Array	82
4.3.6.2.	Test 13: Obstruction to Record Apex of the Hyperbola.....	83
4.3.7.	Affects of Noise on Beam Performance	84
4.3.7.1.	Description of MATLAB Code	84
4.3.7.2.	Signal-to-Noise Ratio	86
4.3.7.3.	Beam-former Performance on Data with Noise.....	87
4.3.7.3.1.	Test 14	88
4.3.7.3.2.	Test 15	89
4.3.7.3.3.	Test 16	90
4.3.7.3.4.	Test 17	91
4.3.7.3.5.	Test 18	92
4.3.7.3.6.	Test 19	93
4.3.8.	Shifts Along Hyperbola	94
4.3.8.1.	Test 20	95
4.3.8.2.	Test 21	96
4.3.8.3.	Test 22	97
4.3.8.4.	Test 23	98
4.3.9.	Test 24: Combination of Shift and Noise.....	99
4.3.10.	Test 25: When There Are Obstructions Along the Line.....	100
4.3.11.	Test 26: Closest Model to Real Situation	101
4.4.	Experimental Results on Vertical Seismic Profiling Data	102
4.4.1.	Test 27: Beam-former Performance on VSP Data	102
4.5.	Field Data Example	104
4.5.1.	Velocity Analysis	104
4.5.2.	Test 28: Shot Gather from VSP Data.....	105
4.5.3.	Test 29: Stacked Data Example.....	107

4.6. Summary..... 113
Conclusion and Recommendation114
5.1. Conclusion114
5.2. Recommendation for Future Research115
Bibliography.....116
Appendix A118
Appendix B123
Appendix C126
Appendix D127

List of Figures

Figure 1: Example of beam-pattern of a uniform linear array. The main beam, side lobes and the width of the main beam are pointed out modified from (Lundstrom, 2008).	7
Figure 2: Illustration of the near-field and far-field scatterer (Moffat, 2002).	9
Figure 3: Schematic showing depth-arraylength bounds for near-field and far-field.	9
Figure 4: Array response of 1-D array. This is the power spectrum of the array.	11
Figure 5: 2-D array (it includes 1089 receivers. There is a 5 meter interval between receivers)	13
Figure 6: 2-D array response of square pattern with uniform spacing. That is used as the reference for evaluating other array configurations. The required number of geophones are 1089 for the covered area (102400 m ²).	13
Figure 7: Star pattern geometry	14
Figure 8: Array response of star pattern. Side-lobes are significant in comparison with the square array, but proportion of the main-lobe to side-lobe is acceptable. Ratio between amplitude of highest side-lobe to main-lobe is 0.01632.	14
Figure 9: Circle pattern geometry	15
Figure 10: Array response of circle pattern (Ratio between amplitude of highest side-lobe to main-lobe is 0.1209)	15
Figure 11: Triangle geometry	16
Figure 12: Triangle Pattern and its array response (Ratio between amplitude of highest side-lobe to main-lobe is 0.5883)	16
Figure 13: Cross pattern geometry	17
Figure 14: Cross Pattern and its array response (Ratio between amplitude of highest side-lobe to main-lobe is 0.2424)	17
Figure 15: Random pattern geometry	18
Figure 16: Random Pattern and its array response (Ratio between amplitude of highest side-lobe to main-lobe is 0.2641)	18
Figure 17: Square array geometry. In this array the space between square lines progressively increased. The main reason for choosing this configuration is recording the higher frequencies by the center and lower frequencies by receivers far from the centre. By this configuration, we also implement fewer of receivers in comparison with the square pattern.	19
Figure 18: Progressive square Pattern array response (Ratio between amplitude of highest side-lobe to main-lobe is 0.1062)	19
Figure 19: combined circle and star pattern geometry	20
Figure 20: Combination of star and circle pattern and its array response (Ratio between amplitude of highest side-lobe to main-lobe is 0.04445)	20
Figure 21: Basic delay schematic. When the signals arrive at the receivers orthogonally the maximum can be seen at $Kx = 0$, but when the signals coming from different angle at the same receiver we get different result. If the delays apply to receivers, the maximum will be shifted.	24
Figure 22: Linear array showing and 1-D delay calculation.	24

Figure 23: A general form of a time domain beam-former x_m, τ_m are input and time delay respectively and W_m is the amplitude weight of the m th receiver. Modified from (Dudgeon et al., 1984) and (Moffat, 2002)26

Figure 24: A general form of a frequency domain beam-former. The first step in this design is that each input data stream is transformed from the time domain to the frequency domain via the fast Fourier transform (FFT). The last step to get the beam-former output is to apply the inverse transform to the processed FFT vector to obtain time samples once again. The beam-former weights in this case are complex (Allred, 2006).27

Figure 25: (a) Represents a single-point in-homogeneity in the earth, returning seismic energy from a source at the surface to an adjacent geophone, and (b) represents the corresponding signature on the time section.30

Figure 26: Diffraction travel time curve for a coincident source and scatterer. Since the direct wave, which arrives first at the receiver array, had higher amplitude than the diffractions, it was muted out to enhance visualization of the low energy diffraction.30

Figure 27: Geometry of a source (a) coincident with the scatterer, and (b) offset from the scatterer.31

Figure 28: The basic model.33

Figure 29: (a) Synthetic shot gather from the same model in the depth of 600 (m). The location of source for the left model is on the middle of the survey (600 m) and for the right one is on the beginning (0 m). The arrows show the apexes. (b) The lateral position of the apex did not change when the source position was changed, but the shape of the hyperbola and vertical position of the apex was changed. As long as we don't have any prior information about the target position in respect to the source, we could use surface data to detect the target horizontally and VSP data to detect the target vertically.33

Figure 30: a) Shot gather example before applying beam-forming b) this figure shows an example of a beam-power image.34

Figure 31: (a), (c) and (e) are the schematic of the shot-gather and show diffraction response. (b), (d) and (f) are the schematic of the idealized beam-forming results.36

Figure 32: Defined windows for three different hypothetical apexes in various depths. The hyperbolic windows were designed to appropriately cover the scatterer's hyperbola in shot gather sections. As it is shown in the diagram, windows become flatter when the time increases.38

Figure 33: (a) The target is at the depth of 600 m, (b) shot gather from the model (a), (c) is the result of the described method, and (d) is the zoom of specified area of (c).39

Figure 34 : One dimensional Beam40

Figure 35: The basic model (the shot gather for this model can be seen in Figure 29).....41

Figure 36: Result of developed beamforming method from (a) source and target are not coincident (b) coincident source and target.41

Figure 37: The results of beam-former with different elements in time direction for the target at the depth of 250 m.43

Figure 38: Beam-width vs target size graph. Fresnel radius for this specific example at the depth of 250 m is 106 m. As can be seen in the diagram the beam width doesn't change for target size less than Fresnel zone, but start increasing when the size of the target is bigger than Fresnel radius and it is apparently a linear relationship.45

Figure 39: Beam-width vs Depth. Relationship between beam-width and depth is non-linear.46

Figure 40: Fresnel zone vs Depth diagram. FZ increased non-linearly with depth.	46
Figure 41: Left) Top mute was applied to remove first arrivals. Right) Band-pass filtered version.	51
Figure 42:(a)Image showing a square scatterer. The white background represents the host rock (velocity=4.5 Km/s), the black shape represents an ore body (velocity=6.5 Km/s), and the red star is the source. This model is designed in Seismic Unix, (b) it is a shot gather, and (c) the result of the method. (d) The specified part of the part c is zoomed in to show the method could detect top and bottom of the target.	55
Figure 43: (e) & (f) 1-D representation of beam from top and bottom of the target respectively.	56
Figure 44: (a) Image showing a square scatterer. The white background represents the host rock (velocity = 4.5 Km/s), the black shape represents an ore body (velocity = 6.5 Km/s), and the red star is the source. This model is designed in Seismic Unix, (b) it is a shot gather, and (c) the result of the method. (d) & (e) 1-D representation of beam from top and bottom of the target respectively.	57
Figure 45: (a) Image showing a square scatterer. The white background represents the host rock (velocity=4.5 Km/s), the black shape represents an ore body (velocity=6.5 Km/s), and the red star is the source. This model is designed in Seismic Unix, (b) it is a shot gather, and (c) the result of the method.(d)&(e) 1-D representation of beam from top and bottom of the target respectively.	59
Figure 46: In this example target's dimension is 400 m by 50 m.	61
Figure 47: (a) The color version of the shot gather. Note the high amplitudes in the middle of the shot gather. (b) Result of beam-former. As can be seen in the Figure the top and bottom of the reflector are detected. In addition, if you look at two sides of the result you could see the diffraction results from edges of the target.	62
Figure 48: It is 1-D result from top of the target in to see how the response looks.	62
Figure 49: In this example the target's dimension is 200 by 200 m.	63
Figure 50: (a) The color version of the shot gather.(b) Result of beam-former. The top and bottom of the target can be distinguished in this figure.	64
Figure 51: This figure shows 1-D beam from top and bottom of the 200 by 200 m rectangular model and shows us the spatial resolution.	64
Figure 52: Triangle model in the depth of 400 m.	65
Figure 53: (a) shot gather from triangle model. (b) Beam-forming result from triangle model.	66
Figure 54: This Figure shows 1-D representation of the triangle model and shows us the spatial resolution.	66
Figure 55: Lens-Shape Scatterer with 40 Degrees Dip.	67
Figure 56: (a) Shot gather (color version) and (b) beam-former result.	67
Figure 57: 1-D representation of the target.	68
Figure 58: in this model, two separated target by the distance of 600 m can be seen.	69
Figure 59: Shot gather from the model in Figure 58. It is predictable as long as the recorded hyperbolas are separated it is expected that the beam-former works well.	70
Figure 60: beam-forming result could be seen in this figure. As you can see the two targets distinguished as we expect from the calculation was made before starting application of beam-former.	71
Figure 61: Geometry of two similar geological models representing adjacent massive sulfide deposits in the Moffat's experiment.	72

Figure 62: Beam-former response from Moffat's examples (2002). Beamformer couldn't resolve the targets.	72
Figure 63: In this model, two targets separated by the distance of 200 m can be seen	73
Figure 64: shot gather	73
Figure 65: As it is obvious from the beam-former result, two targets are detectable. Figure 66: 1-D representation from top of the targets. Two targets are separately detected. The power difference is also because of the different distances of the targets from the source.	74
Figure 67: In this example, the targets are closer together and the distance between them is 50(m) (30% of the Fresnel zone) so according to the definition of the horizontal resolution, we could not separate them.	75
Figure 68 a) shot gather (color version). b) the result shows the beam-former detects two separated target as one longer rectangular target.	75
Figure 69: 1-D representation from top of the Figure 68 (b).....	76
Figure 70: in this model two targets have 50 m depth difference.	77
Figure 71: Left) Shot gather from the model. Right) two targets were detected by beam-former. The dashed line is the part of 1-D representation shown in the next Figure.	78
Figure 72: 1-D representation from middle of the shot gather and beam-power in Figure 71 to show the targets are distinguishable. Both top and bottom of the targets can be seen in the graph.	78
Figure 73: in this model the depth difference is 30 m, which is close to the $\lambda/4$	79
Figure 74: left) Shot gather from the model in Figure 73. Right) two targets were detected by beam-former. The dashed line is the part of 1-D representation shown in the next Figure.....	80
Figure 75: 1-D representation from middle of the shot gather and beam-power in Figure 74 to show the targets are distinguishable. Both top and bottom of the targets can be seen in the graph.	80
Figure 76: In this cartoon some limitations along array were shown (black triangles are receivers).....	81
Figure 77: there are a few areas in which no data is recorded	81
Figure 78 (a) Shot gather. (b) beam-forming image could be seen in this figure. Top and bottom of the target was detected. (c) The 1-D representation of the top of the target.	82
Figure 79: (a) Shot gather. (b) beam-forming image could be seen in this figure. Top and bottom of the target was detected. (c),(d) The 1-D representation of the top and bottom of the target respectively.	83
Figure 80: In this figure, the effect of adding Gaussian noise in the simple example was shown.	85
Figure 81: Model before adding Gaussian noise after adding Gaussian noise	85
Figure 82: a) signal plus Gaussian noise b) Signal c) Noise	86
Figure 83: Trough white windows signal calculated from left figure and noise calculated from right figure. The window used to determine signal-to-noise ratio is consistent for all examples and is 180 ms in time axis and 1196 m in length. The chosen window includes the signal completely.	87
Figure 84: (a) shot gather (b) beam-former image (c) & (d) 1-D representation of beam from top and bottom of target respectively.....	88
Figure 85: (a) shot gather (b) beam-former image (c) & (d) 1-D representation of beam from top and bottom of target respectively.....	89
Figure 86: (a) shot gather (b) beam-former image (c) & (d) 1-D representation of beam from top and bottom of target respectively.....	90
Figure 87: (a) shot gather (b) beam-former image (c) 1-D representation of beam from top of target. ...	91

<i>Figure 88: (a) shot gather (b) beam-former image (c) & (d) 1-D representation of beam from top and bottom of target respectively.....</i>	<i>92</i>
<i>Figure 89: (a) shot gather (b) beam-former image (c) & (d) 1-D representation of beam from top and bottom of target respectively.....</i>	<i>93</i>
<i>Figure 90: (a) shot gather (b) beam-former image (c) 1-D representation of beam from top of the target.</i>	<i>95</i>
<i>Figure 91 : (a) shot gather (b) beam-former image (c) 1-D representation of beam from top of the target.</i>	<i>96</i>
<i>Figure 92: (a) shot gather (b) beam-former image (c) 1-D representation of beam from top of the target.</i>	<i>97</i>
<i>Figure 93: (a) shot gather (b) beam-former image (c) 1-D representation of beam from top of the target.</i>	<i>98</i>
<i>Figure 94: (a) shot gather (Noise added to data) (b) beam-former image (c)1-D representation of beam from top of the target.</i>	<i>99</i>
<i>Figure 95: (a) shot gather (Noise added to data) (b) beam-former image (c) 1-D representation of beam from top of the target.</i>	<i>100</i>
<i>Figure 96: (a) Primary model (b) shot gather after adding noise (c) Beam-forming image. Five targets could be detected in this figure.</i>	<i>101</i>
<i>Figure 97: In this example target's dimension is 50 by 50 m. The black line represents borehole. The receiver spacing is 4 m.</i>	<i>102</i>
<i>Figure 98 (a) Shot gather (b)This figure is the result of beam-forming on the VSP data. The high power can be seen on left and right of the target. To find the location of the target, it is better to look at the two dimensional spectrum on left and right of the target.</i>	<i>103</i>
<i>Figure 99: The ratios of main-lobe to side-lobes are fairly acceptable and there is no problem to find the maximum position of the main-lobe.</i>	<i>103</i>
<i>Figure 100: VSP Shot gather.....</i>	<i>105</i>
<i>Figure 101: In this set of Figures, the results of beam-former on the VSP data with the velocities of 2000, 3100, 3400, and 4400 m/s are shown.</i>	<i>106</i>
<i>Figure 102: stacked section. The diffraction hyperbola can barely be seen as indicated.</i>	<i>107</i>
<i>Figure 103: The code was run for various velocities: 1000, 1500, 2000, 3000, 4000 and 5000 m/s.....</i>	<i>109</i>
<i>Figure 104: Fine search for finding the best velocity for detecting the target.</i>	<i>111</i>
<i>Figure 105: stack data and beam-forming result.</i>	<i>112</i>
<i>Figure 106: 1-D representation of beam from top of the target.</i>	<i>113</i>

List of Symbols and Abbreviations

FFT Fast Fourier Transform

CMP Common Mid_point Gather

Fz Fresnel Zone

Chapter 1

Introduction

1.1. Application of Seismology in Mineral Exploration

Seismic methods illuminate the subsurface using elastic waves. The signals of interest arise from the reflection, refraction and scattering of waves at boundaries where abrupt changes in elastic properties occur. Seismic reflection techniques have been used extensively for oil and gas exploration in sedimentary basins. Through geological imaging, these techniques help identify the location and size of oil and natural gas fields. Seismic methods have had relatively limited use in mineral applications. This is due, in part, to relatively high cost of seismic techniques, but is predominantly the result of the complexity of the seismic response in the hard rock environment. However, recent results indicate that seismic methods can be adapted for use in mining exploration, though some modifications to standard practice are required in view of the complex scattering and weak reflectivity that characterizes seismic data from ore deposits. Early application and recent developments in the mining industry can be seen in the following table (Milkereit et al., 2003):

Table 1 Early application and recent developments in mining industry

Year	
1908	First portable seismographs were used to study seismic wave propagation.
1914	The first seismic application for mineral exploration.
1980	The seismic imaging of shallow sedimentary hosted mineral deposits is first developed.
1987	First successful application of 2D seismic profiling in a mining camp.
1993	MITEC review of seismic reflection surveying for mineral exploration, led to comprehensive petro-physical, borehole geophysical and seismic studies of massive sulphides.
1994	First 3D seismic survey for mineral exploration

1997	First successful application of 3D seismic for mine planning and development
2002	High resolution 3D seismic imaging made available

In recent decades, the number of newly discovered economic ore deposits has decreased because those that are near-surface have already been found and exploited. Therefore, geophysical exploration methods that can locate economically viable deposits at depths of up to several kilometres are required. The use of seismic methods could be one possible solution (Eaton et al., 2003). The potential for significant contrasts in seismic wave velocity and density of major ore deposits within their host-rocks, suggest that seismic reflection methods can play a role in targeting deep-seated mineralized bodies. As well as a contrast in acoustic impedance (of 10% or greater), several geometrical criteria must be met in order for an ore body, or any other geological feature to be seismically visible. Mineral deposits are generally small with respect to the seismic wavelength, they usually have complex geometries, and are also often found in a steeply dipping setting. It is possible to detect and prospect for ores using reflection techniques if the deposits meet the size, thickness and presentation constraints required for reflection or diffraction (Salisbury and Snyder, 2007), and the seismic method is properly tuned to the target.

Pioneer seismic reflection investigations in major mining camps in Canada, Australia and South Africa have already demonstrated that the methodology could successfully be used for exploration at depth (Malehmir and Bellefleur, 2011). Today, there are numerous 2D and 3D reflection seismic projects around the world, directly intended for targeting mineral deposits at depth (> 1000 m), or for unraveling geological structures which host mineral deposits for mining and exploration purposes.

1.1.1. Seismic Exploration for Minerals – Special Considerations

Processing and interpretation of seismic reflection data using standard oil and gas seismic techniques are based on an underlying layered earth model. For example, recorded traces are organized and stacked to image continuous features; observed variations in amplitudes are modeled assuming specular reflection from a quasi-planar boundary. In mining, continuous marker reflections such as sills sometimes exist (Juhlin, 1990) but often do not. For successful application of seismic method in mining, it is paramount to consider scattering effects (Hurich, 1996), where scattering refers to diffractions that originate from localized anomalous regions. These signals are considered to be secondary importance to continuous reflections in conventional seismic processing and interpretation, but in the context of mining exploration they likely represent the most important component of the recorded seismogram. The preservation, enhancement and interpretation of scattered signal are the keys to successful application of seismic methods for mineral exploration.

1.2. Thesis Objective

Several approaches can be used in conjunction with the seismic reflection technique to detect and locate ore deposits. The main focus of this thesis is to evaluate the effectiveness of seismic beam-forming as a cost effective alternative to conventional 3-D surveys.

Beam-forming is an array processing technique for estimating characteristics of seismic waves. The basic principle of beam-forming is to combine the data collected from all sensors, and then apply the beam-forming algorithm to estimate the parameter of interest (Tu, 2009). In this study, the location of the unknown target is the parameter of interest. Beam-forming could be an approach to decreasing the cost of the seismic technique by significantly decreasing the source cost by relaxing the imaging requirement of complete azimuthal illumination of the target, and to set the goal as subsurface detection and localization, rather than complete imaging. Also, as can be seen in Chapter 2, by finding an optimum receiver array we intend to decrease the number of receivers as well and then apply beam-forming further decreasing cost.

To achieve the objective of this research, a quasi-parametric study of the various factors that control beam performance was implemented. The following steps were taken to carry out the study:

- Simulations were developed in MATLAB to evaluate the potential configurations of the seismic receiver arrays in order to minimize the number of receivers required and reduce the time and expense of operating arrays, as well as the computational cost of executing beam-forming.
- Synthetic seismic data were generated, in Seismic Unix, using the finite difference method.
- Software algorithms were developed, using MATLAB, to perform the beam-forming procedure to localize targets both horizontally and vertically.
- A quasi-parametric study of various issues that may affect beam performance is carried out.
- The result of the parametric study is analyzed and discussed.

1.3. Thesis organization

This thesis is an evaluation of effectiveness of beam-forming as a signal processing technique for exploration of deposits. The beam-forming process attempts to locate the target in subsurface.

Chapter 2 describes array theory. Different 2-D arrays (in a case the 3-D seismic recording required) have also been designed to identify optimal receiver array geometries to meet the purposes of adequate beam response and economy of deployment.

Chapter 3 introduces the theoretical background for the conventional beam-forming technique used in this study. It is known as a delay-and-sum method.

In **Chapter 4**, the method discussed in Chapter 3 is applied. The performance of the method on the synthetic and field data is evaluated. The theory is also applied to VSP data. Finally, real field data is examined to verify the beam-former under real data conditions. The obtained results show that beam-forming method can be a successful method to employ for the location of scatterers.

Finally, conclusions of the experiment and the implications of what has been achieved in this research are discussed in **Chapter 5**.

Chapter 2

Array Design

2.1. Introduction

The objective of this chapter is to evaluate the potential configurations of the seismic receiver array to identify the configurations that optimize the power ratio between the main-lobe (containing the maximum power) and its side-lobes (located outside the main beam). In preparation for field work, we need to work with 2D array, so we concentrate for finding the best 2D array in real fields. Although we did not have a chance to work with 2D array, the information is available for future research.

Another factor evaluated is the number of receivers required to achieve an acceptable beam performance. Minimization of the number of elements required decreases the time and cost involved in array deployment and computations.

2.2. Array Application

According to Johnson and Dudgeon (1984) three primary uses of sensor arrays are:

- to enhance signal to noise ratio of the sensing system
- to extract information about the signal sources (i.e. number, position, velocity, etc.)
- to track signal sources as they move

In this study we intend to use the array to increase S/N ratio and locate the target.

2.3. Array Resolution

The resolution of an array is the ability of distinguishing between two objects in close proximity. Resolution is usually quantified as the 3dB beam-width (beam width at half of the maximum power level). For a uniform linear array this is calculated in radians as (Manolakis et al., 2000):

$$\Delta\varphi_{3dB} \approx 0.89 \frac{\lambda}{L} \quad 1$$

where L is the length of the array. If we enlarge L (the aperture of the array) $\Delta\varphi$ gets smaller, and this results in a narrower beam and an increase in spatial resolution.

The resolution properties of the beam-forming method are commonly defined in terms of the Rayleigh criterion which is the generally accepted criterion for the minimum resolvable detail and establishes a standard to characterize the spatial resolution (Lundstrom, 2008). Resolution could be described in terms of wave-number. The apparent wave-number is the true wave-number multiplied by the sine of the angle of the beam away from the perpendicular to the array. The main beam response is equal to a wave-number pass-band, so the narrower beams results in higher resolution. The beam pattern of a linear array which is distributed along the X axis is shown in Figure 1.

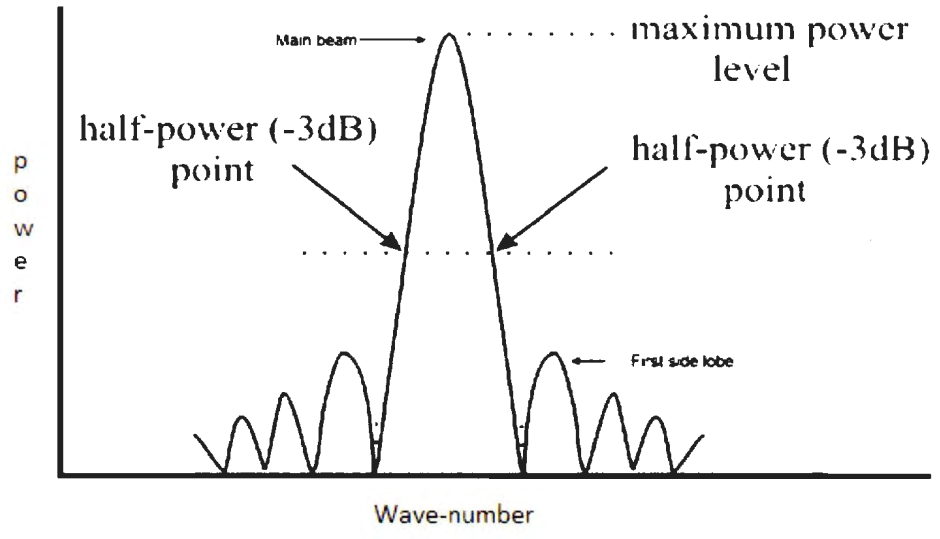


Figure 1 Example of beam-pattern of a uniform linear array. The main beam, side lobes and the width of the main beam are pointed out. Modified from (Lundstrom, 2008)

2.4. Spatial Aliasing

In modern seismology we use digital recording which means that we don't record continuously but rather we sample waves closely spaced by discrete times. To define the waves from such samples we need at least two samples per period of the highest frequency components we wish to utilize, otherwise we will encounter what is called temporal aliasing. Similarly we don't sample seismic waves with traces at all surface locations, but instead samples are separated by the group interval. Both reflections we want to extract and noise we want to suppress have apparent wavelengths that can be measured at the surface. To prevent spatial aliasing we need two samples per apparent wavelengths along the seismic line. Since wavelength is inversely proportional to frequency, higher frequency components have shorter wavelengths and are more likely to be spatially aliased (Sheriff and Geldart, 1995).

Spatial aliasing in the array results in a deterioration in the array response manifested in wrapping of high wave-number K power into lower wave-number K which affects the resolution of the beam. The initial K at which spatial alias occurs (Nyquist K) is a function of the sampling spacing of the seismic receivers.

2.5. Near-field and Far-field Region

The response of an array can be classified based on the scale of the array and the characteristics of the impinging wave-fields and is typically divided into far-field and near-field regions. The far-field is the region where the depth of the scatterer from the array is more than $L^2/4\lambda$. In this region the wavefronts are effectively planar. The near-field is the region where the depth of the scatterer from the array is less than $L^2/4\lambda$. This region is dominated by curved waves. An illustration of near-field and far-field can be seen in Figure 2. $L^2/4\lambda$ is the transition between near-field and far-field. This transition is frequency and velocity dependant. The transition graph is plotted in Figure 3 for velocity of 4500 m/s and peak frequency of 50 Hz.

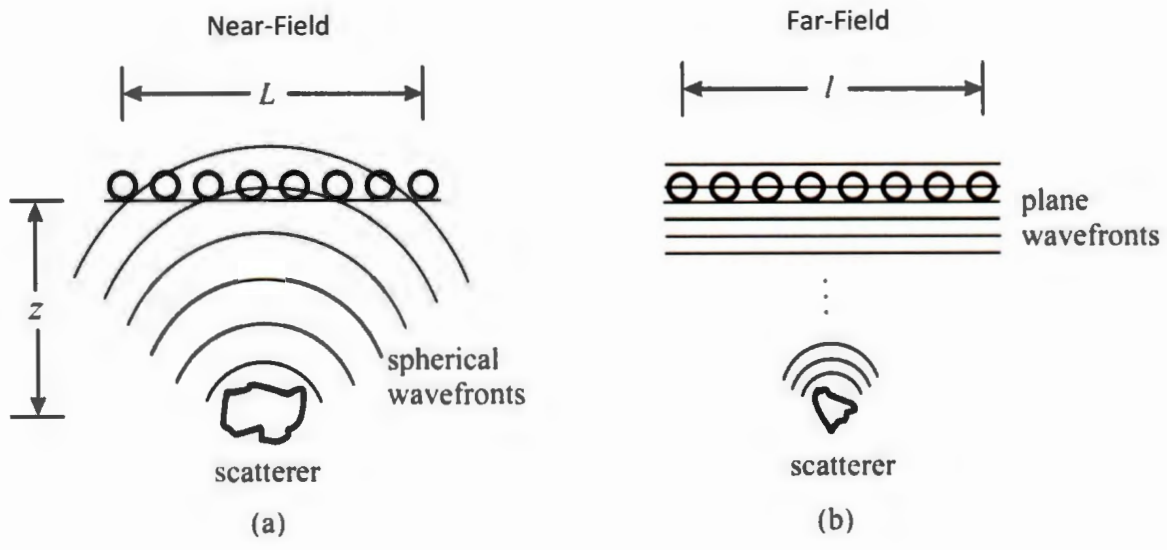


Figure 2: Illustration of the near-field and far-field scatterer (Moffat, 2002)

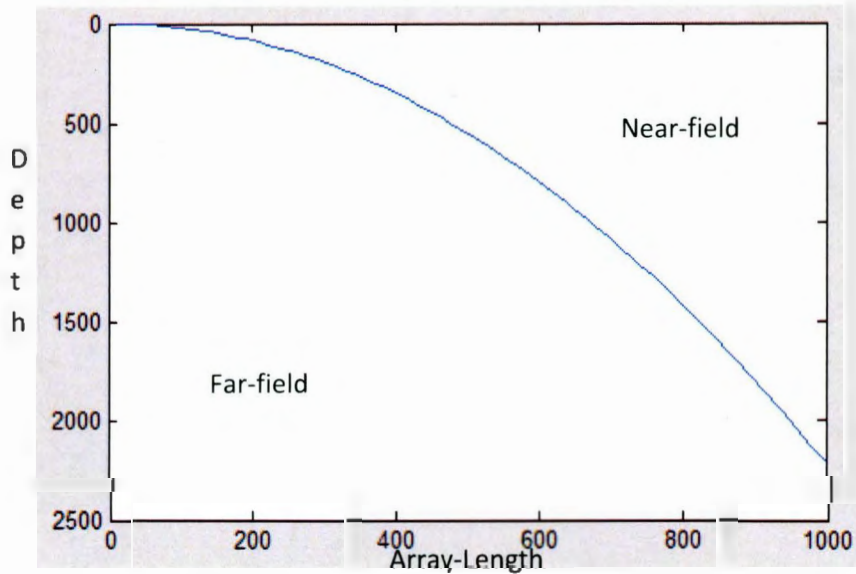


Figure 3: Schematic showing depth versus array-length bounds for near-field and far-field.

For example, for a 400 m array, 355 m depth is the transition boundary for the frequency of 50 Hz. Because the domain (near-field vs far-field) of the array response is a function of array length it is important to design the array to optimize the result.

2.5.1. Far-field Array Response

The initial aim of this work is to determine an optimal array configuration that provides results in an acceptable array response but minimizes the number of required receivers. To determine the optimal array configuration, we calculate the far-field impulse response of a variety of array configurations and compare those responses to an ideal fully populated square array.

2.6. Potential Array Configuration

Array geometries can be classified into three categories:

1. Linear
2. Planar
3. Volumetric (3-D)

Within each category, we can consider:

- a) Uniform spacing
- b) Non-uniform spacing
- c) Random spacing

For this study, we focus on linear and planar arrays. The impulse response of an array provides important information on the directional discrimination of the array as well as estimation of the width of the beam for an ideal plane wave. The impulse response of an array is determined by the power spectrum. It is also called the array transfer function because the array output is the convolution of the wave-field and the theoretical frequency-wavenumber response. The normalized array response in the k_x, k_y plane is given by (Iyer, 1968):

$$R_t(k_x k_y) = \frac{1}{n^2} \left| \sum_{i=1}^n e^{-j(k_x x_k + k_y y_k)} \right|^2 \quad 2$$

Where n is the number of receivers in the array and (x_i, y_i) are their coordinates. R always exhibits a central peak, the value which is one for this normalized case ($k_x = k_y = 0$) and side-lobes with amplitudes of less than one. The narrower the central peak, the higher the spatial

resolution of the array. The most direct method of determining the impulse response of an array is through the Fourier Transform. In the Figure 4, the array response of linear array (number of receivers =10 and spacing =10 m can be seen).

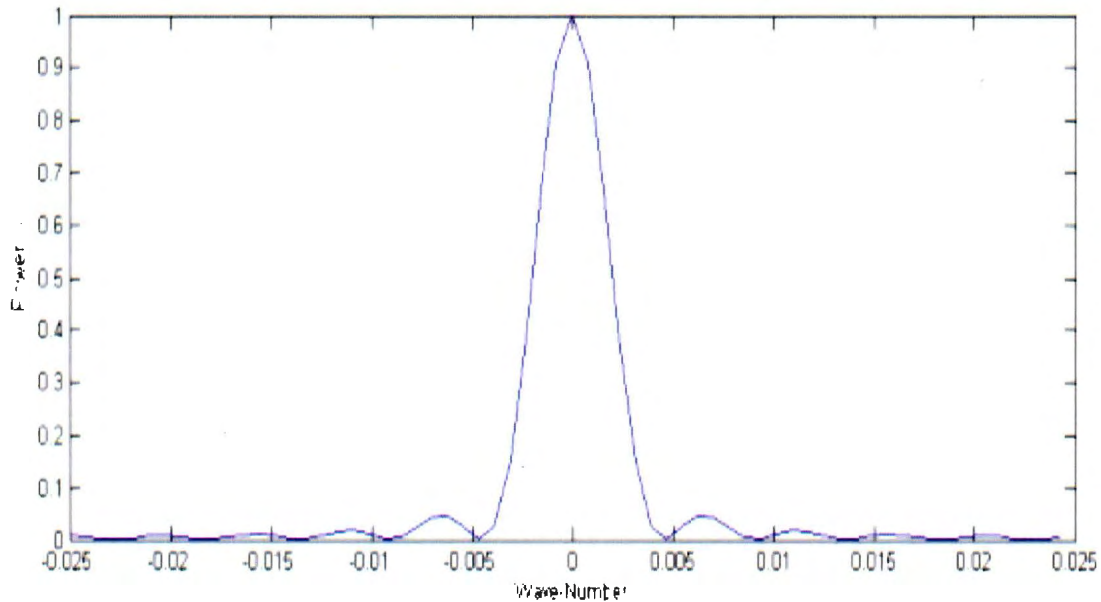


Figure 4 Array response of Linear Array. The power spectrum of the array.

In electrical engineering terminology, the main spectral line and its side-lobes are called ‘main-lobe’ and ‘side-lobes’ respectively. Optimization of the power ratio between the main-lobe of the beam and the side-lobes and minimizing beam width are the criteria used to evaluate potential configurations of the seismic receiver arrays. In addition, minimizing the number of receivers reduces the time and expense of array placement and the computational cost of executing beam-forming.

2.7. Description of MATLAB Code

Using the above theoretical background, a MATLAB code was written to carry out the discrete 1-D Fast Fourier Transform for linear array and 2-D Fast Fourier Transform (FFT) for planar array. The program codes Array1D.m and Array2D.m can be seen in Appendix A. Most of the

command lines have a comment at the end giving more details about the command. After defining the receiver space and array pattern in the matrix, the FFT is applied to the matrix and is used to determine the normalized power spectrum. Finally, the power spectrum is plotted to visualize the impulse response.

2.8. Simulation

The design of arrays to achieve certain performance criteria involves trade-offs among the parameters of the array geometry, the number of sensors, and signal-to-noise ratios (Van Trees, 2002). Here a 2-D spatial power spectrum was calculated for several different geophone arrays to find the best array which is economical and easy to implement in the real world. Square, circle, triangle, random, star, and cross patterns were used in this case because they are popular, commonly used, standard and easily designed and implemented, although not necessarily optimum (Kerekes, 2001). In this sense, we can also say that optimum in array performance is that which provides minimum side-lobe to main-lobe ratio and minimum beam-width. In the following figures, the results of various arrays with a different number of receivers can be seen.

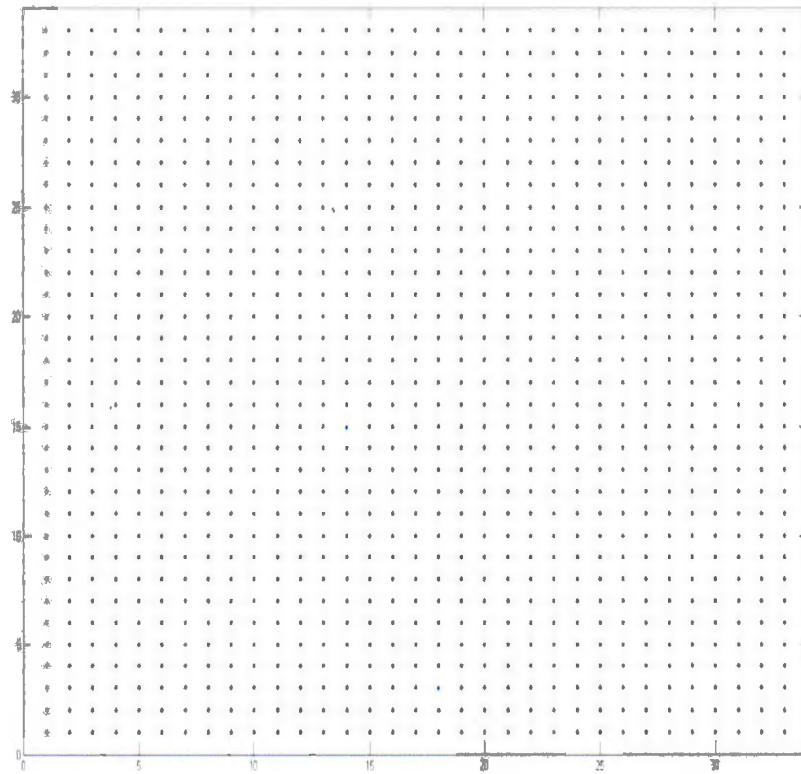


Figure 5: 2-D array (it includes 1089 receivers. There is a 5 meter interval between receivers)

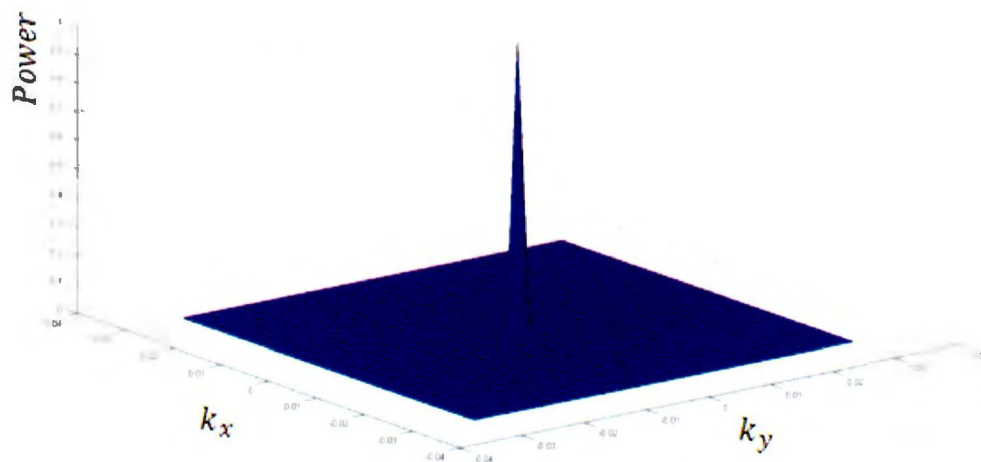


Figure 6: 2-D array response of square pattern with uniform spacing. That is used as the reference for evaluating other array configurations. The required number of geophones are 1089 for the covered area (102400 m^2).

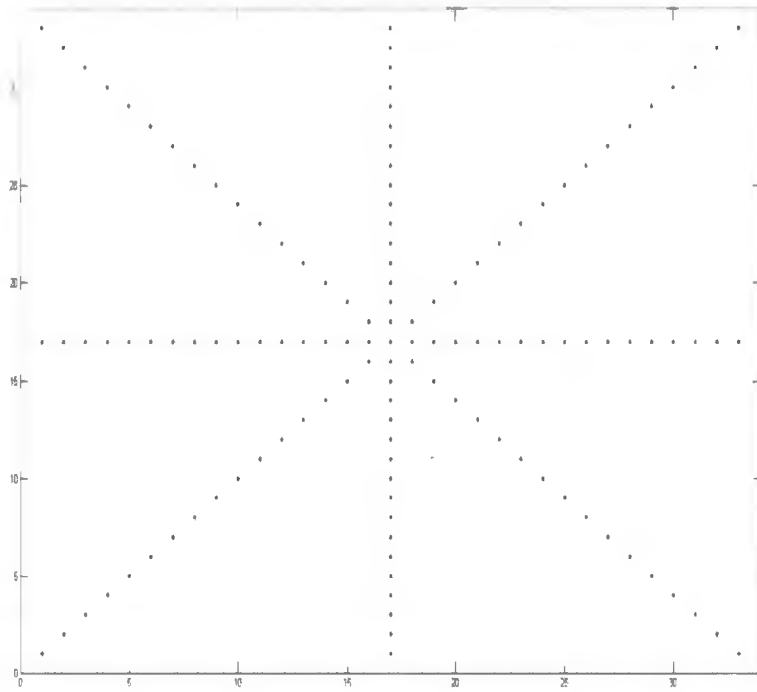


Figure 7: Star pattern geometry

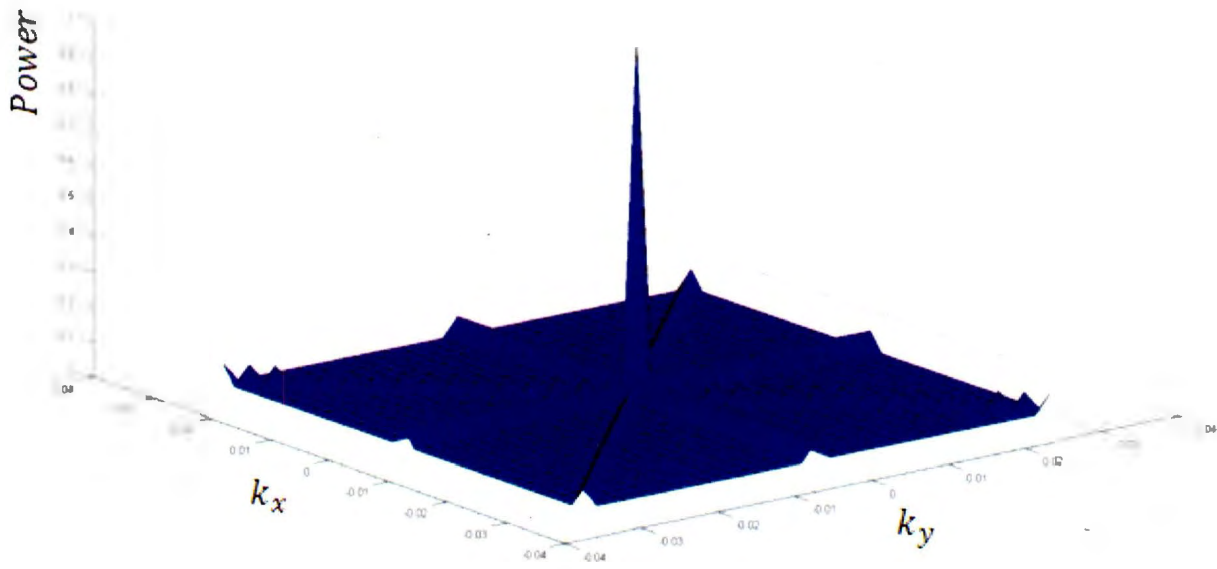


Figure 8: Array response of star pattern. Side-lobes are significant in comparison with the square array, but proportion of the main-lobe to side-lobe is acceptable. Ratio between amplitude of highest side-lobe to main-lobe is 0.01632.

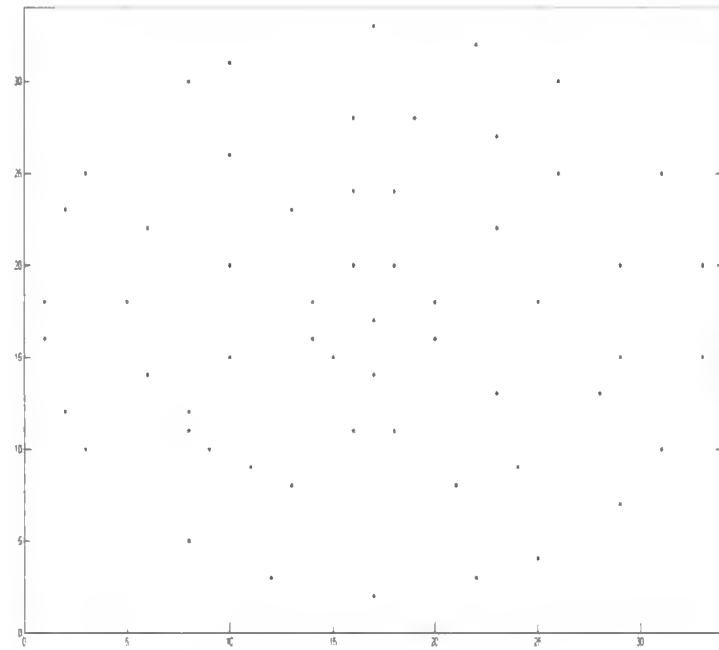


Figure 9: Circle pattern geometry

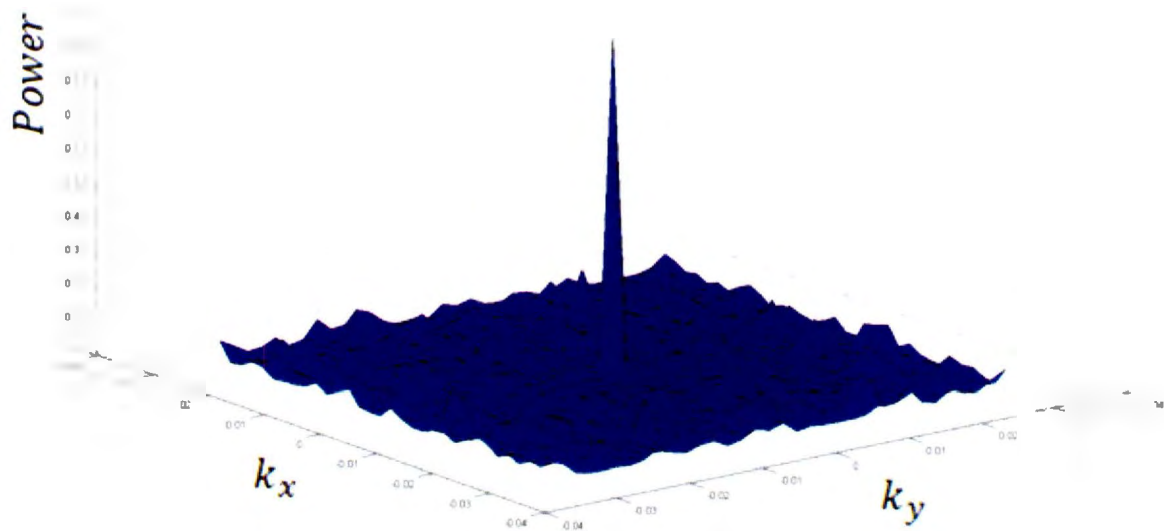


Figure 10: Array response of circle pattern (Ratio between amplitude of highest side-lobe to main-lobe is 0.1209)

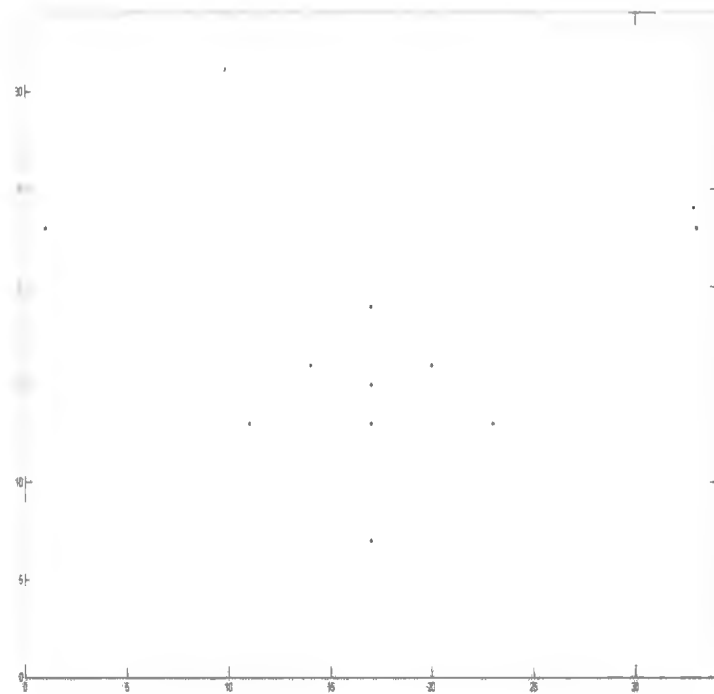


Figure 11: Triangle geometry

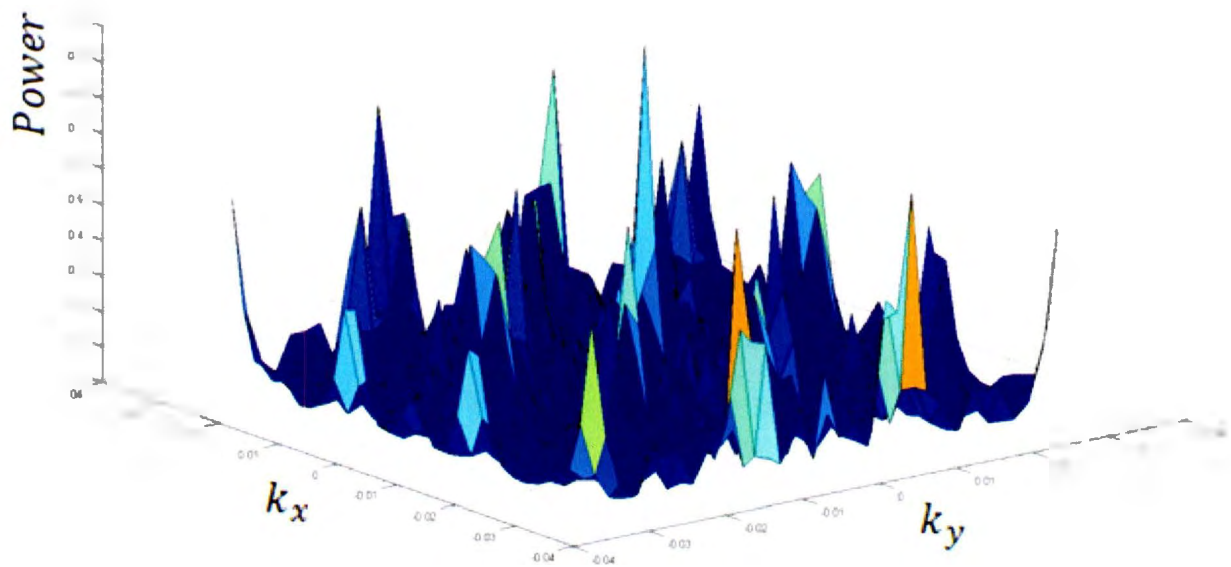


Figure 12: Triangle Pattern and its array response (Ratio between amplitude of highest side-lobe to main-lobe is 0.5883)

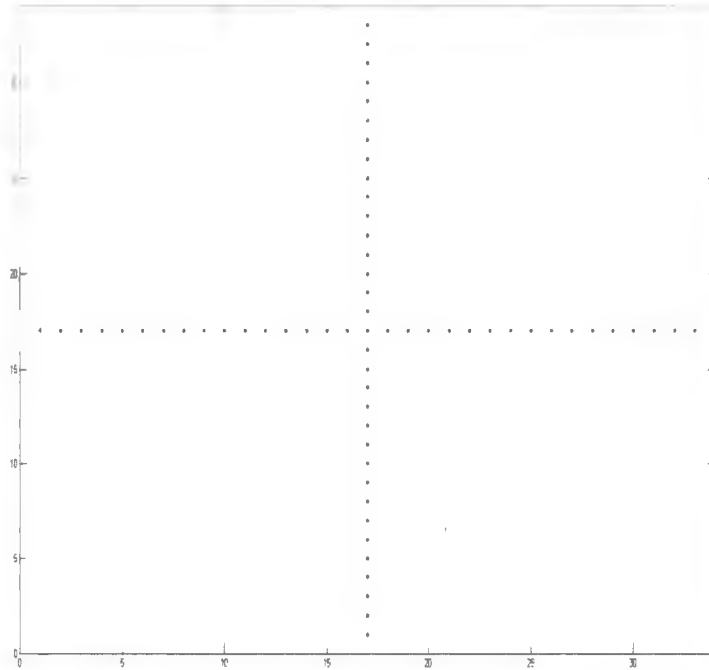


Figure 13: Cross pattern geometry

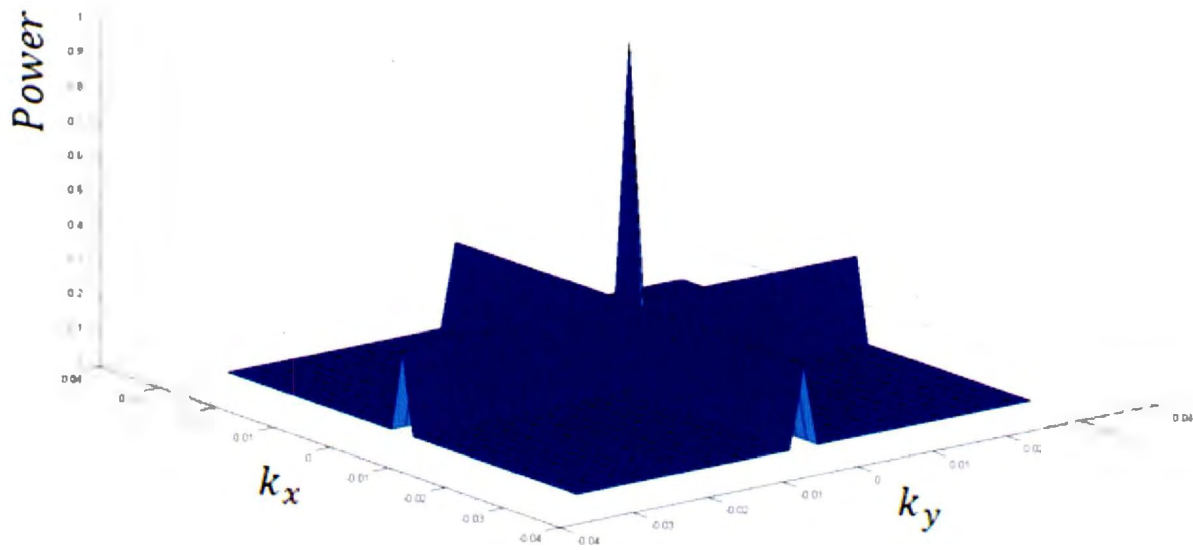


Figure 14: Cross Pattern and its array response (Ratio between amplitude of highest side-lobe to main-lobe is 0.2424)

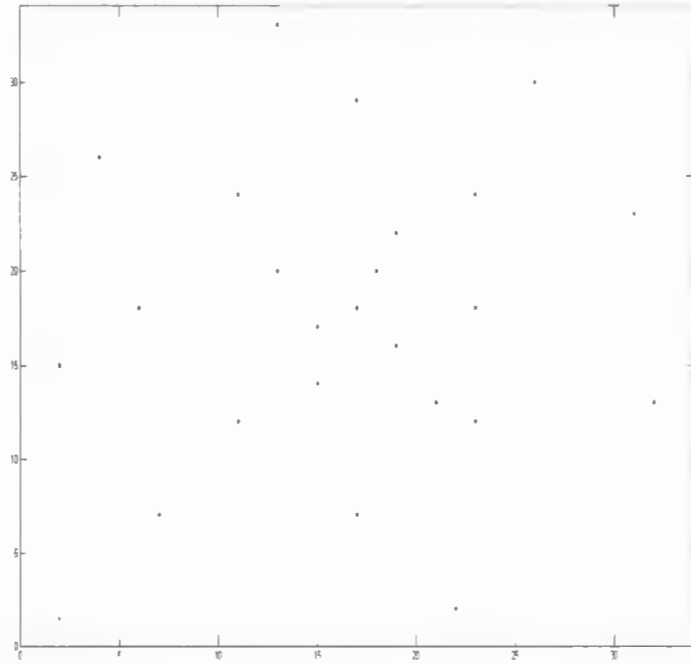


Figure 15: Random pattern geometry

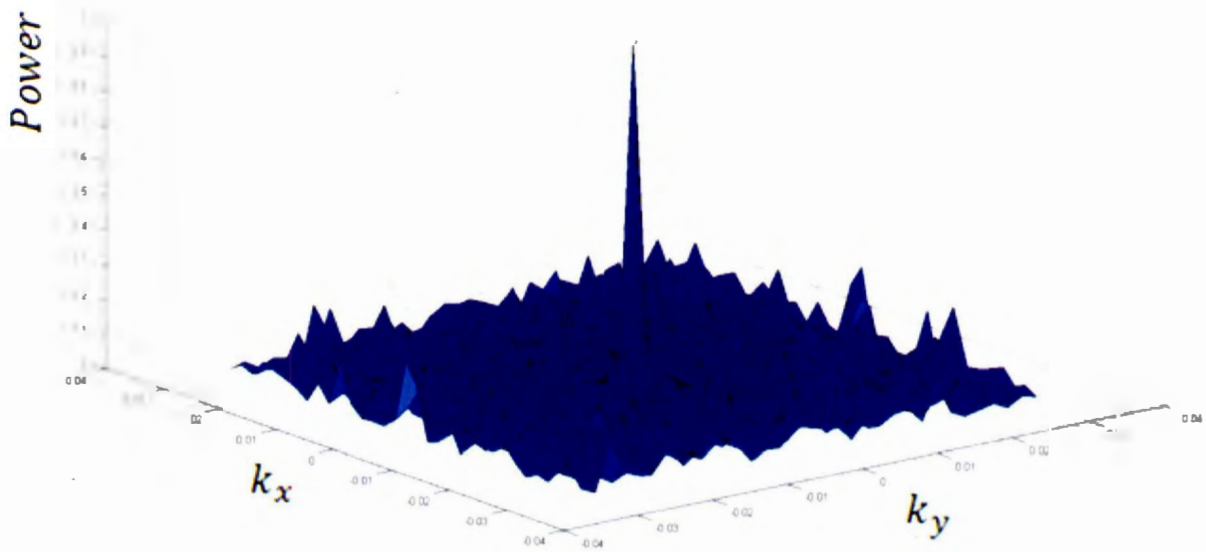


Figure 16: Random Pattern and its array response (Ratio between amplitude of highest side-lobe to main-lobe is 0.2641)

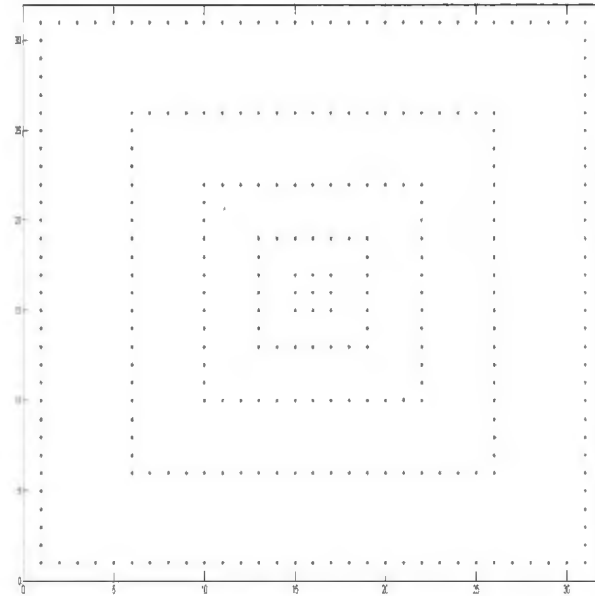


Figure 17: Square array geometry. In this array the space between square lines progressively increased. The main reason for choosing this configuration is recording the higher frequencies by the center and lower frequencies by receivers far from the centre. By this configuration, we also implement fewer of receivers in comparison with the square pattern.

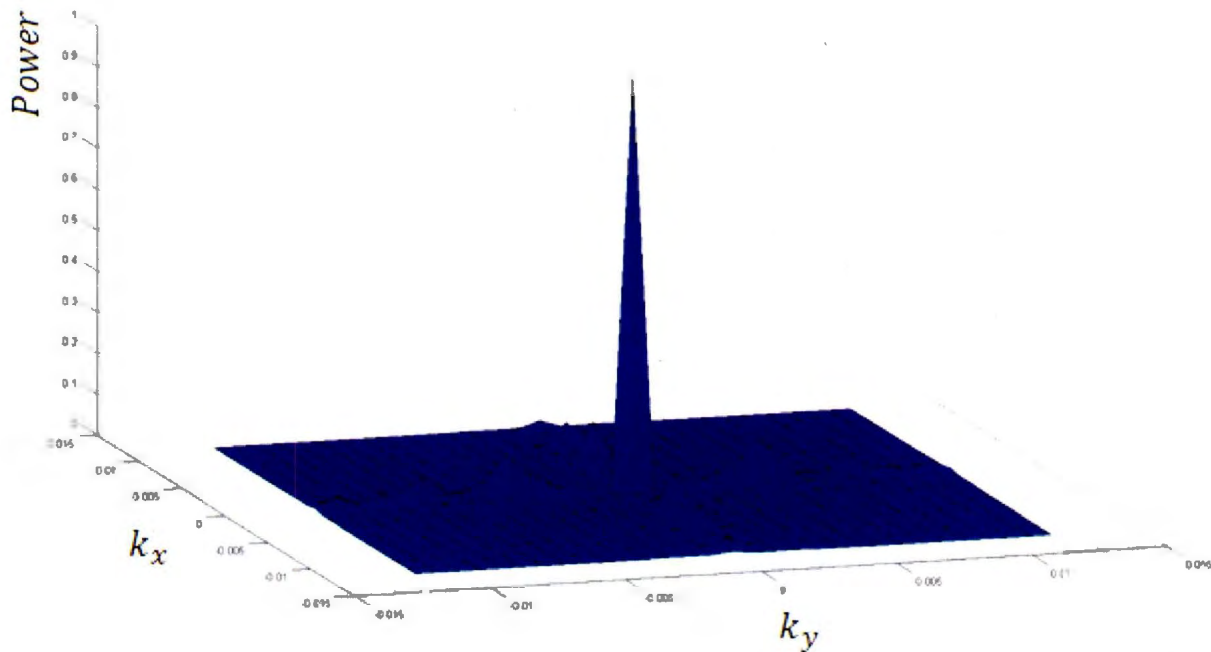


Figure 18: Progressive square Pattern array response (Ratio between amplitude of highest side-lobe to main-lobe is 0.1062)

The second aspect is the combination of the several different patterns together.

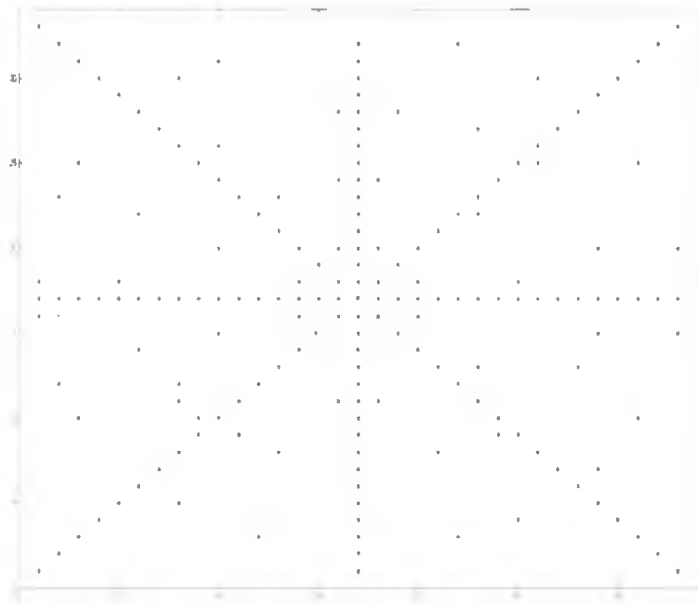


Figure 19: Combined circle and star pattern geometry

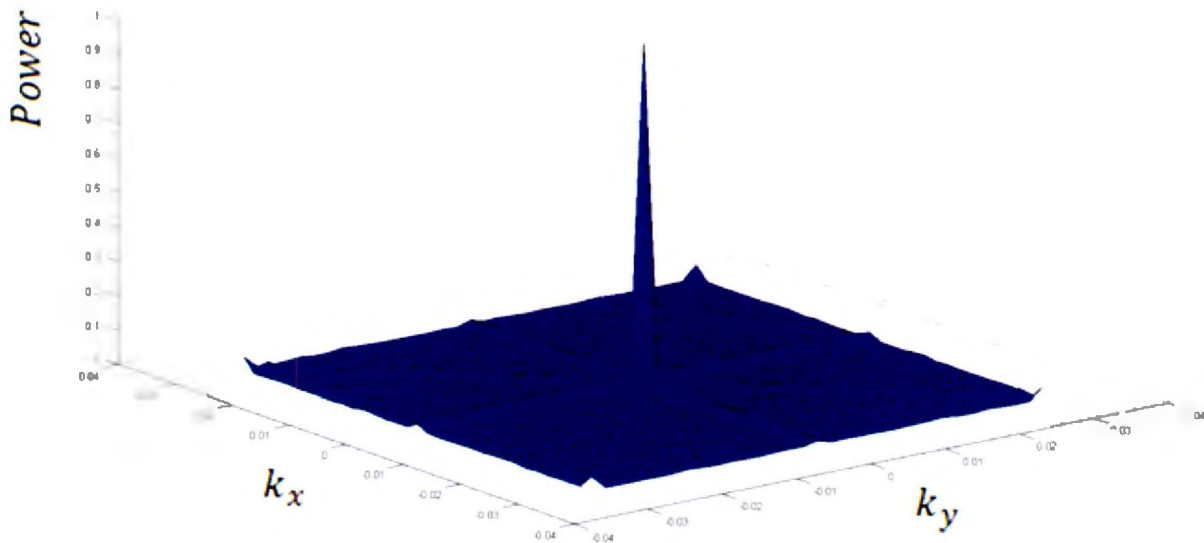


Figure 20: Combination of star and circle pattern and its array response (Ratio between amplitude of highest side-lobe to main-lobe is 0.04445)

2.9. Comparison of Different Arrays Based on Number of Receivers

Here, we compare the number of receivers which have been involved in the suggested patterns (Table 2). Minimizing the number of receivers will decrease the cost and the time for deploying arrays which is one of our goals (especially in mineral industry).

Table 2

Array	Number of Geophones	Area (m^2)	<i>sidelobe/mainlobe</i>	Beam-Width (m)
Square	1089	102400	≈ 0	0.0015
Triangle	10	70400	0.58	0.0016
Random	24	96100	0.26	0.0016
Cross	65	102400	0.24	0.0016
Star	129	102400	0.05	0.002
Circle+Star	180	102400	0.044	0.0018
Square (Progressive)	281	90000	0.10	0.0017

2.10. Summary

According to results of simulation of impulse response, for having acceptable main beam in comparison with the side lobes we have several array designs which can compete with the standard square array design and we can save significant amounts of time and money. According to the results shown in Table 2, a combination of the circle and star array gives us lowest side-lobe to main-lobe ratio and also its beam-width is close to square array.

These simulations help us to obtain an initial view of the beam response and its dependence on number of receivers, length of array and some other factors. In addition, since there is a possibility of recording real data in future in 2-D and 3-D, it is required to study different arrays response numerically to choose the array with least number of geophones which is not only easy to deploy but also to get the best response. In the next section, the beam-forming method in 2D case is explained.

Chapter 3

Beam-Forming

3.1 Introduction

Beam-forming has been used for many years in variety of applications, such as Radar, Sonar, Communications, Astronomy, and in Geophysics. The majority of array processing literature deals with the simplified case of far-field assumption for beam-forming. This means that the received wave-front from a single point source is assumed to be planar because the curvature of the wave-front is small over the length of the array. However, in many practical situations, the source is within the near-field, i.e. the received wave-front is significantly curved over the length of the array.

As discussed in chapter one, the beam-forming technique is used in this study to detect the target, instead of imaging. The use of both beam-forming and a small number of seismic sources to generate energy (the cost of which represents 40-70% of the survey cost) could significantly reduce exploration costs for deeper targets. The proposed technique follows the idea that some mineral deposits generate a characteristic scattering response, which could be detected and thus help to locate the deposits. In the following section, we present the delay-and-sum beam-forming technique used in this study.

3.2 Conventional Beam-forming

Conventional or delay-and-sum beam-forming is quite true to its name, as the beam is formed by applying delays or advances to the data recorded at individual receivers, according to the desired array response and then the receivers are summed together to form that response (the beam). Consider an array of geophones receiving signals from a target in the far-field. If the output from the geophones are simply added together then, when an emerging plane wave is parallel to the array, these geophones outputs are in phase and will add up coherently. When

the plane wave arrives from other angles such that the wave-front is not parallel to the array, then geophones across the array receive signals with differential time delays. The geophone outputs no longer sum in phase and the array output decreases. To determine the angle of emergence of a plane wave arriving at the receiver array it is necessary to apply appropriate delays or advances to transpose the wave-front into parallelism with the array (Figure 21). The transposition is carried out by searching for the system of delays/advances that maximizes the power output of the array.

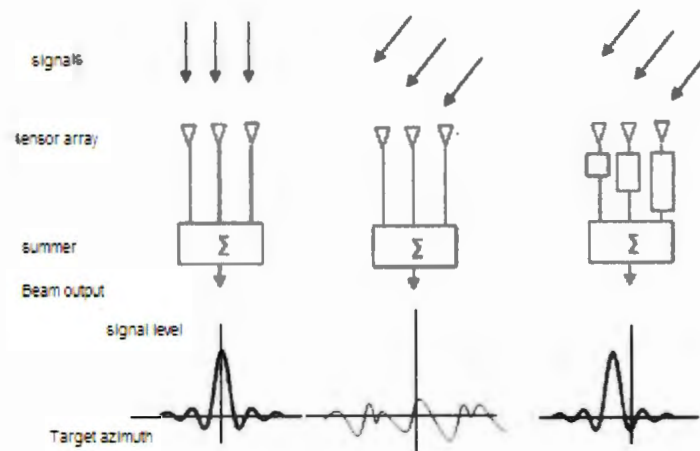


Figure 21: Basic delay schematic. When the signals arrive at the receivers orthogonally the maximum can be seen at $k_x = 0$, but when the signals coming from different angle at the same receiver we get different result. If the delays apply to receivers, the maximum will be shifted.

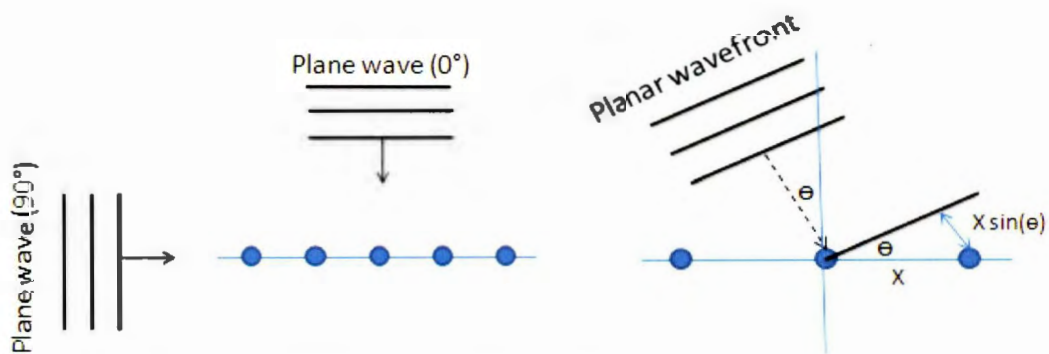


Figure 22: Linear array showing and 1-D delay calculation.

$$\text{Delay} = \frac{\text{Distance}}{\text{Velocity}} = \frac{x \sin(\theta)}{\text{Velocity}}$$

This search technique may be carried out in the time or frequency domain. This means that the search can be made by applying time delays/advances in the time-domain, or the array data can be transformed to the frequency-domain and the search carried out by applying phase delays/advances.

3.2.1 Time-domain Beam-forming

For time-domain beam-forming the recorded signals are processed in the time-domain which is the standard domain for recording seismic data. The angle of emergence or equivalently the direction from which the wave arrives at the array is found by a systematic search for a beam angle that results in the maximum power output from the array. The mathematical expression of this technique is:

$$x_m(t) = s(t - \tau_m) + n_m(t), \quad 3$$

Where $s(t - \tau_m)$ = delayed signal, $n_m(t)$ = Background noise, m = receiver number, and τ_m is the time delay.

If the output is weighted, delayed and then summed to make the beam output, it can be presented by:

$$y(t) = \sum_{m=0}^{M-1} w_m x_m(t - \tau_m) \quad 4$$

Weighting the individual elements of the array allows modification of the beam response to attenuate side lobes introduced by the finite length of the array. The general operation of time-domain beam-former is shown schematically in Figure 23.

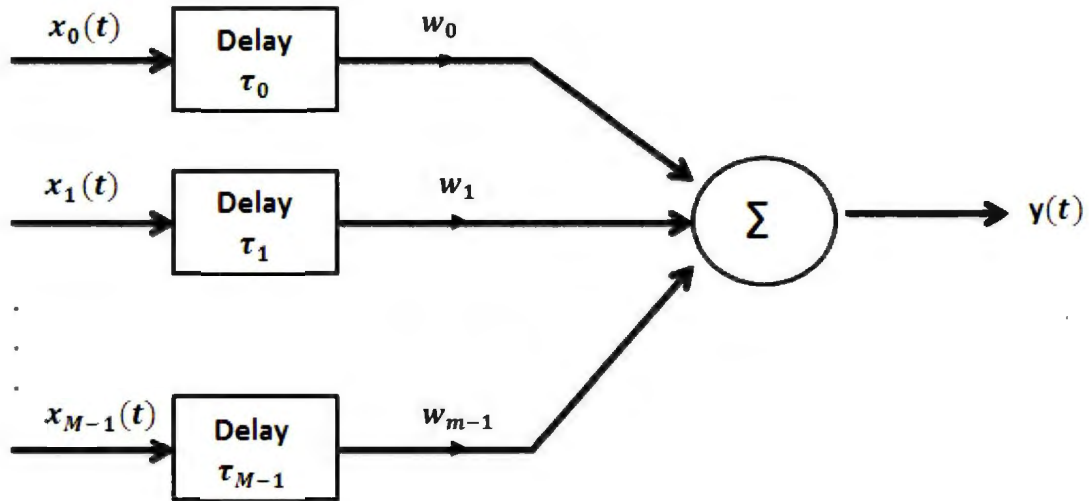


Figure 23: A general form of a time domain beam-former x_m, τ_m are input and time delay respectively and w_m is the amplitude weight of the m th receiver. Modified from (Dudgeon et al., 1984) and (Moffat, 2002)

The objective of this beam-former is to determine the angle of arrival of waves that reach the array, so as to determine the direction of the source from the array.

3.2.2 Frequency-Domain Beam-forming

Frequency domain beam-forming creates a beam by performing the delaying and summing operations in the frequency domain (Dudgeon and Mersereau, 1984). Because a time shift is equivalent to a phase shift in the frequency-domain, beam-forming can be carried out by phase shifts and summation in the frequency-domain. The transformation from the time-domain to the frequency-domain is carried out through the Fourier transform which is an operation that decomposes a signal into its constituent frequencies. Therefore, the first step of frequency-domain beam-forming is Fast Fourier Transform (FFT) of the input signal, and the last step is the

inverse FFT to obtain the transformed signal in the time domain again. The Fourier transform of the beam is given by (Dudgeon and Mersereau, 1984):

$$Y(f, \varphi) = \sum_{m=0}^{M-1} w_m X_m(f) e^{j2\pi f_D \tau_m(\varphi)} \quad 5$$

Where $X_m(f)$ is the frequency domain input signal, f_D is dominant frequency of signal, $\tau_m(\varphi)$ is the time delay of the m th receiver and f, φ and w are frequency, angle and weighting factors.

The general operation of the digital frequency domain beam-former is shown schematically in Figure 24. The reason for using the frequency-domain implementation is generally because it is computationally faster; therefore, allowing rapid analysis of large volumes of data.

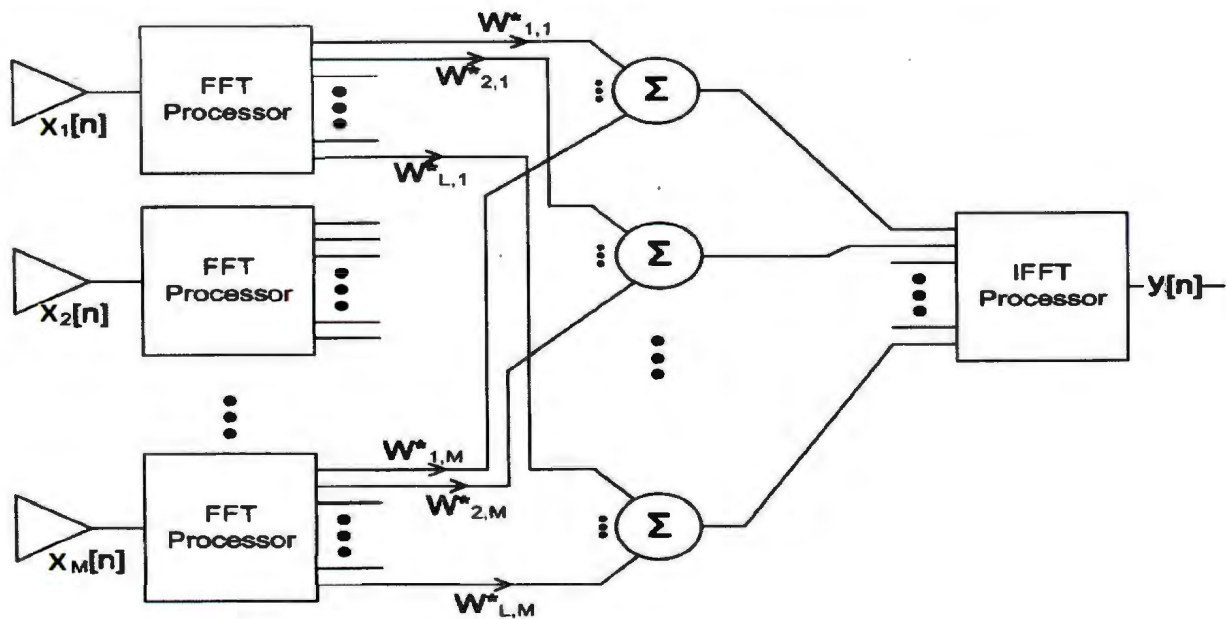


Figure 24: A general form of a frequency domain beam-former. The first step in this design is that each input data stream is transformed from the time domain to the frequency domain via the fast Fourier transform (FFT). The last step to get the beam-former output is to apply the inverse transform to the processed FFT vector to obtain time samples once again. The beam-former weights in this case are complex (Allred, 2006).

In this section, classical beam-forming was explained in the far-field (Lanslots et al., 2010). In this thesis, the target of interest is in the near-field; therefore, the classical beam-forming

method cannot be directly applied. Instead, we employ a novel beam-former that uses the delay-and-sum approach, but does not assume plane waves. This novel beam-forming method is explained in the following section.

3.3 Near-field Beamformer

As was explained in previous sections, classical beamforming requires iterative determinations of the appropriate set of delays/advances to cause inphase summation of the array elements. In the far-field where the emerging wavefront is effectively planar, a linear shift is applied to each array element. In order to apply this technique on near-field targets in which the emerging wave is nonplanar, we propose an alternative near-field beam-forming method which performs the array summation using non-linear shifts. This method will be explained in detail in following sections, but before discussing the details of the beamformer it is necessary to discuss the kinematic nature of diffraction because diffraction is the foundation of the non-linear shifts applied in our beam-forming method.

3.3.1 Diffraction

The scattering of energy by point and point like impedance contrasts gives rise to waves that can be characterized by diffraction theory. For a homogeneous medium, the kinematic response of a point scatterer is a circular wavefront that propagates to the surface. Due to the time-distance relations discussed in detail in the next section the characteristic of t-x expression of the circular wavefront recorded by a surface array is hyperbolic.

Figure 25 represents a single point diffraction and the corresponding signature on the time section. Figure 26 also shows synthetic seismic data that were generated using a second order finite-difference modeling algorithm implemented in Seismic Unix. It shows the diffraction traveltime curve for a coincident source and scatterer. The scatterer was modeled as square-shaped geological blocks placed at a depth of 300 m. A source was placed directly above the scatterer. The dominant source frequency for all generated data is 50 Hz. Since we have used Seismic Unix (sufdmod2) for producing synthetic data, the wavelet is not pure zero-phase.

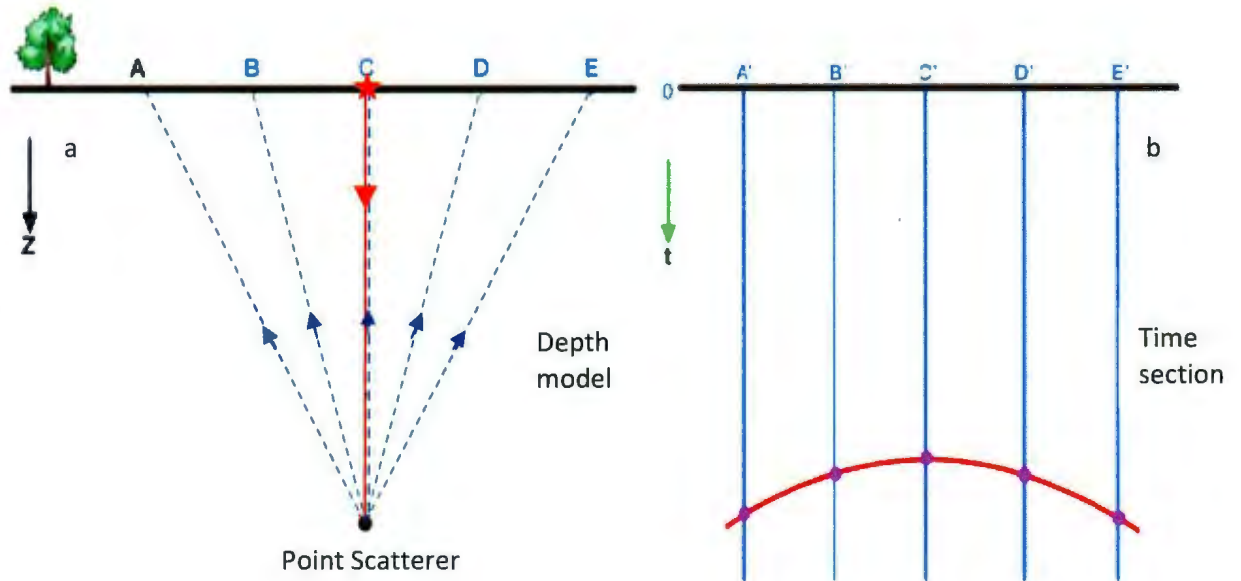


Figure 25: (a) Represents a single-point in-homogeneity in the earth, returning seismic energy from a source at the surface to an adjacent geophone, and (b) represents the corresponding signature on the time section.

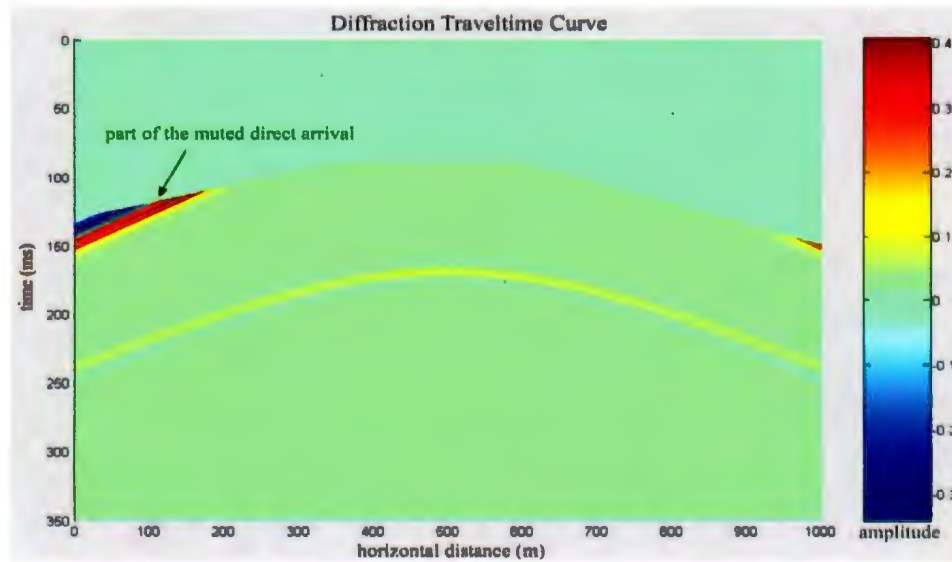


Figure 26: Diffraction travel time curve for a source above scatterer. Since the direct wave, which arrives first at the receiver array, had higher amplitude than the diffraction, it was muted out to enhance visualization of the low energy diffraction.

3.3.1.1 Diffraction Equation

A theoretical diffraction curve is governed by the geometry of the array and the background velocity. In the case of a linear geophone array (for the scatterer below the geophone array), the source could be coincident with the scatterer or offset from the scatterer. Figure 27 shows the geometry of a source (a) above the scatterer, and (b) offset from the scatterer.

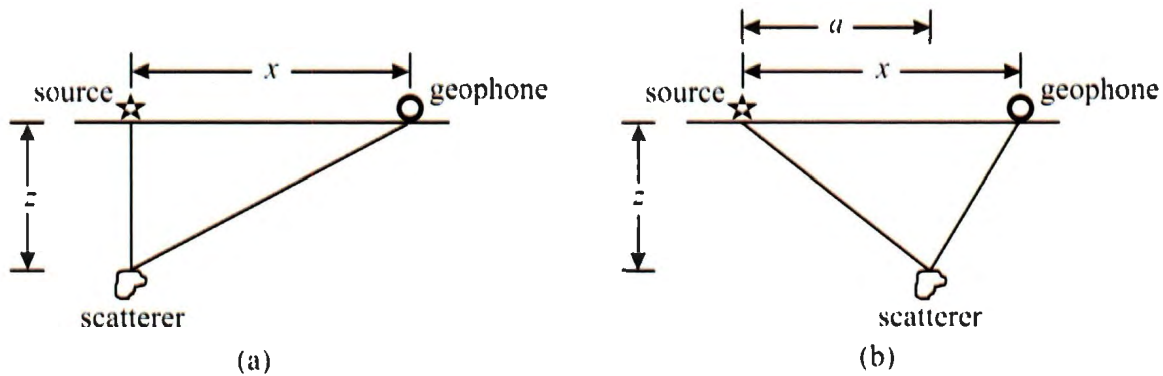


Figure 27. Geometry of a source (a) above the scatterer and (b) offset from the scatterer.

The diffraction travelttime curve for a common source gather over the diffracting point for $z \gg x$ is given by (Sheriff and Geldart, 1995):

$$t_d = (1/V)[z + (x^2 + z^2)^{1/2}]$$

$$\approx 2z/V + x^2/2Vz = t_0 + 2\Delta t_n \quad 6$$

Where t_d is diffraction travelttime, v is the velocity and $\Delta t_n = x^2/4Vz$ is the normal moveout for a reflection. However, when the source is not vertically over the diffracting point, the diffraction travelttime curve is given by (Sheriff and Geldart, 1995):

$$t_d = (1/V) \left((z^2 + a^2)^{1/2} + [(x - a)^2 + z^2]^{1/2} \right)$$

$$\begin{aligned}
&\approx 2z/V + a^2/2Vz + (x - a)^2/2Vz \\
&\approx t_0 + (2a^2 - 2ax + x^2)/2Vz \\
&\approx t_0 + 2\Delta t_n + \frac{a(a - x)}{Vz}
\end{aligned}
\tag{7}$$

The beamformer developed in this work uses the equation valid for source above scatterer. The difference between last two equations is the factor of $\frac{a(a-x)}{Vz}$ which is zero for the geophones on top of the target because a equals x . $\frac{a(a-x)}{Vz}$ has the maximum value for the shallow targets and targets that are in far-offset in respect to the source. Since our goal is detection and in most cases we don't have prior information for target for simplifying we ignore $\frac{a(a-x)}{Vz}$ value in our method. We will show that this assumption does not affect our detection by showing two models 1) source above target and 2) source offset from the target in section 3.4.2.2.

3.3.2 Characteristics of Diffraction

There are several important characteristics of the point diffraction:

- The travel time curve of a point diffractor is a hyperbola with its apex fixed above the diffractor, so if we can find the apex we locate the spatial position of the diffractor.
- If the source is offset from the scatterer, the apex of the diffraction hyperbola does not move laterally. Figure 29 demonstrates that the lateral apex position of the hyperbola is independent of the source position.
- Diffractions can appear anywhere on the shot gathers, and the traveltimes are controlled by the velocity and location of the source with respect to the scatterer.

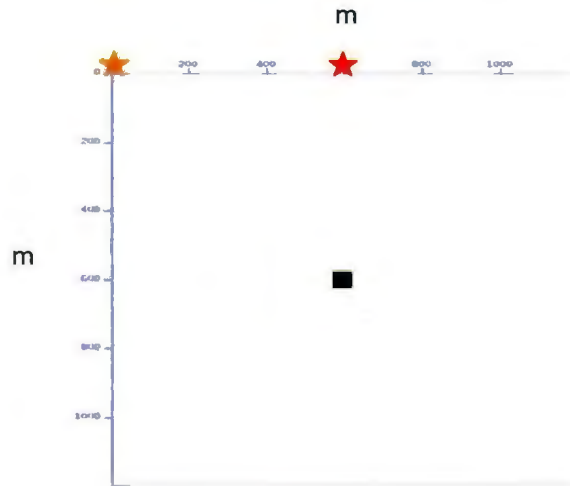


Figure 28: The basic model.

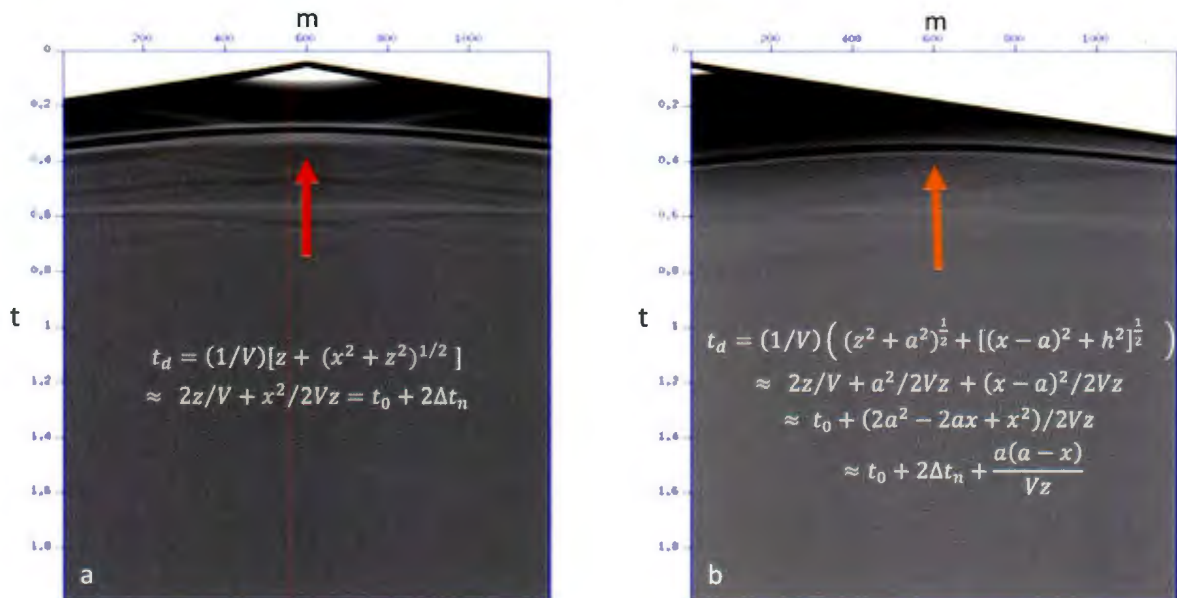


Figure 29: (a) Synthetic shot gather from the same model in the depth of 600 (m). The location of source for the left model is on the middle of the survey (600 m) and for the right one is on the beginning (0 m). The arrows show the apexes. (b) The lateral position of the apex did not change when the source position was changed, but the shape of the hyperbola and vertical position of the apex was changed. As long as we don't have any prior information about the target position in respect to the source, we could use surface data to detect the target horizontally and VSP data to detect the target vertically.

Therefore, if we can find the diffraction hyperbola, the position of the apex shows location of the scatterer. If the source is exactly on top of the target, not only do we locate the scatterer horizontally but also vertically at correct location. But that is not always the case, because the

source could be anywhere in respect to the target. The point is that we can always locate the scatterer spatially.

3.4 Description of the Method

In the near-field beam-forming method, similar to the classical method, once we apply the delays with the use of the diffraction concept, the next step is to perform the summation of the array elements. In this beamforming method, we assume that the source and the scatterer are horizontally coincident and we use equation 6 for our method. Then we form the beam (sum along the hyperbola) for each potential target location. The absolute value of summation (beam power) is then placed on the assumed target's position, which is the apex of the hyperbola. The absolute value is used to provide a better display in the beam-power plot for distinguishing top and bottom of the target because the peak and trough have different polarity. The use of the absolute value forces the beam response to always be positive. For a known velocity the process simply requires forming the beam at each potential scattering point, while for an unknown velocity you have to form the beam iteratively to determine max beam power. Details will be explained in sections 3.4.1 and 3.4.2.

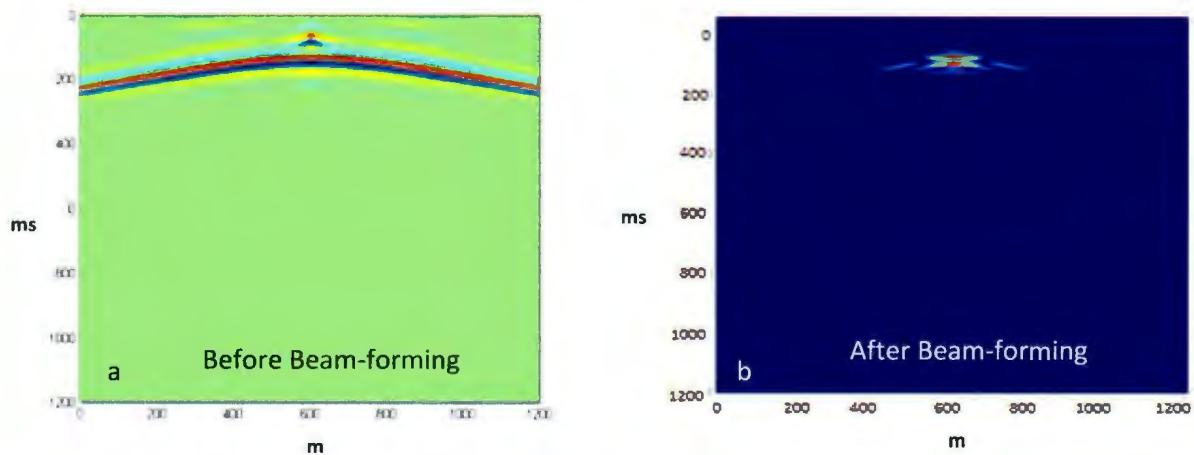
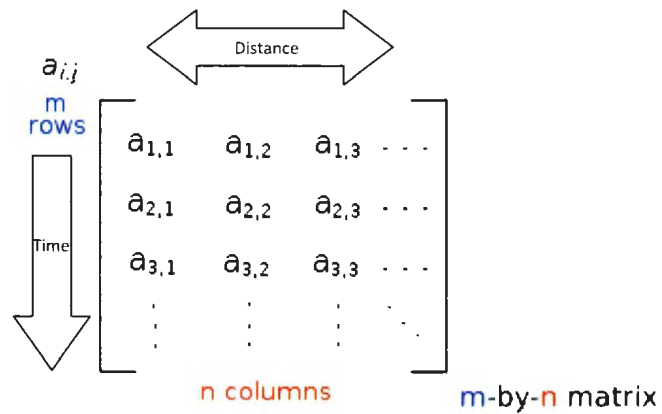


Figure 30: a) Shot gather example before applying beam-forming b) this figure shows an example of a beam-power image.

3.4.1 Explaining the Method in Detail

The approach is to beam-form at every potential diffraction apex point in the data and then assign the beam-power at these points to the position of the potential apex. Because we don't have any prior information about the location of the scatterer, so we need to search for every possible position. The following figures clarify the idea. Keep it in mind that we are using MATLAB for our coding and the input and output are both matrixes.



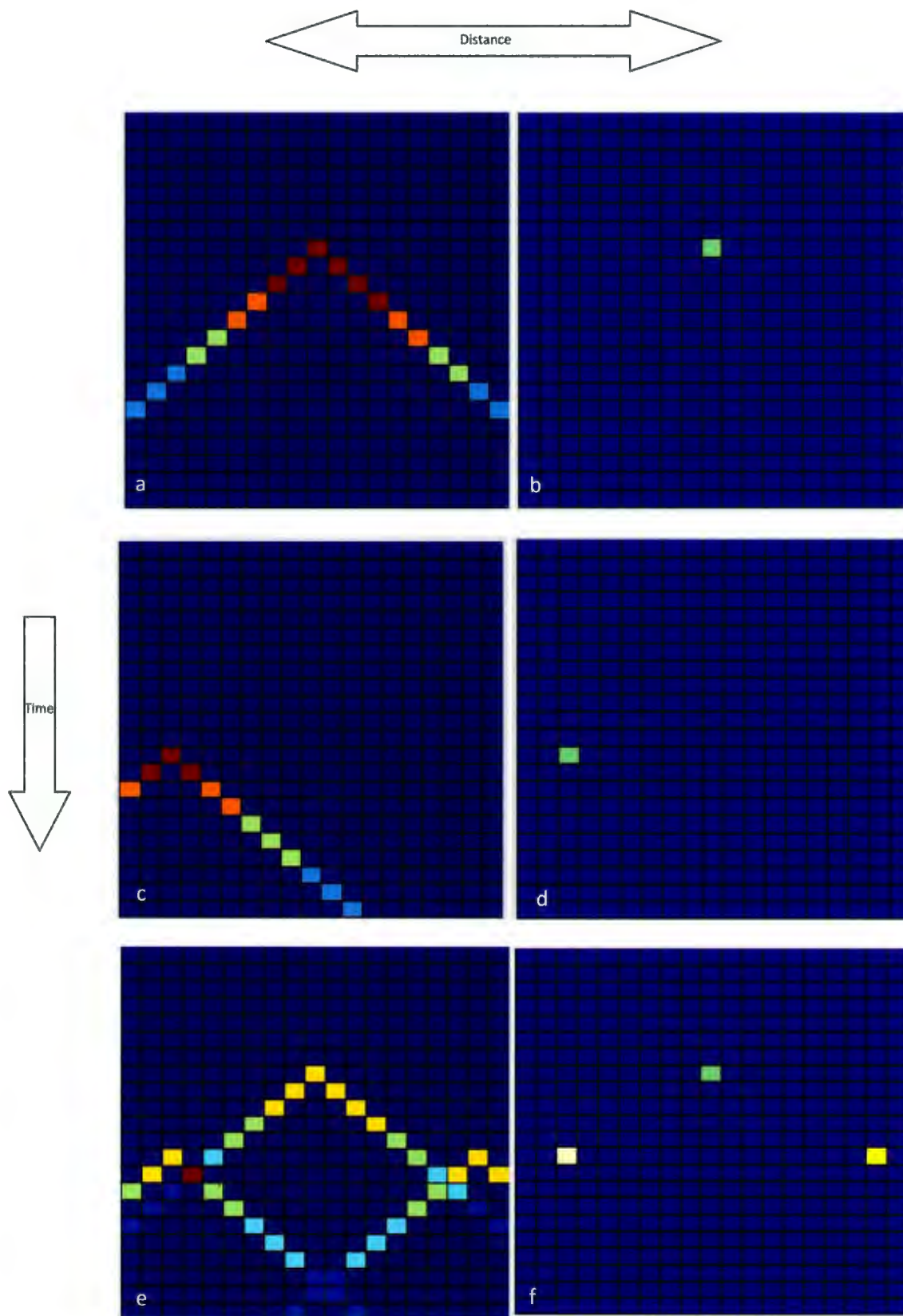


Figure 31: (a), (c) and (e) are the schematic of the shot-gather and show diffraction response. (b), (d) and (f) are the schematic of the idealized beam-forming results.

In practice, we need to identify the elements of the matrix that contain the diffraction and sum along them and locate the value on the apex position.

3.4.2 Identifying the Matrix Elements Relevant to the Diffraction

Because the main goal of the beamformer is locating an unknown target, a global scan for the target by sweeping all possible locations of the diffraction apex is required. As the seismic scattering response to a single point is already known, we can define a hypothetical hyperbolic window to cover the single point's seismic response. Therefore, for any possible target's spatial position (for each sample), the diffraction response can be calculated. By doing this, the delay is defined by the theoretical diffraction response, and summation takes place along that response. The absolute value of summation is then placed on the assumed target's position, which is the apex of the hyperbola.

As mentioned before for calculating the diffraction response, we assume that the source and the target are horizontally coincident. This built in assumption localizes the target spatially but not temporally. This is an inherent weakness of our beamforming method. Figure 32 shows an example of the hypothetical hyperbolic window that is used for identifying relevant elements in the input matrix

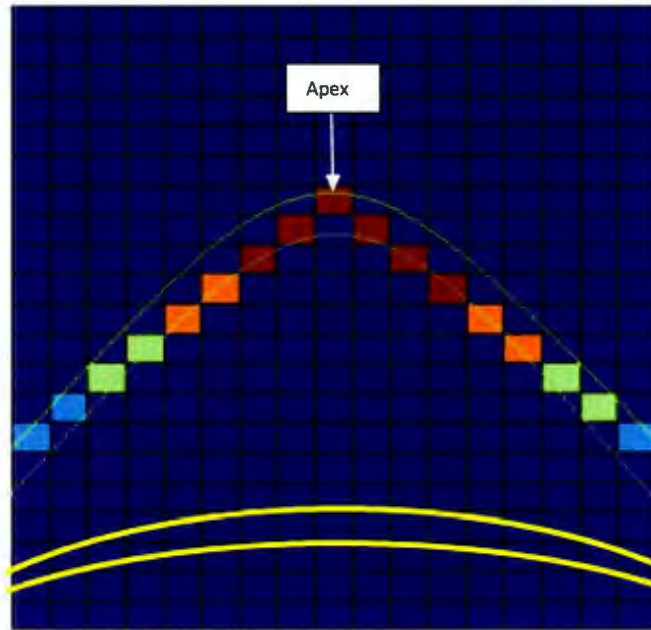


Figure 32: Defined windows for three different hypothetical apexes in various depths. The hyperbolic windows were designed to appropriately cover the scatterer's hyperbola in shot gather sections. As it is shown in the diagram, windows become flatter when the time increases.

We should mention that only one element from each row is read in. There is an option to increase the number of time samples but we will demonstrate later in this chapter that a single time sample produces the best result.

3.4.2.1 First Example

In this section, as an example, the method is applied on a shot gather from a 50 by 50 meters square target, 250 meters deep which is shown with a black square in the Figure 33 (a). In this figure the source is shown by a red star. As can be seen, the source is above the target, and it is in the middle of the array. Figure 33 (b) is the response of this target. Figure 33 (c) is the result of our near-field beam-forming method.

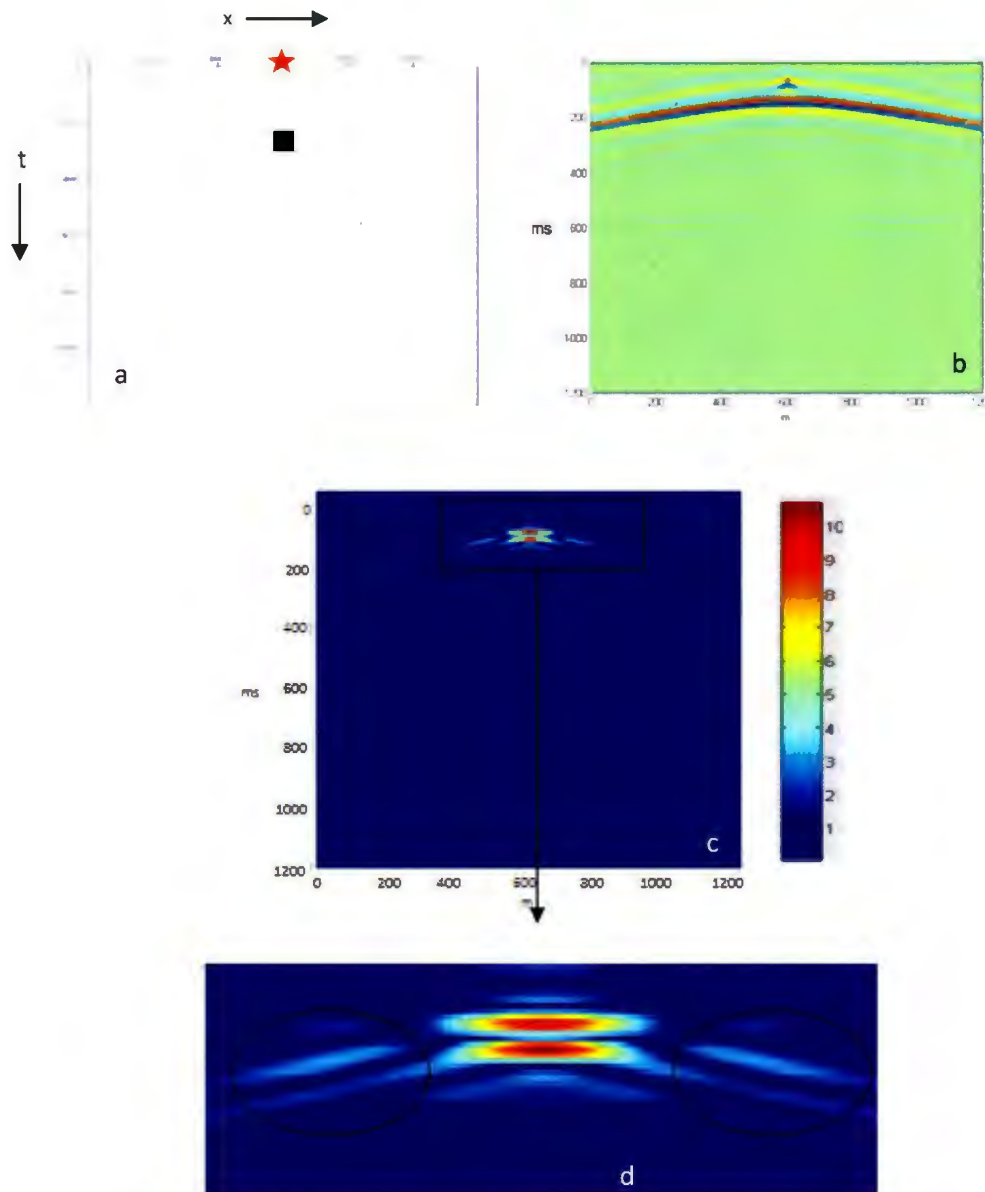


Figure 33: (a) The target is at the depth of 600 m, (b) shot gather from the model (a), (c) is the result of the described method, and (d) is the zoom of specified area of (c).

Figure 33(c) shows the final plot of our beamforming method. The blue and red colors show areas with low and high acoustic impedance respectively. In this example, two separate red events relate to top and bottom of the initial square target in Figure 33 (a). There are also artifacts on the left and right sides of the Figure 33 (d) which could be because of temporal and spatial sampling of the data, or associated with the summation process. These results

demonstrate the effectiveness of our beamforming method. To interpret the result more precisely, it is useful to look at a one dimensional display of the beam which means we are taking a time-slice of the amplitude at the time corresponding to the peak amplitude. A 1-D display of the beamformed data in the previous example is shown in

Figure 34 34.

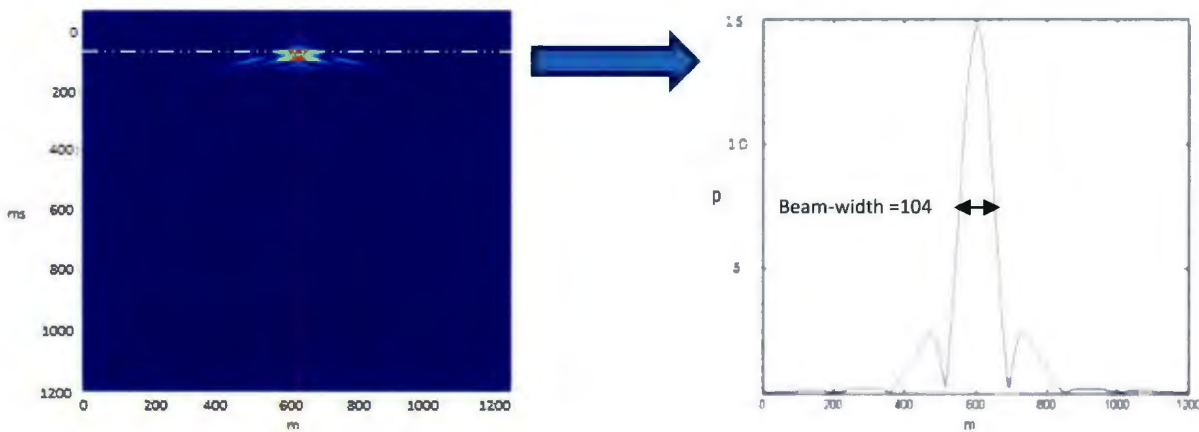


Figure 34 : One dimensional Beam

In Figure 34, the mainlobe and sidelobes are distinguishable. To characterize the beam, we determine the beam-width at a point half down from maximum power. In this case the beam-width is almost twice the real size of the target which has 50 m width. We will focus on the relation between the beam-width, target size and depth in section 3.5, but before that we need to discuss the number of samples we used in time direction for our beamforming.

3.4.2.2 Coincident source-target and offset source-target Example

To verify that the potential error associated with the assumption of coincident source and target has limited effect on target detection, we study the result of the beamformer for the following models. For the first model we have a source at the beginning of the array and for the second one the source is at the centre of the array and on top of the target which is at the depth of 600 m.

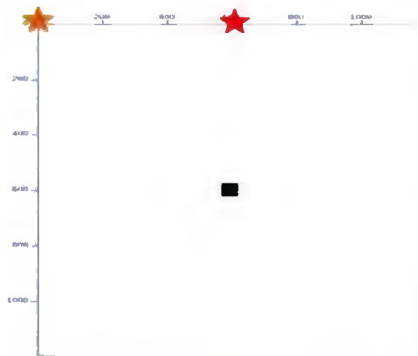


Figure 35: The basic model (the shot gather for this model can be seen in Figure 29)

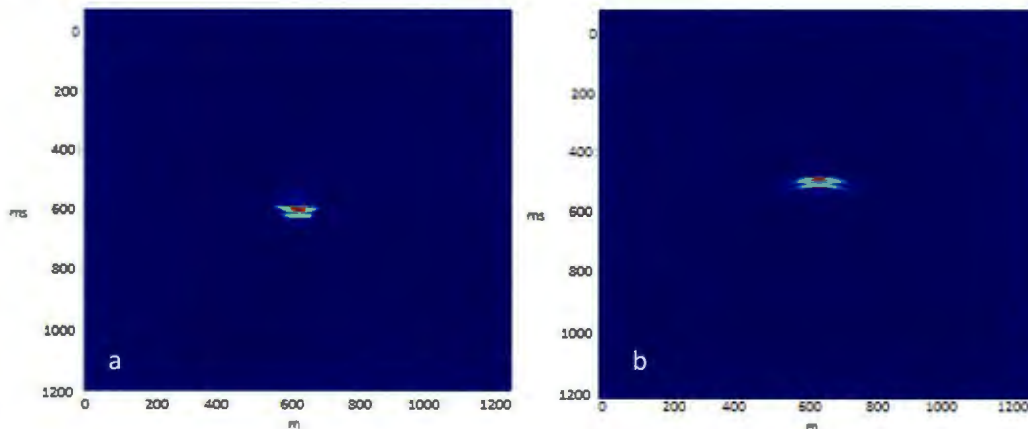


Figure 36: Result of developed beamforming method from (a) source and target are not coincident (b) coincident source and target.

Based on these results the target was correctly spatially located for both situations. However, there are couple of differences in the results:

- The artifacts in Figure 36 (a) are no longer symmetrical because the source is on the left side of the target so amplitudes are variable over the hyperbola. This shows that these artifacts are summation artifacts.
- Both targets are detected laterally in correct location, but not vertically because the travel-times from source to target and target to receivers are different for these two examples.

3.4.3 Temporal Samples

The number of time samples in the time direction used for beamforming is an important parameter. As the number of time samples increases not only the computation time increases (because it includes more samples to sum through) but also the correct detection of the known target is affected as demonstrated in following figures. In the following 4 experiments the beam-former was applied on the same model as shown in Figure 33 (the target at the depth of 250 m at the middle of the array) with different numbers of time samples. As we can see in Figure 37(a) where one sample per trace is used for the summation, the target is clearly detected but if more samples included (5 elements in Figure 37 (b), 25 elements in Figure 37 (c) and 50 elements Figure 37 (d)) both temporal and spatial resolution diminishes.

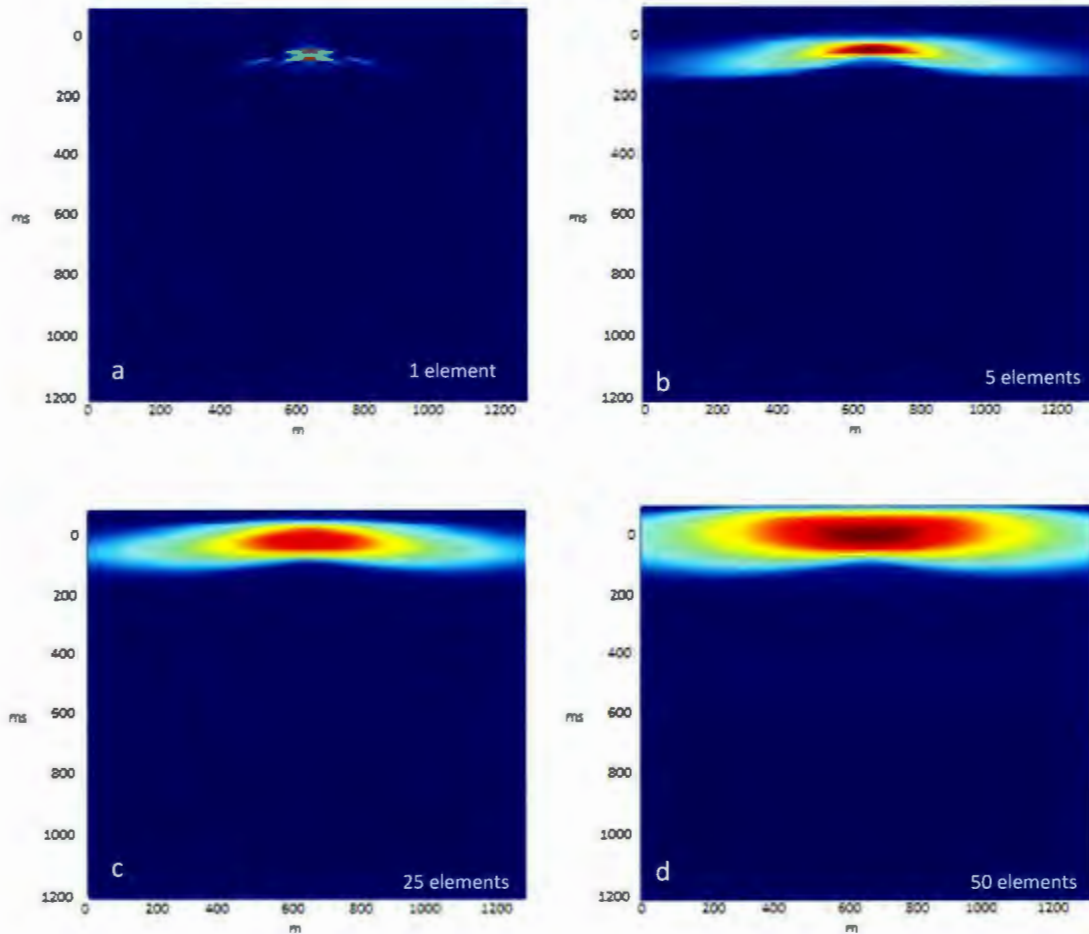


Figure 37: The results of beam-former with different elements in time direction for the target at the depth of 250 m.

This test demonstrates that including one element in time direction provides the best possible detection of the target.

3.5 Criteria for Evaluating the Beamformer

Before showing the different examples from beam-forming results, it is necessary to develop criteria for evaluating the performance of the beamformer. We also need to understand how these criteria relate to target size and target depth. The first criterion, we want to focus on is the degree of localization which means how well the beamformer actually locates the target

spatially. The second and the major criterion can be used to evaluate the beamformer is the beamwidth.

3.5.1 Degree of Localization

The degree of localization is the ability of the beamformer for detecting and locating the target spatially. This is partly related to the beamwidth but also depends on the mainlobe to sidelobe ratio. As it is shown in Figure 33 (c), there are clearly artefacts that are not just sidelobes but are caused by smearing associated with the summation process. These artifacts (in that example) are almost symmetrical and we can identify those in left, right, top and below the detected target. The power ratio of the smearing area to the highest power in the beamforming plot is small. This ratio for the shown example in Figure 33 is 0.1, so we can easily identify the target based on its high power in comparison with the associated artifacts. This is further discussed in Chapter 4 in the context the effects of noise on the beamformer.

3.5.2 Beamwidth

Since both localization and beam-width are related, we study the behavior of beam-width when the size and depth of the target is changing. By doing this, we determine the limitation for resolving, detecting and estimating the size of the target. We use this criterion in Chapter 4 to evaluate beamformer result and to compare different models.

3.5.2.1 Beam-width vs Target Size

In this section, the relationship between target size and beam-width is examined to set a standard for performance of the beam-former on band limited data. The experiment is carried out for targets at a depth of 250 m with a thickness of 50 m, and various target widths. The relation between target size and beam-width can be seen in Figure 38.

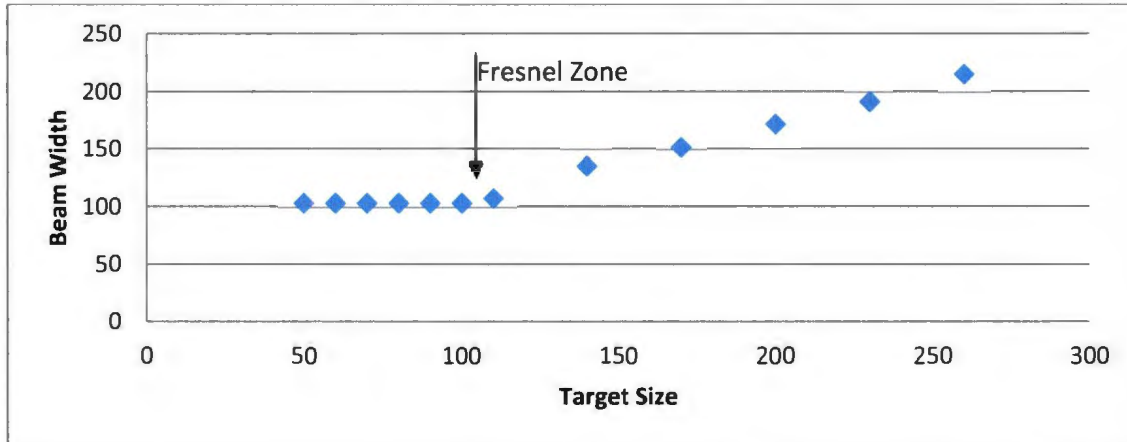


Figure 38: Beam-width vs target size graph. Fresnel radius for this specific example at the depth of 250 m is 106 m. As can be seen in the diagram the beam width doesn't change for target size less than Fresnel zone, but starts increasing when the size of the target is bigger than the Fresnel radius and it is apparently a linear relationship.

The Fresnel radius for this specific example is 106 m. As can be seen in Figure 38, the beam width doesn't change for target sizes less than Fresnel zone, but increases (apparently linearly) when the size of the target is bigger than Fresnel zone. An estimate of the relationship between target size and beam-width for the targets larger than Fresnel zone is approximately:

$$beamwidth \approx \frac{2}{3} * (target\ size)$$

For example for the target size of 400 m, we expect beam-width to be approximately 266 m. Therefore, it is still possible to detect the target smaller than the Fresnel zone by beam-forming method, but we could not estimate its size; though, for target larger than Fz we can approximately determine the size of the target.

3.5.2.2 Beam-width vs Depth

In this section we examine the relationship between beam width and the depth of the target. In order to have a fair comparison, we chose the target width equal to the Fresnel zone corresponding to the target's depth. We then determine how the beam-width changes with increasing target depth.

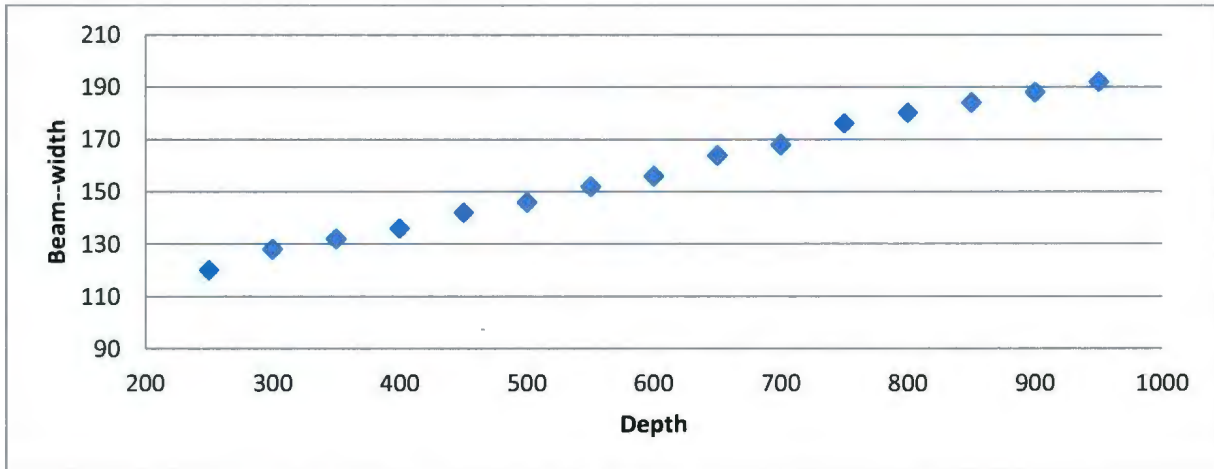


Figure 39: Beam-width vs Depth. Relationship between beam-width and depth is non-linear.

As can be seen in the Figure 39, the beam-width increases linearly with Fresnel zone as depth increases, demonstrating the link between beam-width and spatial resolution.

3.5.2.3 Fresnel zone vs Depth

In this section, the relationship between Fresnel zone and depth is evaluated. As can be seen in the Figure 40, and as it is expected from the Fresnel equation, the FZ increased with depth.

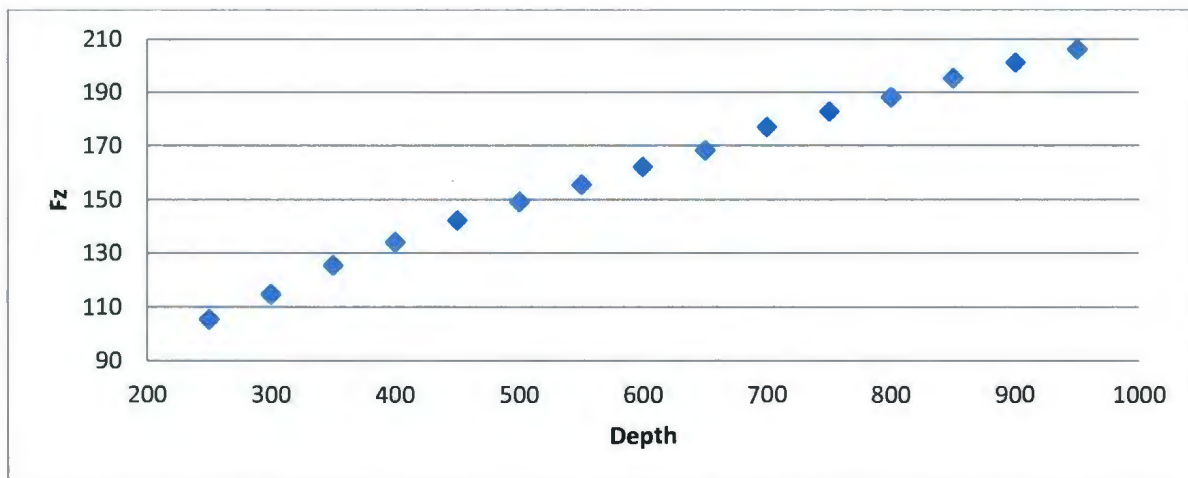


Figure 40: Fresnel zone vs Depth diagram. FZ increased non-linearly with depth.

If we compare diagrams in Figure 39 and Figure 40, approximately the same trend can be seen. We could say beam-width follows the same relationship as FZ with depth.

According to the last three experiments (3.5.2.1, 3.5.2.2 and 3.5.2.3), some conclusions can be drawn:

- The beam-former does not focus for targets smaller than the Fresnel zone (Figure 38).
- We should expect the deeper the target the wider the beam is, but beam-width varies directly with the Fresnel zone
- Beam-width systematically under-estimates target width.

These experiments verify the use of beam-width as a parameter to characterize the response of the beamformer.

3.4 Difference between Migration and this Method

After studying this method, one might question the difference between the explained method and Kirchhoff Migration. There are some differences between our technique and migration:

- In treatment of the data prior to summation: there is no amplitude and phase corrections in this method while in migration it is required to apply amplitude and phase corrections before summation.
- Our method is not as complete as the migration, and we want to relax imaging criterion and instead of fully imaging, detecting the target is the main goal. Seismic migration maps the seismic reflection energy recorded on the Earth's surface to its correct spatial and depth location, while at the same time collapsing the width of the Fresnel zone to the size of seismic wavelet in the Earth.
- The method could be applied on a single shot gather and help us to detect the target, while the migration applied on group of shot gathers (we can apply the migration on a shot-gather but it does not help us to image or locate the unknown target based on only one shot gather).

3.7 Summary

In this chapter, some aspects for delay-and-sum beam-forming and its performance in time and the frequency domain have been covered. Our introduced method has been described in section 3.4. This method has a potential to be applied on both seismic reflection profiling, and vertical seismic profiling. The relationship between the Fresnel zone, the target size and the beam-width are also examined which is a key to calibrating the beam performance. Based on the results, our preliminary objective (detecting the target) is elevated. Although, we have the ability to determine the larger target's size.

Chapter 4

Beam-former Performance

4.1. Introduction

In this chapter, the concepts discussed in the previous chapters, and the beam-former introduced in Chapter 3, are evaluated by application of the beam-former to synthetic data. These simulations are designed to examine the beam-former response in a variety of situations. The technique will be applied to both surface and vertical seismic profiles.

4.2. Synthetic Data Generation

Generation of synthetic seismic data was performed in Seismic Unix, using a second-order acoustic finite difference algorithm (Appendix D). The finite difference algorithm can be used to calculate synthetic seismograms for complex geological models that are not readily addressed through analytical solution. Finite difference modeling is a time-marching procedure, which solves the elastic equations recursively to compute motion in an elastic medium (Kelly et al., 1976). The finite difference method gives reliable arrival times of seismic events and amplitudes that vary with the elastic impedance contrasts. With respect to this analysis the most important issue with Finite Difference modeling is inaccuracy in the solution due to accumulation of the numerical errors generally known as grid dispersion. In order to minimize grid dispersion, the grid spacing parameter is defined as less than 10% of the shortest wavelength used.

The models used for the analysis have velocities of 4500 m/s for background and 6500 m/s for the target and constant densities equal to 2700 kg/m^3 resulting in a reflection coefficient equal to 0.1 between the background and scatterer. The receiver spacing is 4 m which is reasonable spacing for field experiments. The dominant source frequency for all generated data is 50 Hz. The scatterers were modeled as square-shaped geological blocks for most examples. A shot was placed in the middle of the array for most cases.

4.2.1. Processing of the Data

Prior to analysis the synthetic data were processed via Landmark's ProMAX software package and Seismic Unix. The operations employed were trace muting and band-pass filtering.

4.2.1.1 Trace Muting

Trace mutes were implemented throughout the processing sequence. A mute removes unwanted data (direct waves) from the seismogram so they don't interfere with the beam-forming. The direct wave which arrives first at the receiver array has higher amplitude than the diffractions, so the direct wave is noise with respect to beam-forming on diffractions.

4.2.1.2 Band-pass Filtering

The main reason for applying band-pass filtering in this study is because of residual effects of the mute on the data. Figure 41 demonstrates the abrupt difference between the muted part and the rest of the data, but after applying the band-pass filter this problem is solved. The type of the filter employed in this study is the Ormsby band-pass filter. The results before and after processing are demonstrated in Figure 41. Since we have used Seismic Unix (sufdmod2) for producing synthetic data, the wavelet is not pure zero-phase. Note that the wavelet was altered by the filter. While our goal is to detect the deposit horizontally on surface profiles, it doesn't have any effect on the method.

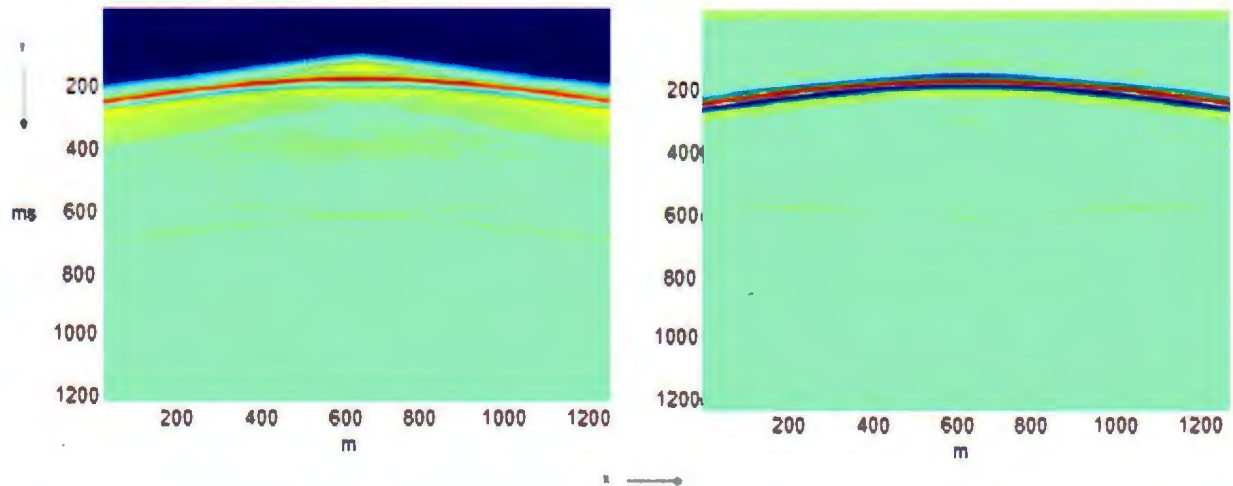


Figure 41: Left) Top mute was applied to remove first arrivals. Right) Band-pass filtered version.

You could see the band-pass filter removed the DC shift as well. The data is now ready for transfer to MATLAB which will apply the beam-forming method.

4.2.2 Description of MATLAB Code

Using the theoretical background in Chapter 3, a MATLAB code was written to carry out the objectives of this thesis. The program code *Beamformer.m* is documented in Appendix B, and it is the main code for this research. The program opens the binary data file that is exported from Seismic Unix (processing already applied to the data), and arranges the file into columns and rows representing receiver samples and time, respectively. In all the synthetic examples, the input matrix is 300 by 300. The beam-former requires velocity information to operate. For the synthetic examples, 4500 m/s was chosen, but for real field data it is required to run the code iteratively for a range of velocities and then evaluate the results (test 29). After opening and arranging the data, the program applies the delays with the use of the diffraction concept. The program then sums across the window, and puts the value on the apex position. Then, it re-plots these values as a beam power image which has 300 columns and 300 rows. There is no advance information about the location of the target. We insert the shot-gather as an input, and obtain the beam power image as an output. The beam-former as mentioned before, is searching for all possible scatterer locations.

4.2.3 Synthetic Data Generation and MATLAB Code for Vertical Seismic Profiling DATA

Synthetic data generation for the VSP examples is the same as surface profiling; the only differences are the shot location which is close to the borehole (zero-offset VSP), and the locations of receivers in the vertical direction. The MATLAB code is the same, the only difference being search direction. For surface profiling, the code searches for hyperbola from top to the bottom, but for VSP, the search is from left to right. It is handled by transposing the input matrix.

4.3 Evaluation of the Beam-formers Response for Surface Profiling

4.3.1. Studied Parameters

In this section, the beam-forming response for the uniform linear array is evaluated. The chosen velocities for all synthetic models are 4500 m/s for background and 6500 m/s for the deposits. The following is a list of possible beam-forming scenarios:

- **4.3.2:** Determine the response of the beam-former in a situation where the source and the target are in the centre of the array, and where the targets are less and more than 500 m depth.
- **4.3.3 :** Evaluate the response of the beam-former in a situation where the target is offset from the source that is at the centre of array. The main reason for this evaluation is that in the field we don't have prior information about the position of the target it could be anywhere in respect to the source.
- **4.3.4 :** Evaluate the response of the beam-former where the source is at the centre and the shapes and sizes of the targets are variable. We examined different sizes in terms of Fresnel zone (smaller and bigger than Fresnel radius) to determine detection abilities of the beam-former.
- **4.3.5 :** Determine the vertical and horizontal abilities of the beam-former to distinguish between two adjacent targets, in a case there are multiple targets.
- **4.3.6 :** Discover the results of using imperfect arrays to make our models similar to real situation where we cannot record in every single position (there could be trees and other obstructions in the line).
- **4.3.7 :** Investigate the response of the beam-former in different noise environments.
- **4.3.8 :** Study the beam-former results in data that have static shifts.
- **4.3.11:** Explore the beam-former on the combination of cases in 4.3.9 and 4.3.10.

In all of the analysis:

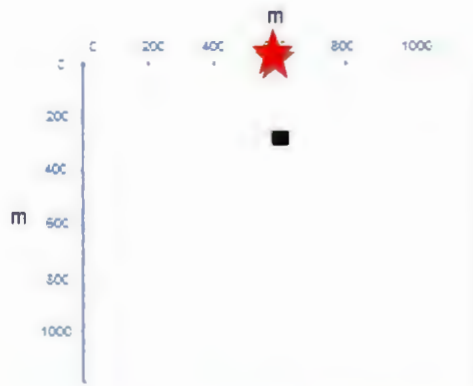
- All of the array elements are equally weighted; therefore, the highest amplitude will always contribute the most power to the beam.
- The $\frac{1}{2}$ down point of the main-beam for some models is also calculated as a measure of beam width for comparing the beam-former results.

4.3.2. Test 1: Source and target at the centre of the array

To determine the response of the beam-former in a situation where the source and the target are in the centre of the array the following models are examined:

- The square scatterer (50 by 50 m) at the depth of 250 m
- The square scatterer (50 by 50 m) at the depth of 1000 m

The size of the targets is 32% of the Fresnel zone. In order to present a better visualization of the beam-former, one-dimensional beams on the top and bottom of the detected target are revealed. According to the results, main-beams can be distinguished from side-lobes.



(a)

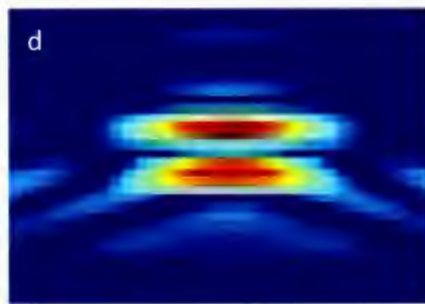
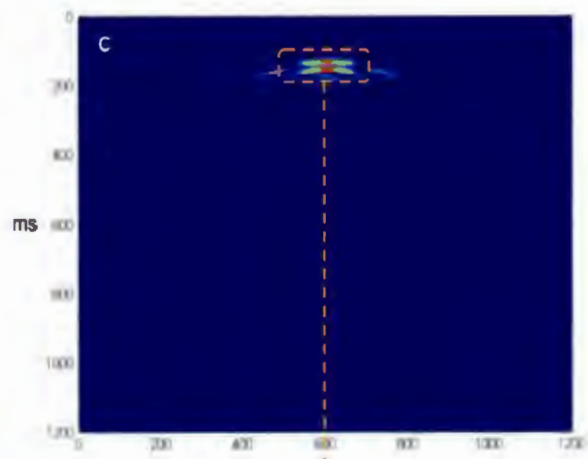
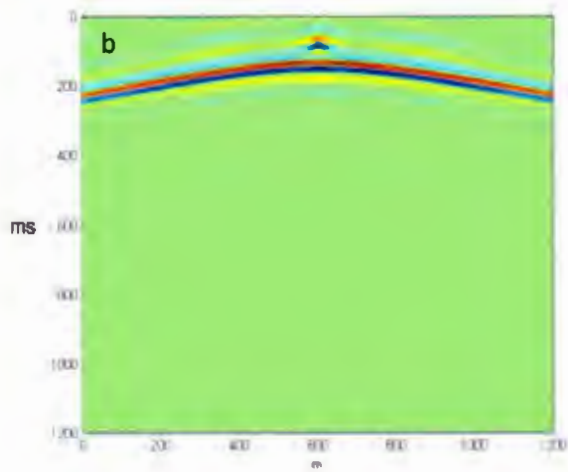


Figure 42:(a) Image showing a square scatterer. The white background represents the host rock (velocity=4.5 Km/s), the black shape represents an ore body (velocity=6.5 Km/s), and the red star is the source. This model is designed in Seismic Unix, (b) it is a shot gather, and (c) the result of the method. (d) The specified part of the part c is zoomed in to show the method could detect top and bottom of the target.

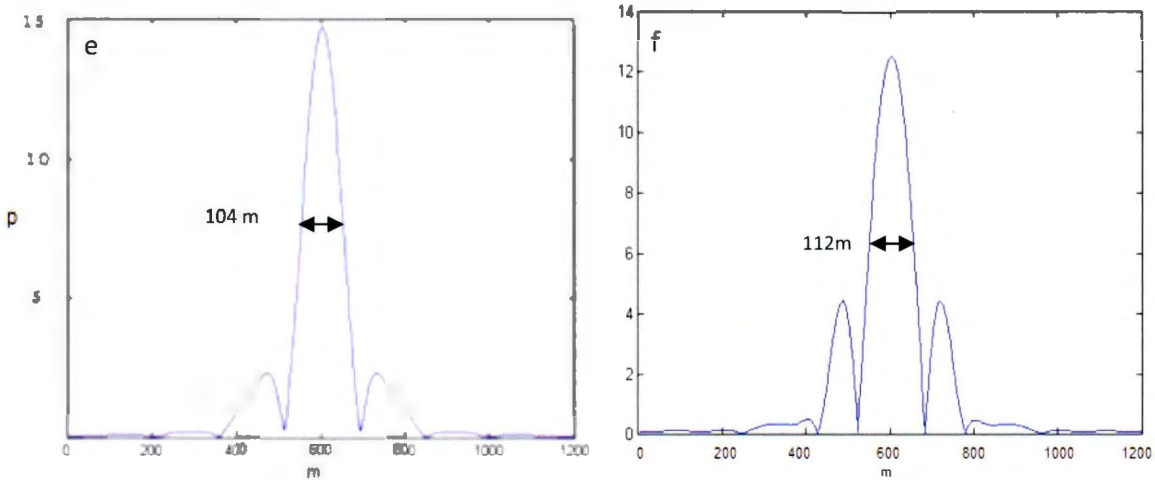


Figure 43: (e) & (f) 1-D representation of beam from top and bottom of the target respectively.

In most of the examples in this chapter, the 1-D presentations from top and bottom of the detected targets are shown to aid evaluation of the beam-width.

The $\frac{1}{2}$ down point of the main-beam for the beam from the top is 104 m and from the bottom is 108 m. When we compare the resolution of the beam (108 m) with the real size of the target (50 m), it is obvious that the beam-former couldn't spatially resolve the actual size of the target and we can just detect the target by beam-former. The results of the same target at 1000 m depth are shown in Figure 44.

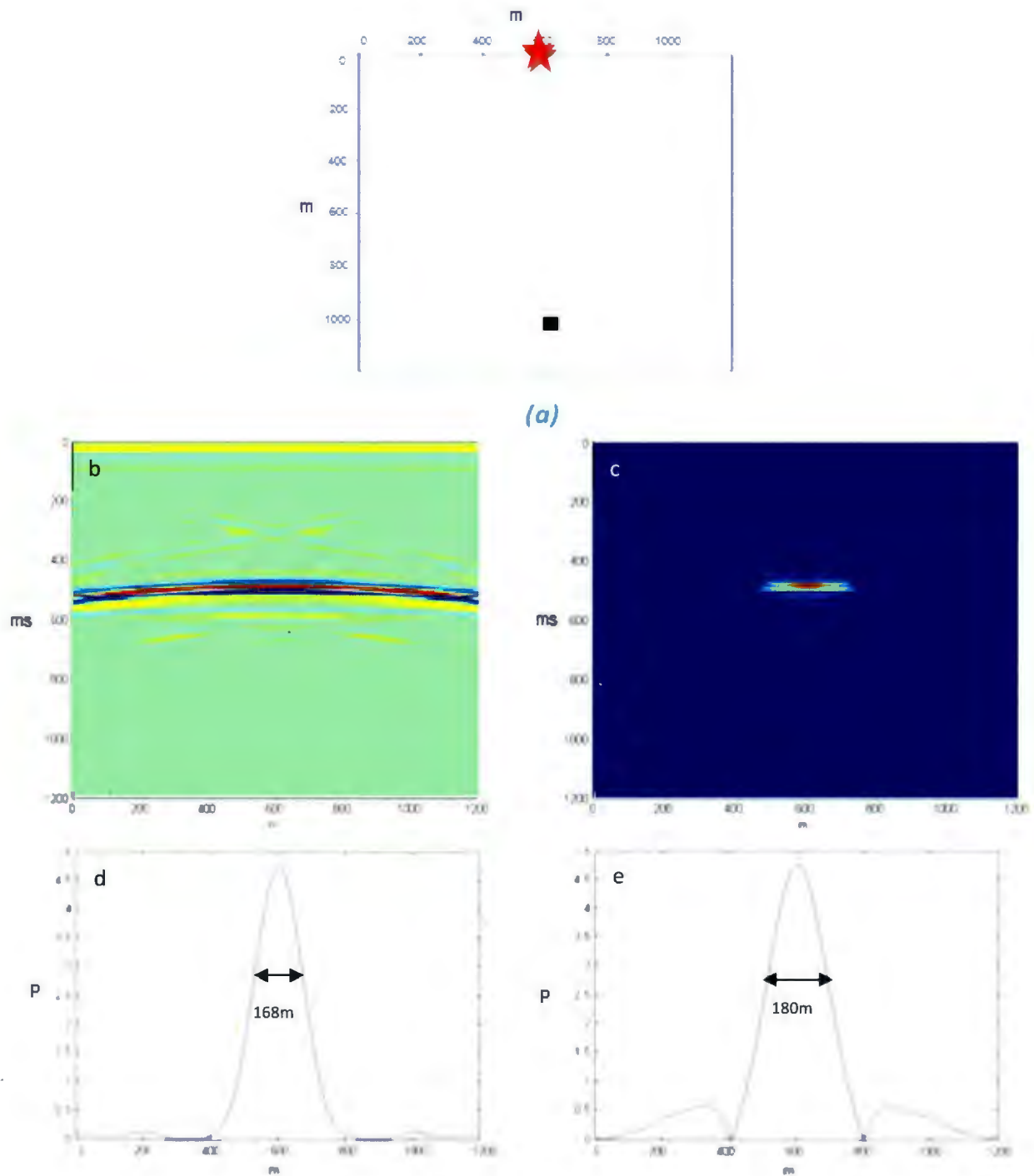
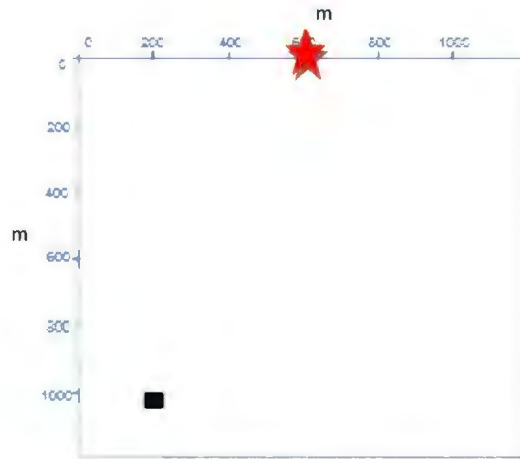


Figure 44: (a) Image showing a square scatterer. The white background represents the host rock (velocity = 4.5 Km/s), the black shape represents an ore body (velocity = 6.5 Km/s), and the red star is the source. This model is designed in Seismic Unix, (b) it is a shot gather, and (c) the result of the method. (d) & (e) 1-D representation of beam from top and bottom of the target respectively.

The ½ down point of the main-beam for the beam from the top is 168 m and from the bottom is 180 m. After comparing the results from two targets at different depth in test 1, it can be concluded that when the target is deeper the spatial resolution is lower. This is consistent with the increased size of the Fresnel zone at this depth. In addition, the comparison of the beam-width (168 m) and actual size of the target shows the beam doesn't resolve the true size of the target and only detects it.

4.3.3. Test 2: Target offset from the source which is at the centre of the array

After testing the beam-forming on the situation source and the target at the centre of the array, it is time to examine beam-forming on a target that is offset from the source. The main reason for this evaluation is that in the field we usually don't have prior information about the position of the target it could be everywhere in respect to the source. Figure 45 shows the tested model and its results. As can be seen, the beam-former effectively detects the target in this situation.



(a)

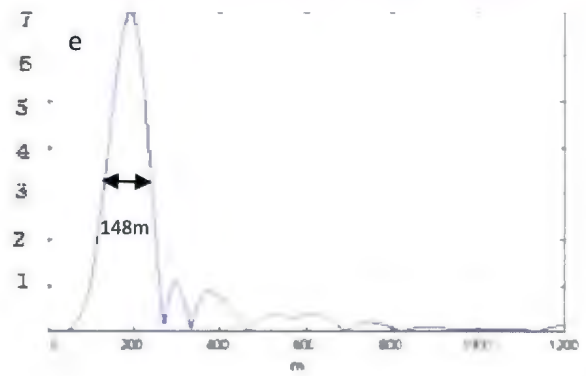
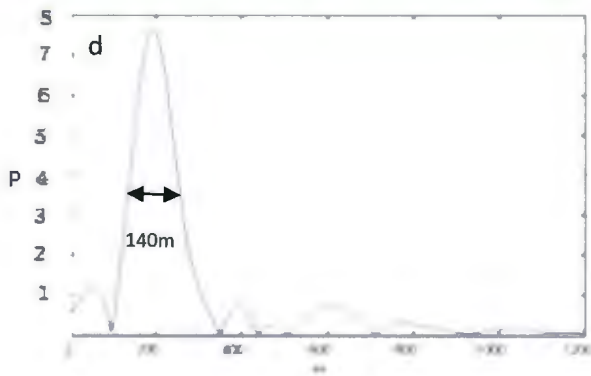
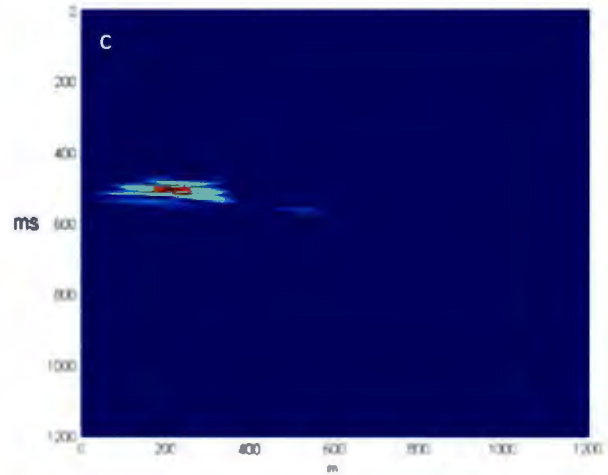
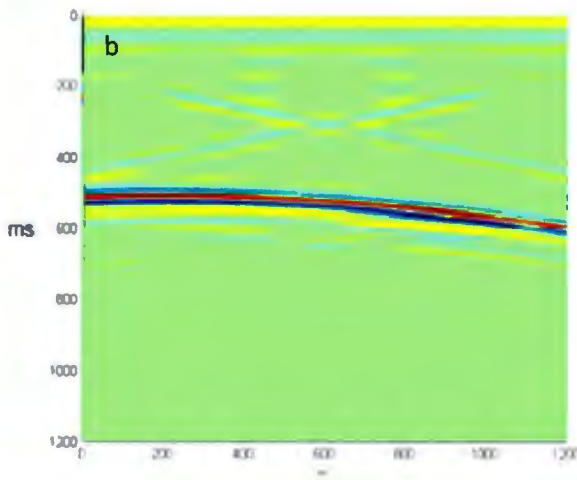


Figure 45: (a) Image showing a square scatterer. The white background represents the host rock (velocity=4.5 Km/s), the black shape represents an ore body (velocity=6.5 Km/s), and the red star is the source. This model is designed in Seismic Unix, (b) it is a shot gather, and (c) the result of the method.(d)&(e) 1-D representation of beam from top and bottom of the target respectively.

The $\frac{1}{2}$ down point of the main-beam for the beam from the top is 140 m and from the bottom is 148 m. The width of the beam is still higher than actual size of the target, so we could not characterize the target.

4.3.4. Source is at the centre of, the shapes and sizes of the target are variable.

In all of the examples that have been presented up to this point, the targets were fairly small in size in comparison with the Fresnel zone. Attention can now turn to examining the results of the beam-former in the case of larger targets.

In this section, various targets with differing sizes will be examined:

- Test 3: Rectangular target (400 x 50 m (depth= 400 m)) which simulates a lens shaped body.
- Test 4: Square target (200 x 200 m (depth=400 m)) which is simulates a large equidimensional geologic body.
- Test 5: A triangle target to compare with rectangular scatterer.
- Test 6: Lens shape scatterer with 40 degrees slope for examining the beam-response on a dipping target.

4.3.4.1. Test 3: Rectangular target(400 by 50 m)

As the first example in this section, the rectangular target of 400 m length and 50 m thickness at the depth of 400 m has been evaluated. This model is long (240% of Fresnel zone) in comparison with its width. This thickness is bigger than the theoretical temporal resolution which is 22.5 m for our models. The model can be seen in Figure 46.

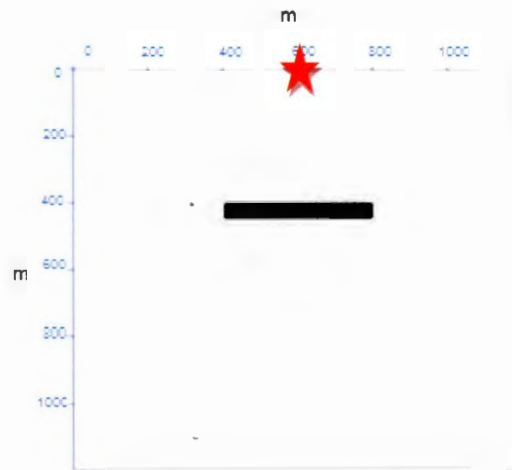


Figure 46: In this example target's dimension is 400 m by 50 m.

When examining the right and left sides of Figure 47(b), edge diffractions from four edges of the target can be seen.

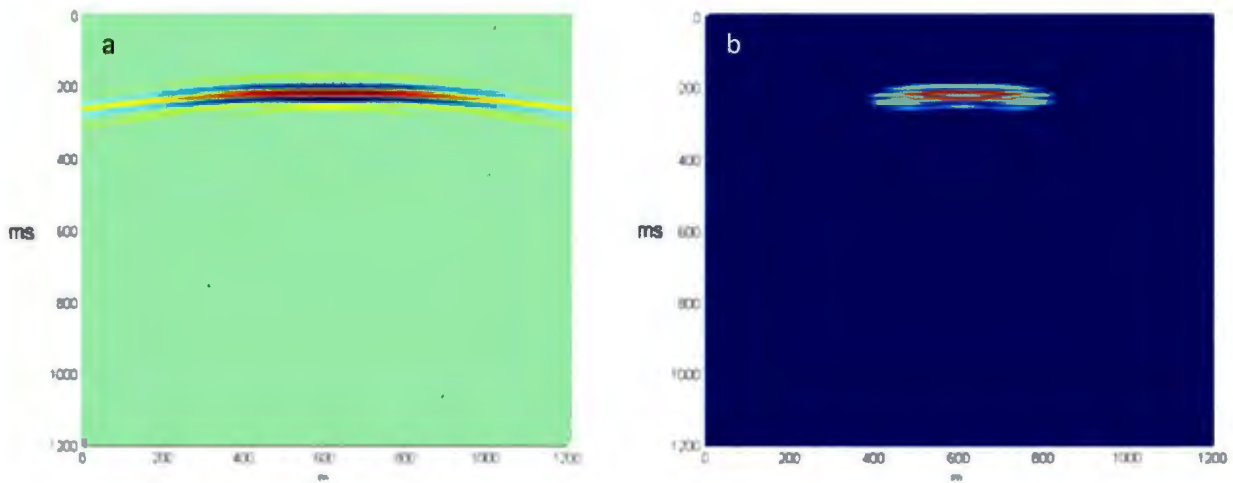


Figure 47: (a) The color version of the shot gather. Note the high amplitudes in the middle of the shot gather. (b) Result of beam-former. As can be seen in the Figure the top and bottom of the reflector are detected. In addition, if you look at two sides of the result you could see the diffraction results from edges of the target.

1-D beam representation from the top of the target demonstrates the peak of the beam and still gives us the center position of the target.

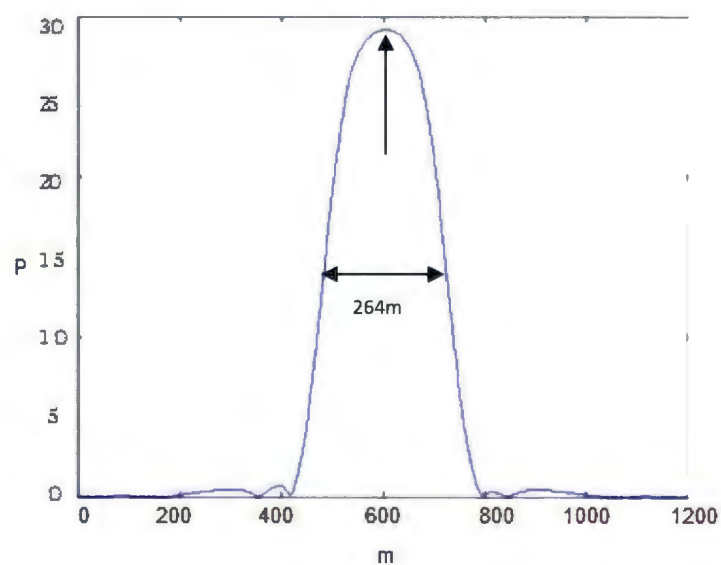


Figure 48: It is 1-D result from top of the target in to see how the response looks.

The ½ down point of the main-beam for the beam from the top is 264 m which follows the same trend as shown in Figure 38. Based on the experiment in 3.5.2.1, the larger the target the wider the beam-width is.

4.3.4.2. Test 4: Square Scatterer (200 by 200 m)

In this example, the target is 200 by 200 m and the depth is 400 m. It has larger dimensions. It is 120% of the Fresnel zone and 800% of temporal resolution. According to the shot gather, the recorded amplitudes from the top of the target are higher because the object is closer to the receivers, and it is expected to receive lower amplitude from the bottom of the data, which is deeper, at the depth of 600 m. Therefore, we can expect to get higher power in the beam-forming image from the top of the detected target, compared to the bottom of the target.

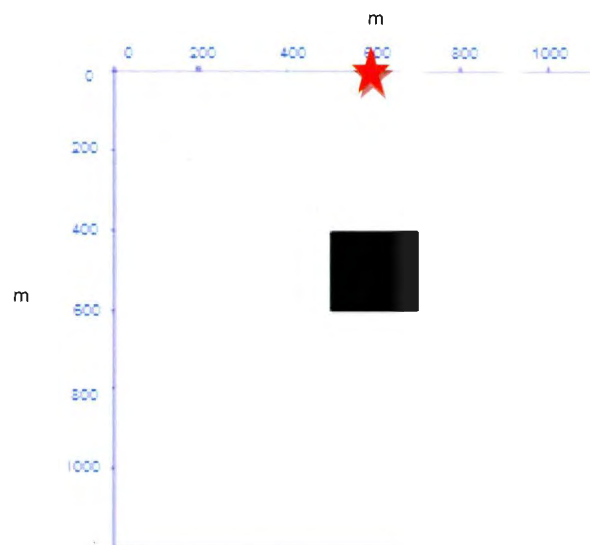


Figure 49. In this example the target's dimension is 200 by 200 m.

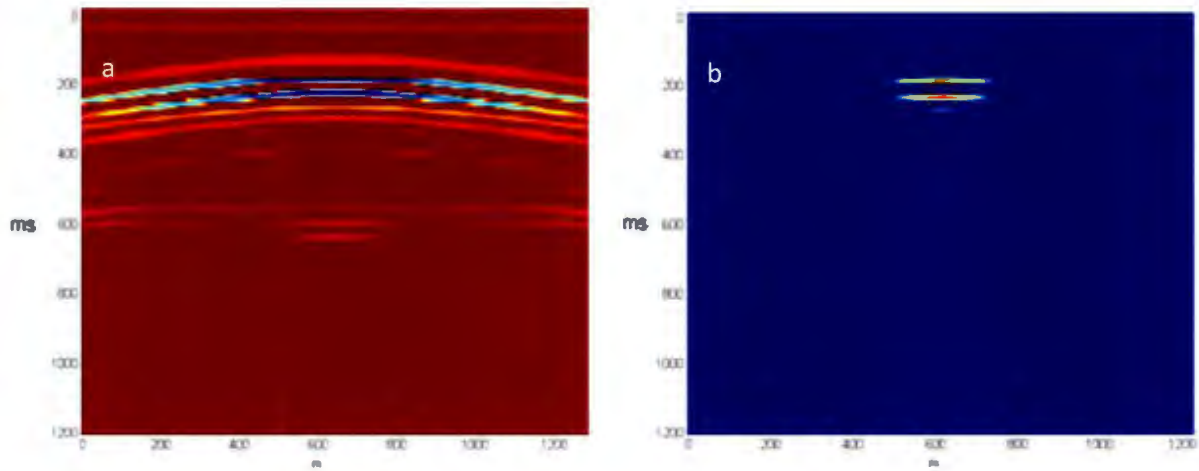


Figure 50: (a) The color version of the shot gather.(b) Result of beam-former. The top and bottom of the target can be distinguished in this figure.

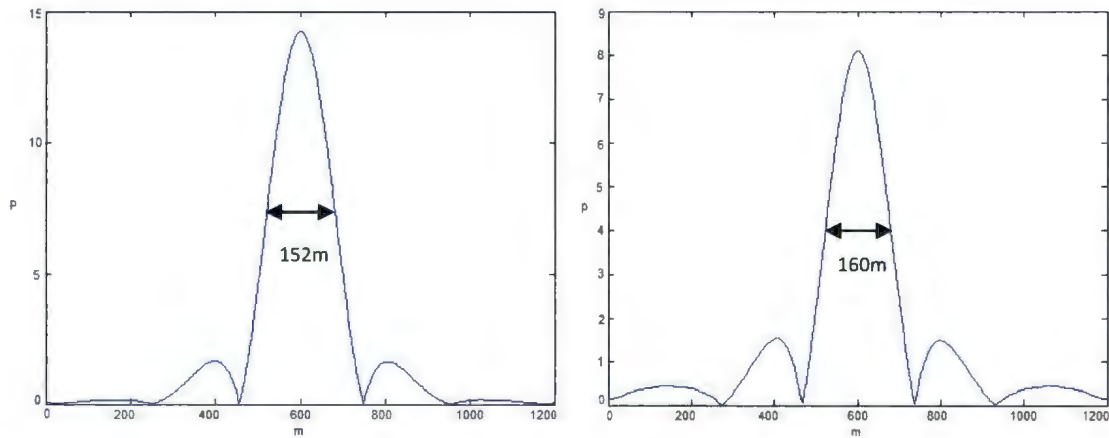


Figure 51: This figure shows 1-D beam from top and bottom of the 200 by 200 m rectangular model and shows us the spatial resolution.

The $\frac{1}{2}$ down point of the main-beam from the top is 152 m and from the bottom is 160 m which are smaller than the actual size of the target, and they are substantially different from the 50 m width square.

4.3.4.3. Test 5: Triangle Model

Another model, displayed in Figure 52, was investigated where the source and the scatterer were coincident in the middle of the array, and the shape of the target is an equilateral triangle. Its height is 50 m which is almost twice the quarter wave-length. The target is at a depth of 250 m. It is almost the same as the first model in test 1. The goal is examining the difference between these two models and target geometries.

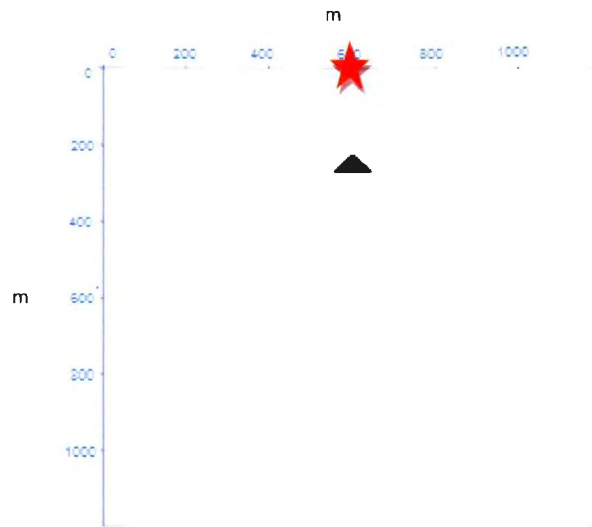


Figure 52. Triangle model in the depth of 400 m

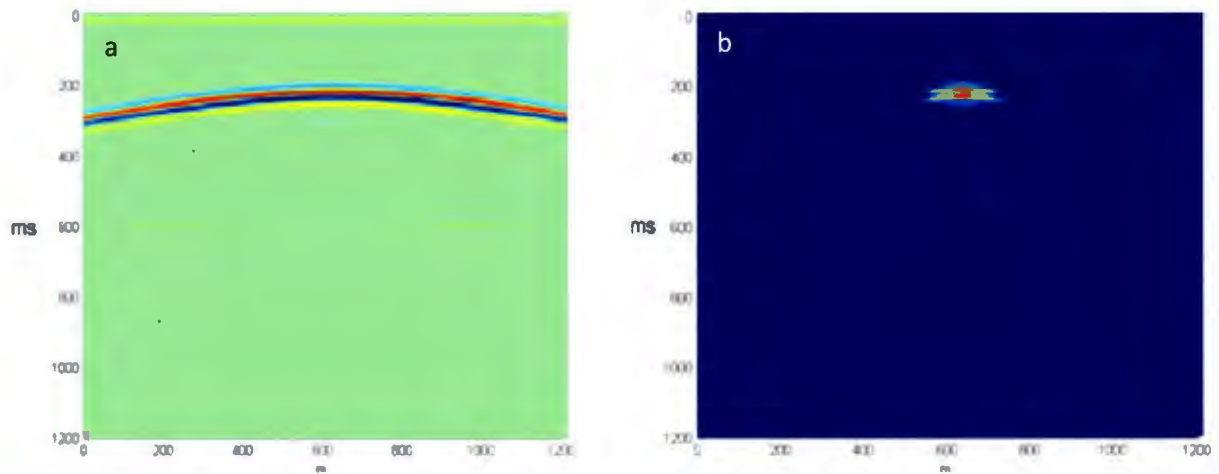


Figure 53: (a) shot gather from triangle model. (b) Beam-forming result from triangle model.

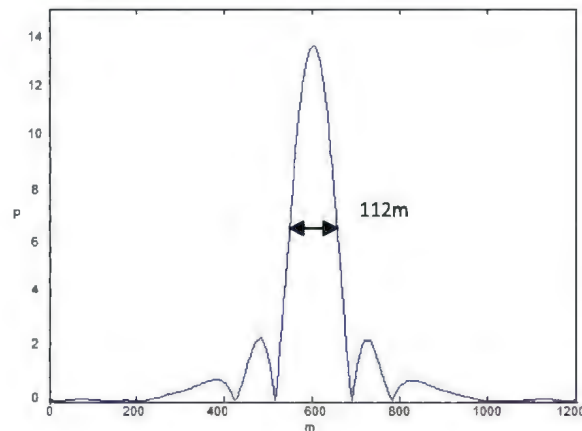


Figure 54: This Figure shows 1-D representation of the triangle model and shows us the spatial resolution.

The $\frac{1}{2}$ down point of the main-beam for the beam is 112 m. As can be seen, spatial resolution from the base of the triangle target is almost the same as main beam from the test 1.

Comparing this test and test 1 shows by this method we could not judge about the shape of the target, and we just detect the target.

4.3.4.4. Test 6: Lens-Shape Scatterer with 40 Degrees Dip

The following target is lens-shaped with a 40 degree dip, and it is closer to the end of the array. The source position is in the middle of the array. This model needs to be tested in order to evaluate the method of detecting a target with a dip. In this case, the top and bottom of the target are having the same trend. The model has been shown in Figure 55.

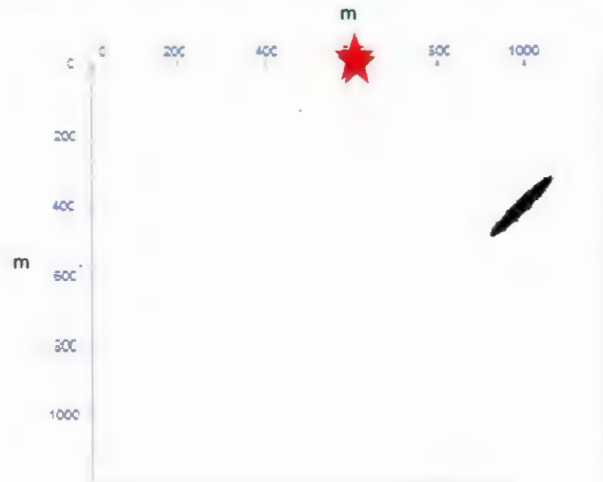


Figure 55: *Lens-Shape Scatterer with 40 Degrees Dip.*

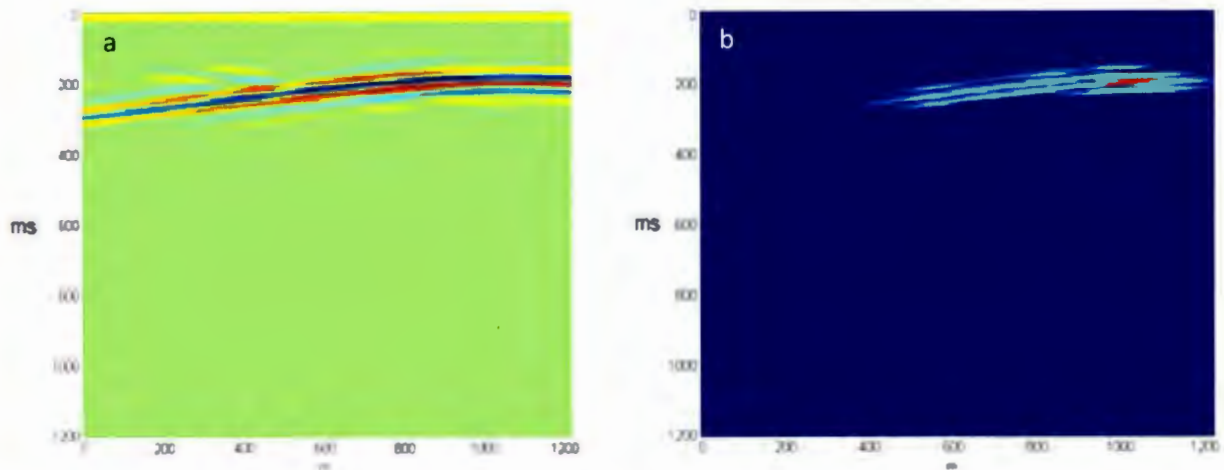


Figure 56: (a) Shot gather (color version) and (b) beam-former result.

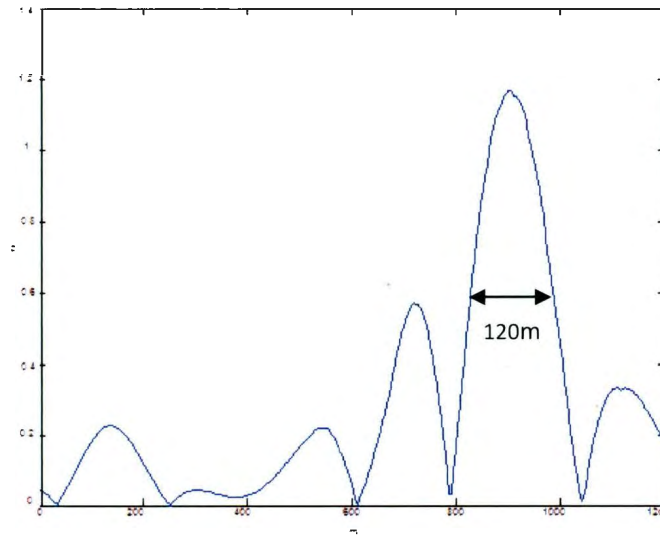


Figure 57-2 D representation of the target

As can be seen in the result, the target is detected by the beam-former, but the angle of the target is not clear in the result because the technique is not designed to recover the angle. What is clear here is that the dip results in an uneven distribution of amplitudes and a high down-dip side-lobe.

Up to here, different models with different shapes, dip and dimensions are examined. Another case that can be encountered in the real world is if we have more than one target in the model. How close can we detect two targets vertically and horizontally? In the next sections, models including two targets with different distances will be tested.

4.3.5. Horizontal & Vertical Detection Abilities of Beam-former

4.3.5.1. Test 7: 600 m Horizontal Distance

In the following examples, the ability to detect separate targets of the beam-former will be examined.

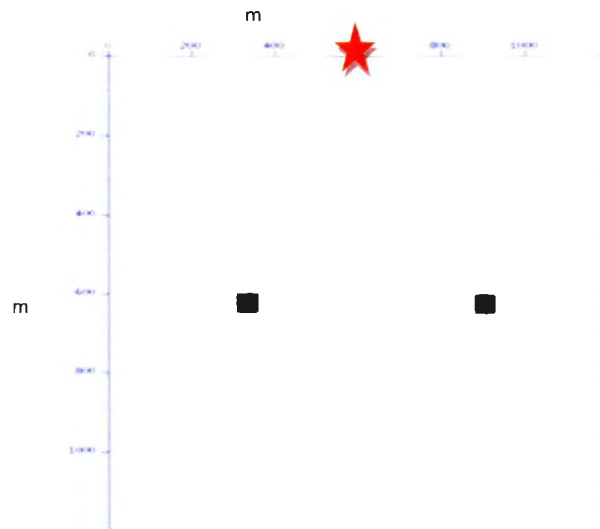


Figure 58. In this model, two separated target by the distance of 600 m can be seen.

The Fresnel zone for this experiment (target at the depth of 600) is approximately 155 m. According to the spatial resolution criterion, the two objects that are 600 m apart should be detected by the beam-former. However it is important to illustrate the beam-former performance for the case in which overlapping diffractions result in constructive interference and amplitudes are higher than the diffraction response (Figure 59). It might be expected that the beam-former would detect this part as a third target in the middle of the other scatterers, but if you look at Figure 60, the two targets are detected well.

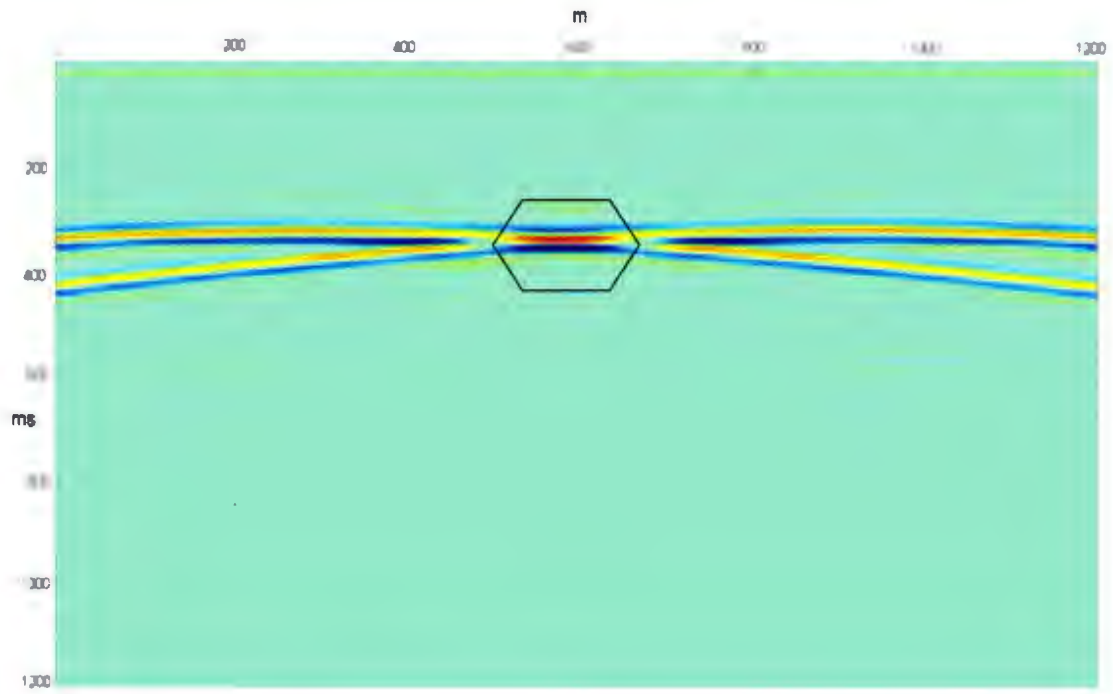


Figure 59: Shot gather from the model in Figure 58.

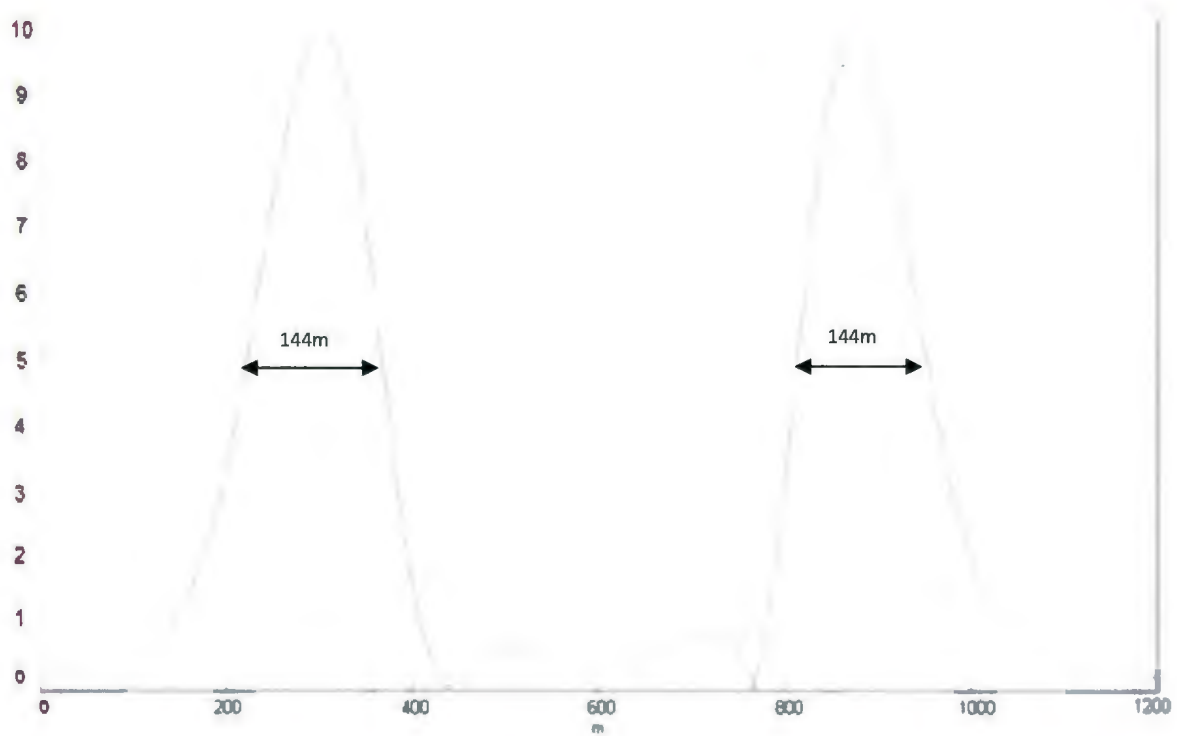
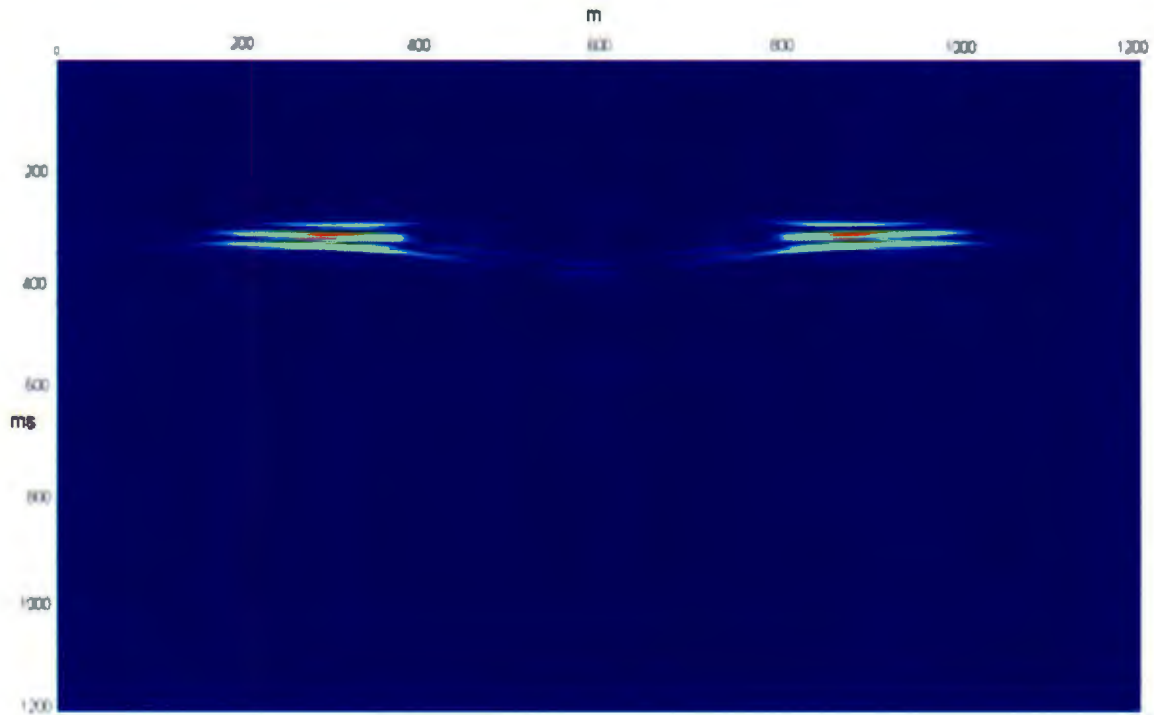


Figure 60: beam-forming result could be seen in this figure. As you can see the two targets distinguished as we expected from the calculation was made before starting application of beam-former.

The location of the source in this test and the following examples are in the middle of the array and between the targets. One reason for choosing the source in the middle of target is because we wish to compare results with those of Moffat(2002) (Figure 61 and Figure 62) who could only resolve the two targets if the source is not directly above the scatterers.

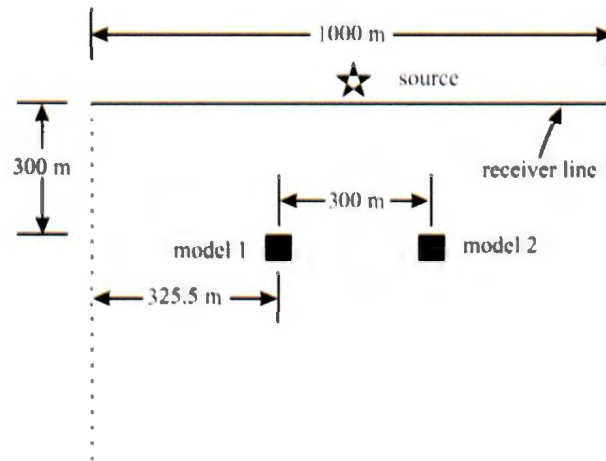


Figure 61: Geometry of two similar geological models representing adjacent massive sulfide deposits in the Moffat's experiment.

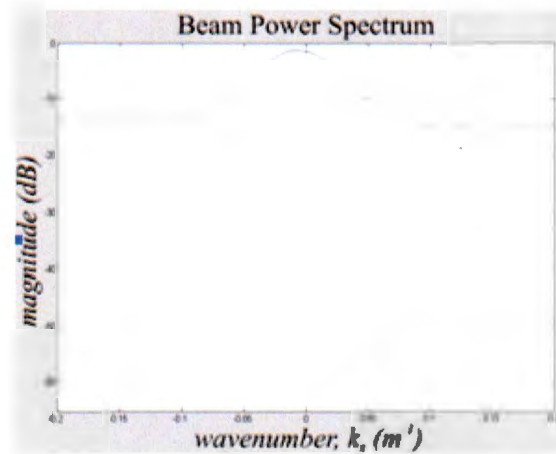


Figure 62: Beam-former response from Moffat's examples (2002) Beamformer couldn't resolve the targets.

4.3.5.2. Test 8: 200 m Horizontal Distance

The following figure is the result of two targets with the 200 m horizontal distance that is still bigger than Fresnel zone (125% of the Fresnel zone) at the same depth (600 m) as the preceding example. According to the calculation, it is still expected to distinguish these targets.

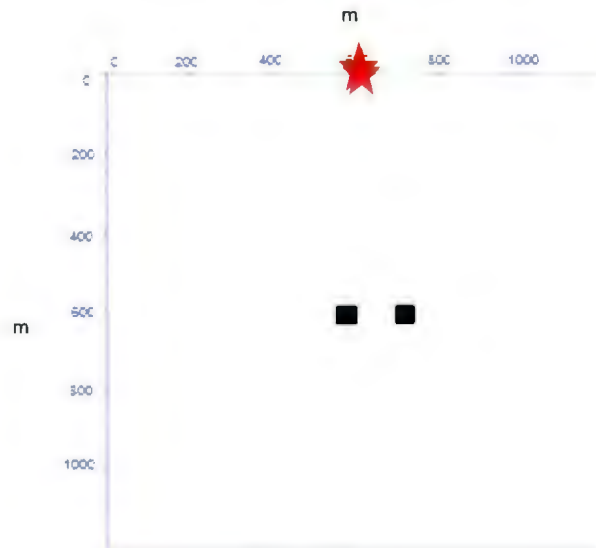


Figure 63: In this model, two targets separated by the distance of 200 m can be seen.

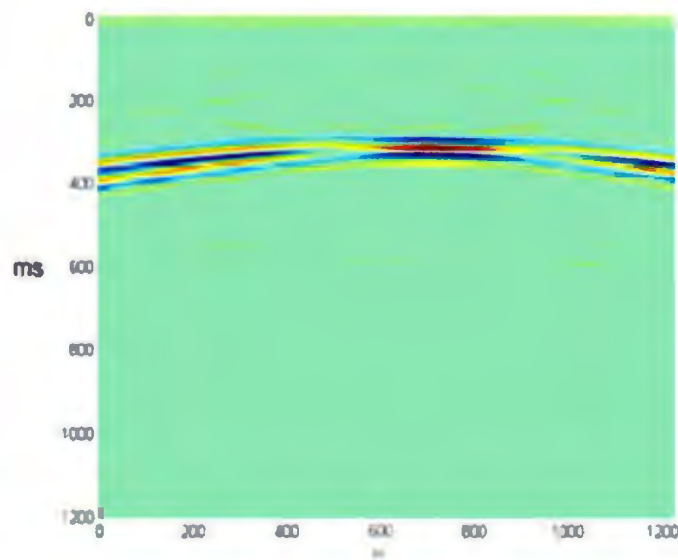


Figure 64: shot gather

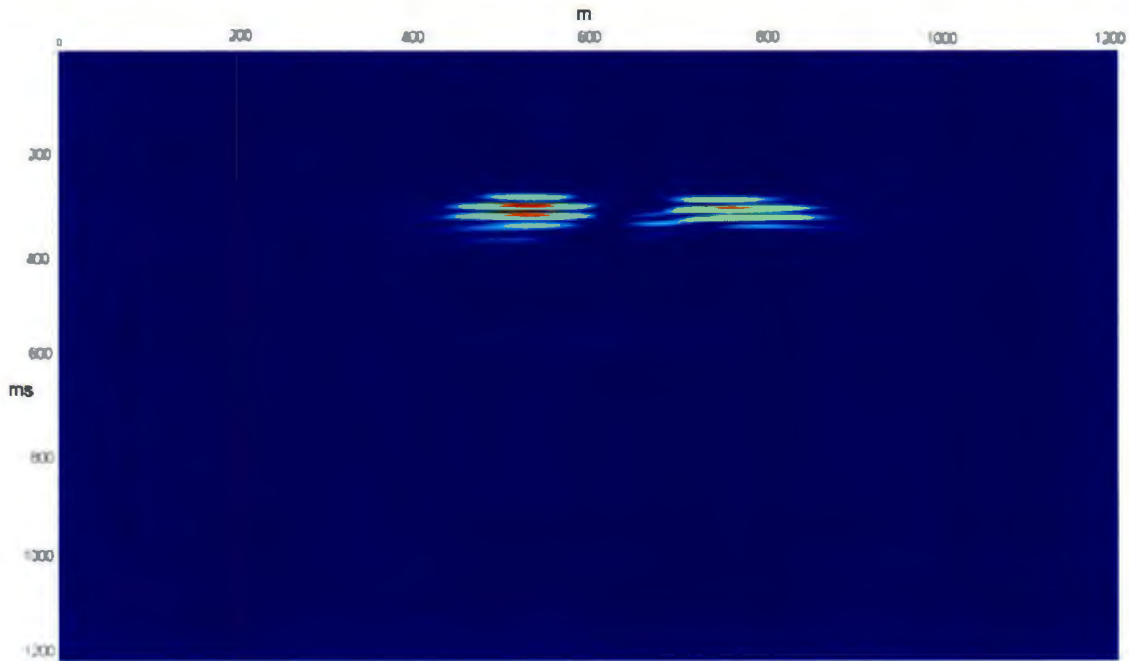


Figure 65: As it is obvious from the beam-former result, two targets are detectable.

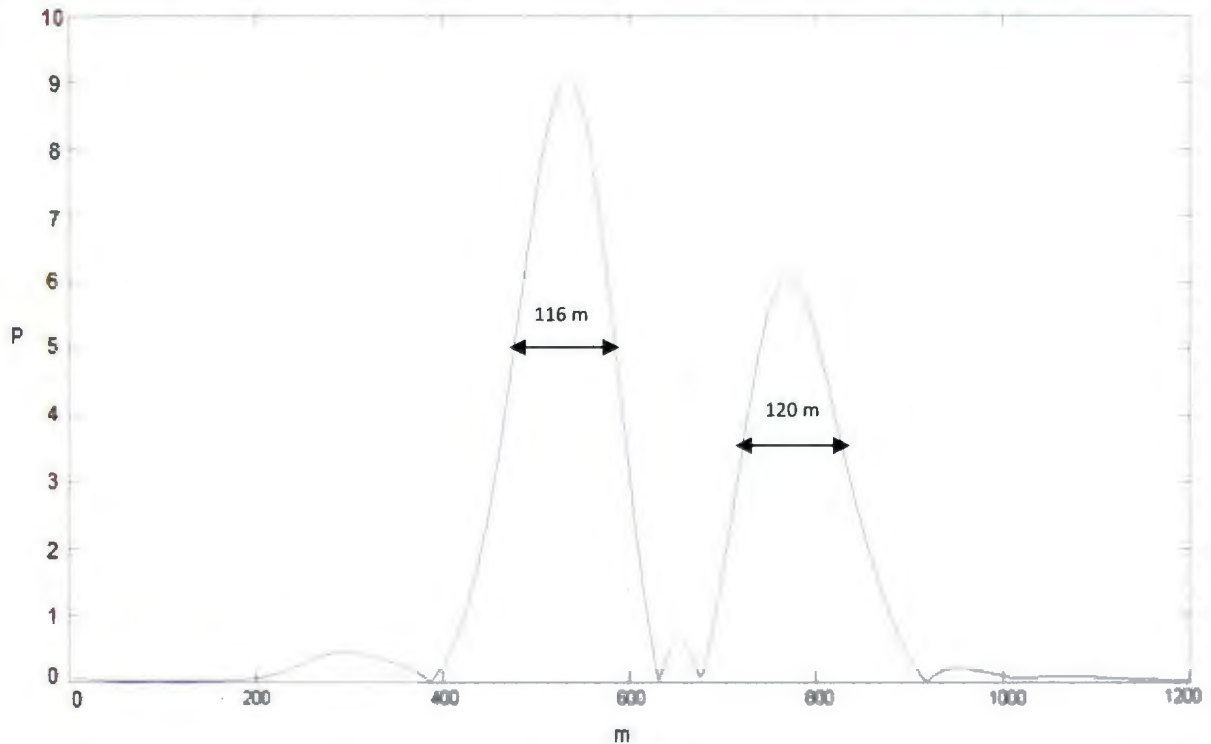


Figure 66: 1-D representation from top of the targets. Two targets are separately detected. The power difference is also because of the different distances of the targets from the source.

The importance of the previous diagrams highlights in the ability of the beam-former to detect and locate two close targets.

4.3.5.3. Test 9: 50 m Distance

In this model, the lateral space between targets is less than the theoretical spatial resolution (30% of the Fresnel zone). If you look at the outcomes in Figure 68, it can be seen that the beam-former is unable to distinguish between the targets. The detected scatterer looks like one rectangular target. The 1-D beam at the top of target also shows one peak.

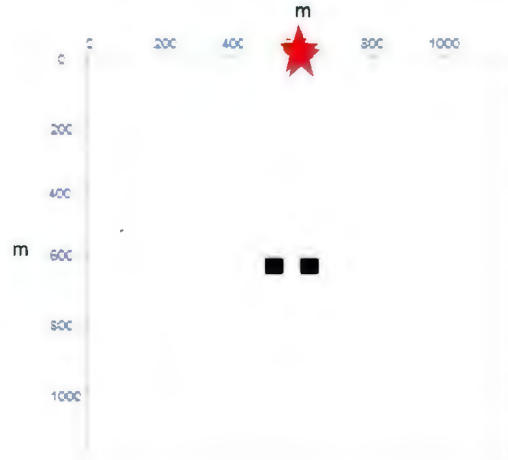


Figure 67: In this example, the targets are closer together and the distance between them is 50(m) (30% of the Fresnel zone) so according to the definition of the horizontal resolution, we could not separate them.

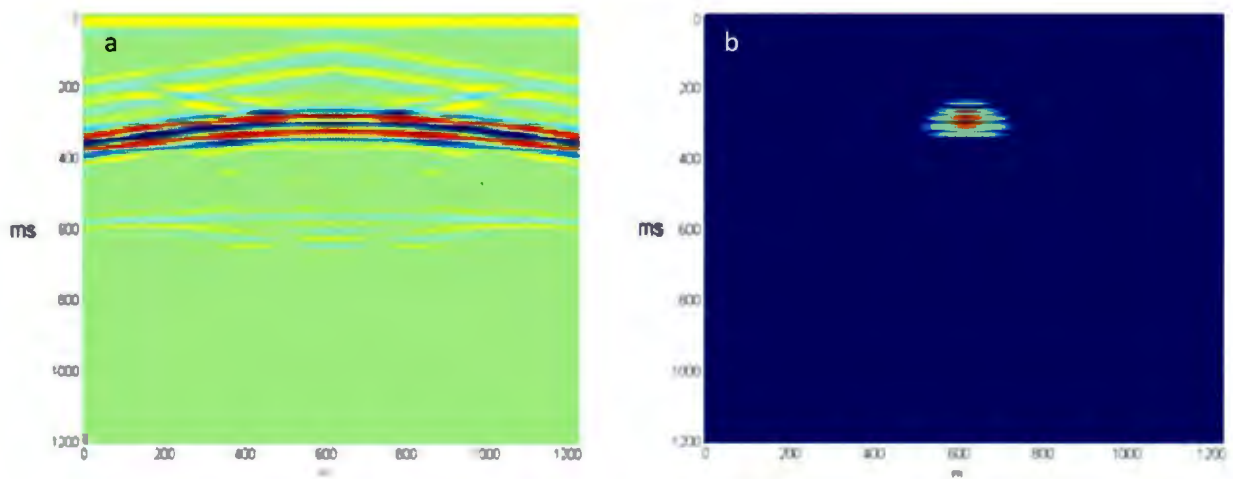


Figure 68 a) shot gather (color version). b) the result shows the beam-former detects two separated target as one longer rectangular target.

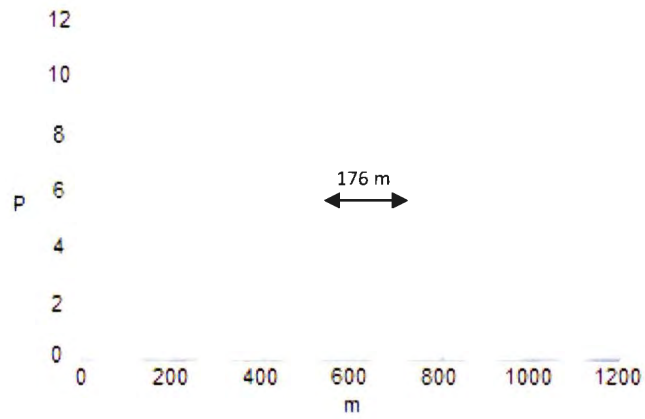


Figure 69: 2-D representation from top of the Figure 68.

In the next section, we study the beam-forming results in the case of two scatterers at different depths.

4.3.5.4. Test 10: 50 m Vertical Distance

In this model, targets are 50 by 50 m. The background velocity is 4500 (m/s) and the targets' velocity is 6500 (m/s). Two targets have 50 m depth difference which is more than the theoretical temporal resolution (which is 22.5 m).

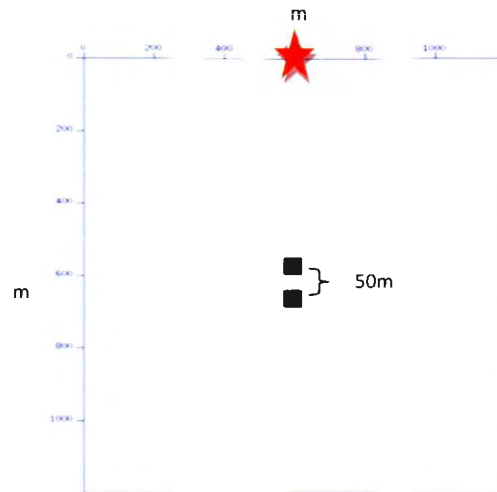


Figure 70: In this model two targets have 50m depth difference

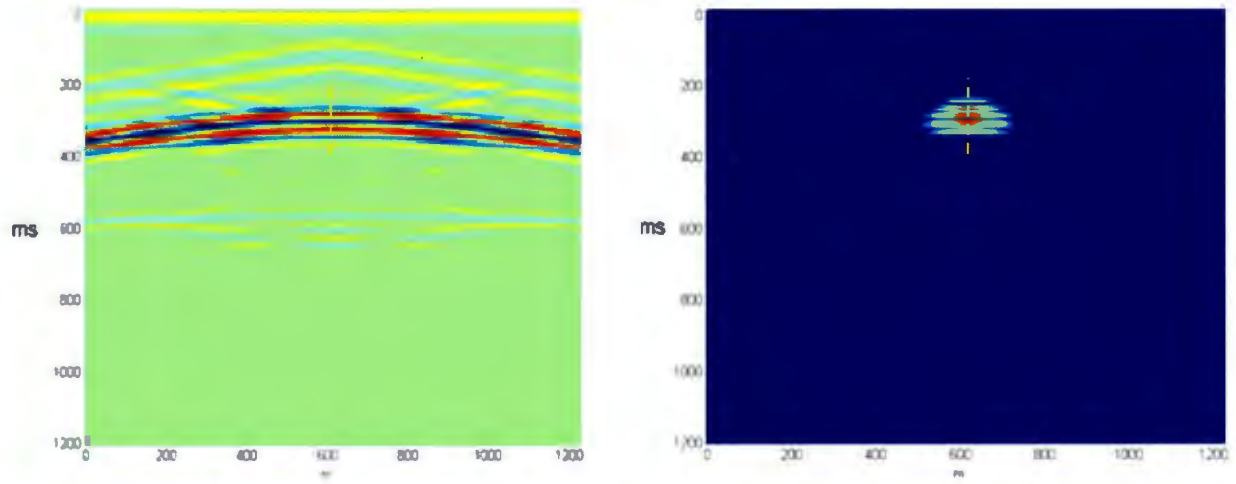


Figure 71: Left) Shot gather from the model. Right) two targets were detected by beam-former. The dashed line is the part of 1-D representation shown in the next Figure.

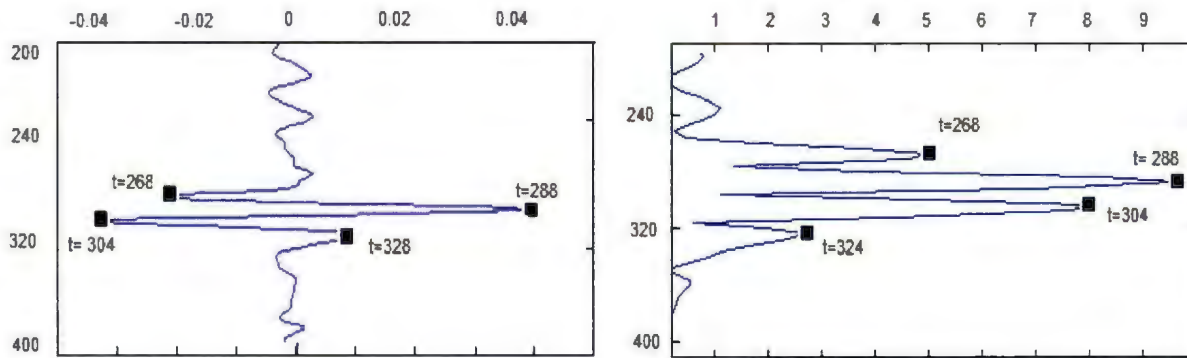


Figure 72: 1-D representation from middle of the shot gather and beam-power in Figure 71 to show the targets are distinguishable. Both top and bottom of the targets can be seen in the graph.

According to the result, the two targets are completely distinguishable. Top and bottom of the both targets represents 4 peaks in the 1-D beam power plot in Figure 72. The bottom of the upper target and top of the lower target are also distinguishable.

4.3.5.5. Test 11: 30 m Vertical Distance

The only difference between this example and the last one is the distance difference between targets, which is 30 m.

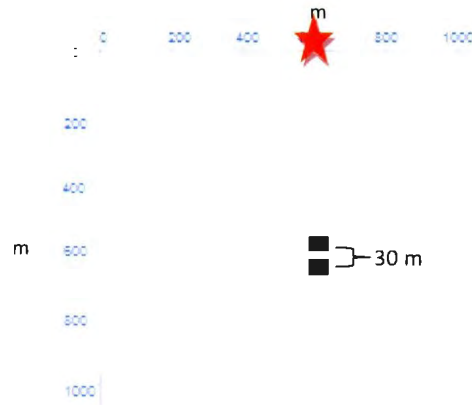


Figure 15. In this mode, the depth difference is 30 m, which is close to the $\lambda =$

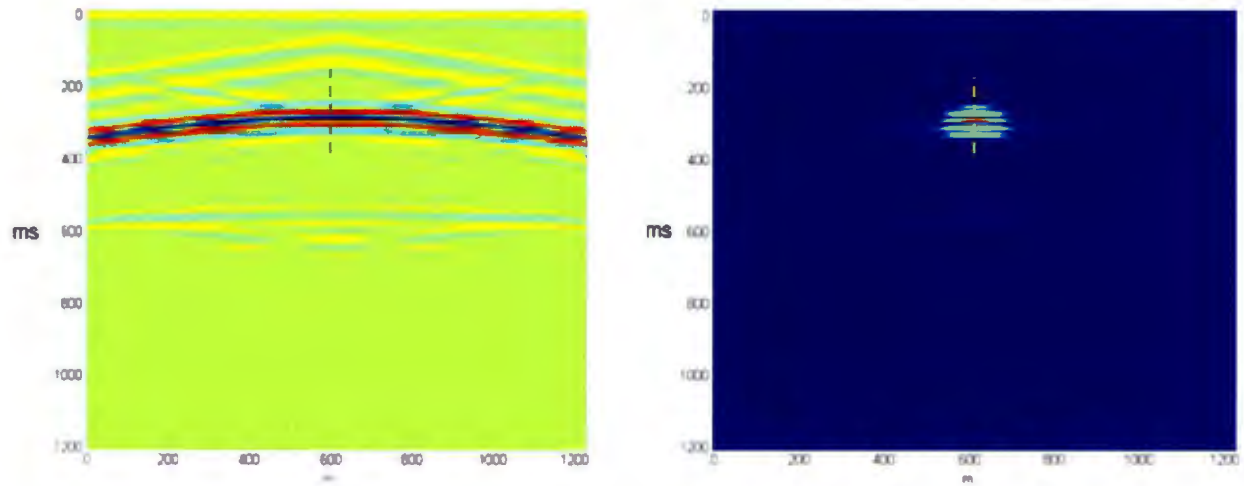


Figure 74: left) Shot gather from the model in Figure 73. Right) two targets were detected by beam-former. The dashed line is the part of 1-D representation shown in the next Figure.

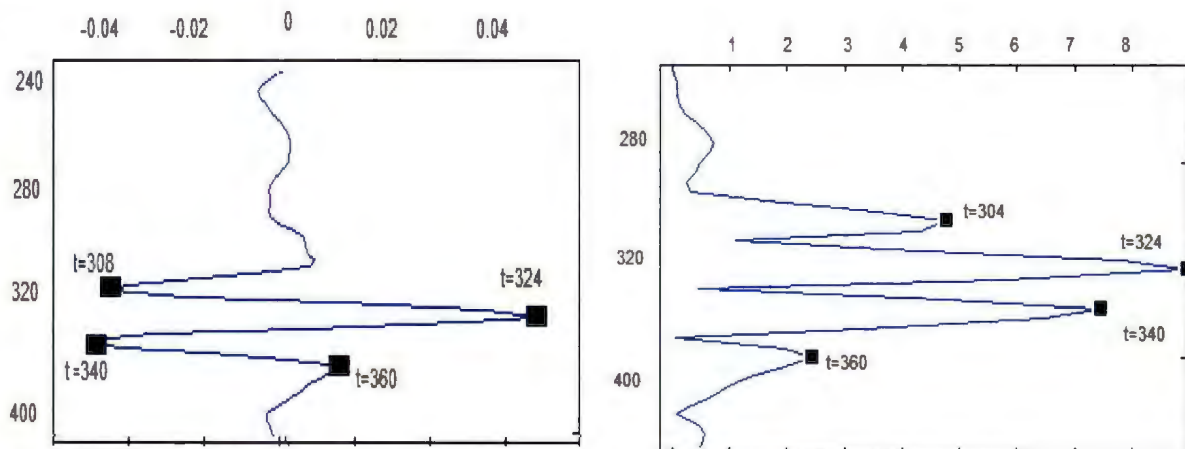


Figure 75: 1-D representation from middle of the shot gather and beam-power in Figure 74 to show the targets are distinguishable. Both top and bottom of the targets can be seen in the graph.

The result demonstrates, as would be expected that the targets are still detectable separately. The bottom of the upper target and top of the lower target are still distinguishable. In the next section, focus will be on different array sizes.

4.3.6. Gap Along the Array Line

The next set of examples is designed to test the beam-former in the following situations:

- When there are dead geophones along the array and when we have restrictions on placing geophones in a part of the array, because of geographical obstructions such as trees or marshes.
- When there are variations in elevation on the array lines

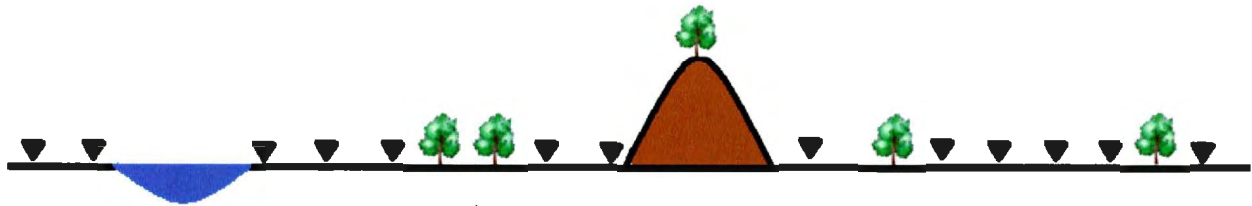


Figure 76: in this cartoon some limitations along array were shown. Black triangles are receivers.

The target used in this section to evaluate our technique is the square target (50 by 50 m), at the depth of 250 m. Array length is 1196 m and the array response is in the near-field.

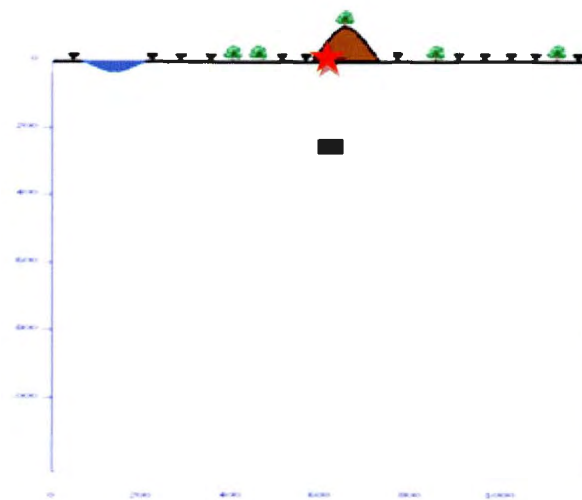


Figure 77: there are a few areas in which no data is recorded

4.3.6.1. Test 12: Random Gaps Along the Array

In the first example Figure 78, there are a few areas in which no data is recorded. The gaps in the array range from 8 m to 80 m. The intention is to examine whether the target could be detected or not in these kinds of situations.

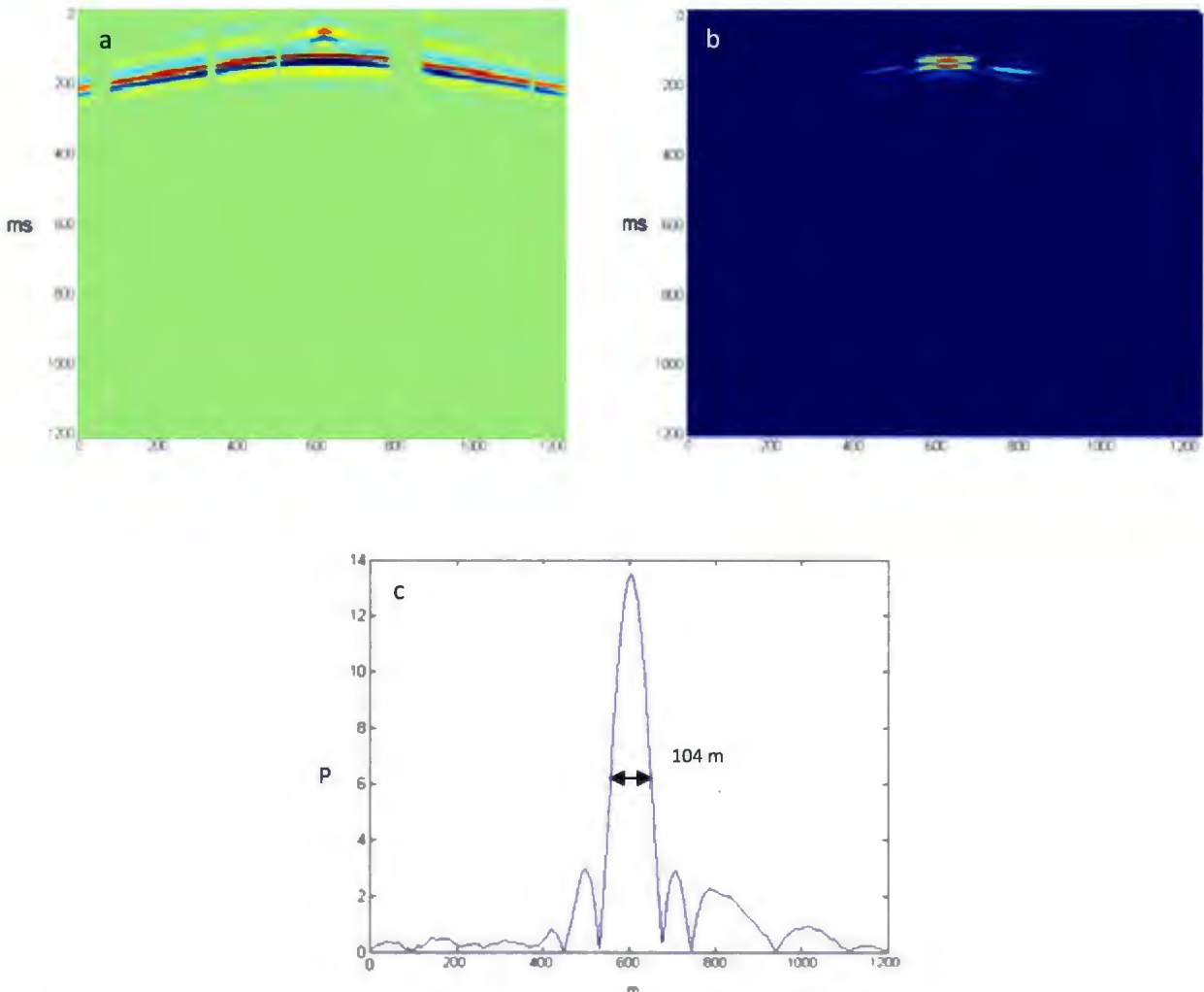


Figure 78 (a) Shot gather. (b) beam-forming image could be seen in this figure. Top and bottom of the target was detected. (c) The 1-D representation of the top of the target.

Based on the result the target was detected even if in some areas the data didn't record data.

4.3.6.2. Test 13: Obstruction to Record Apex of the Hyperbola

An example demonstrating the affects of missing data at the apex of the diffraction is shown in Figure 79. The target is the same depth as in previous examples. According to the results, even if part of the apex could not be recorded, the target is still detectable. However the primary to side-lobes ratio is decreased.

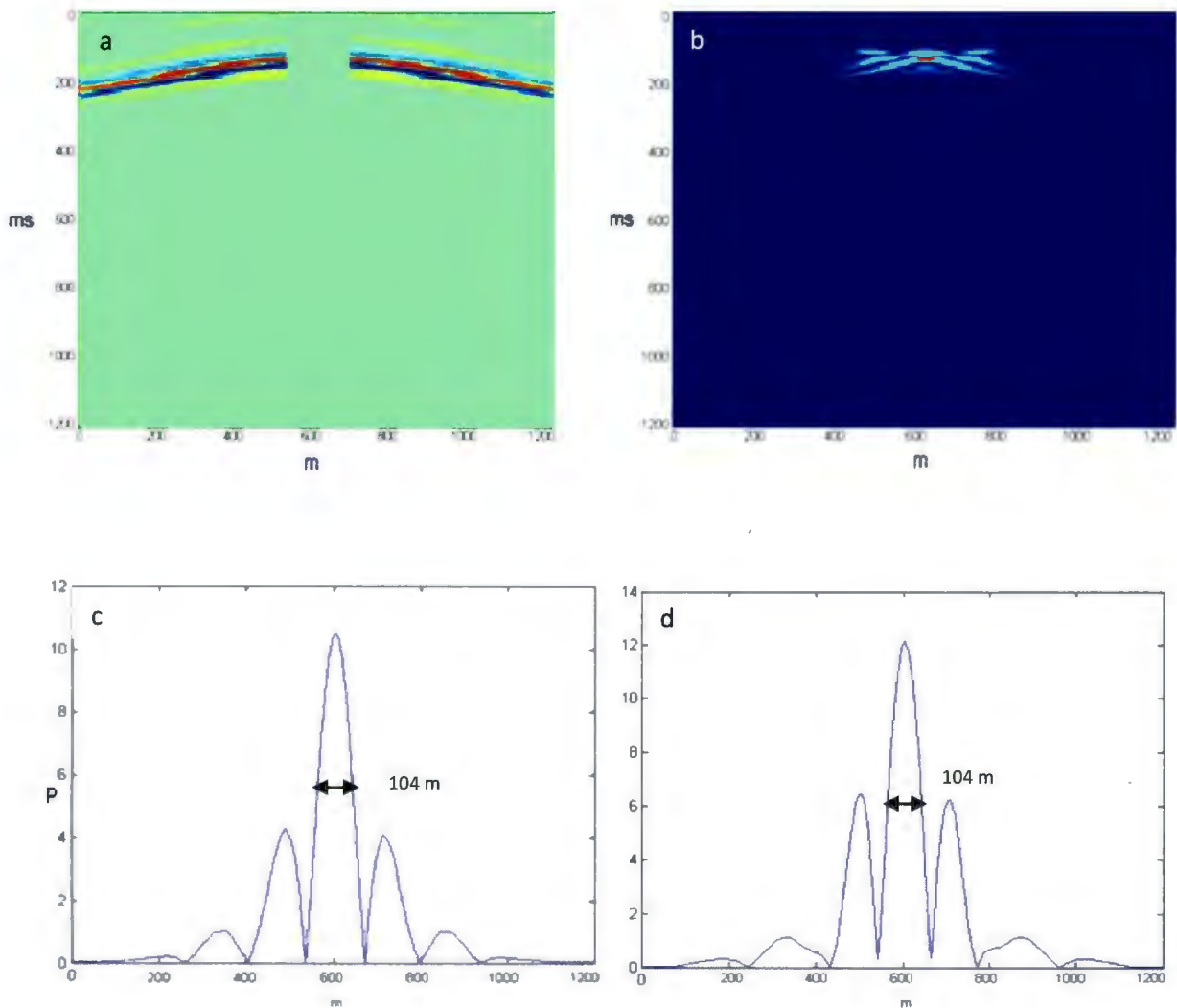


Figure 79: (a) Shot gather. (b) beam-forming image could be seen in this figure. Top and bottom of the target was detected. (c), (d) The 1-D representation of the top and bottom of the target respectively.

4.3.7. Affects of Noise on Beam Performance

A popular and sensible approach to experimental design in most literature is to add Gaussian noise to the data. Adding Gaussian noise has some deficiencies:

- Gaussian noise is broad band in comparison with the signal.
- This noise is uncorrelated trace to trace while in seismic data noise is generally correlated.
- Measurement of the signal to noise ratio as defined in this study doesn't account for coherence of the signal.

Consistent with other examples in the literature (Jeng et al., 2009), noise has been added to the synthetic data in our experiments. In this section, after describing the method used to add Gaussian Noise to the data and defining the signal-to-noise ratio, the response of the beam-former to different noise environments is explored. The same data as Figure 42(a) was used for the determination of beam-former results to the different signal-to-noise ratios. In this noise analysis, the incoherent noise adds to mask the coherent signal, and the goal is to examine how well the beam-former can identify coherent signal imbedded with random noise.

4.3.7.1. Description of MATLAB Code

For adding the white Gaussian noise, the '*awgn*' command from the Communication Toolbox in MATLAB was used. $y = awgn(x, snr)$ adds white Gaussian noise to the vector signal x . The scalar SNR specifies the signal-to-noise ratio per sample, in dB. For instance, this command is used below to add white Gaussian noise to a saw-tooth signal. Both signal and noise are plotted in the Figure 80 and Figure 81.

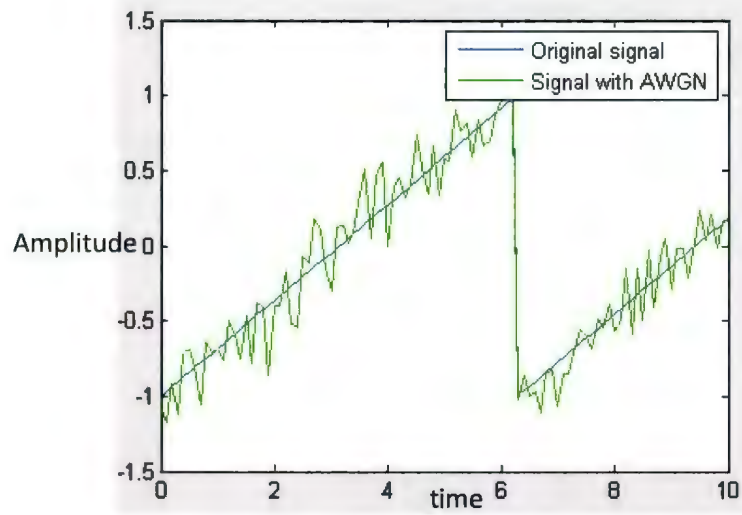


Figure 80: In this figure, the effect of adding Gaussian noise in the simple example was shown.

In the case of the beam-forming experiments this command can be used to add Gaussian noise to the data. Below, the recorded data with noise is compared to the data without noise from the scatterer at the depth of 600 m.

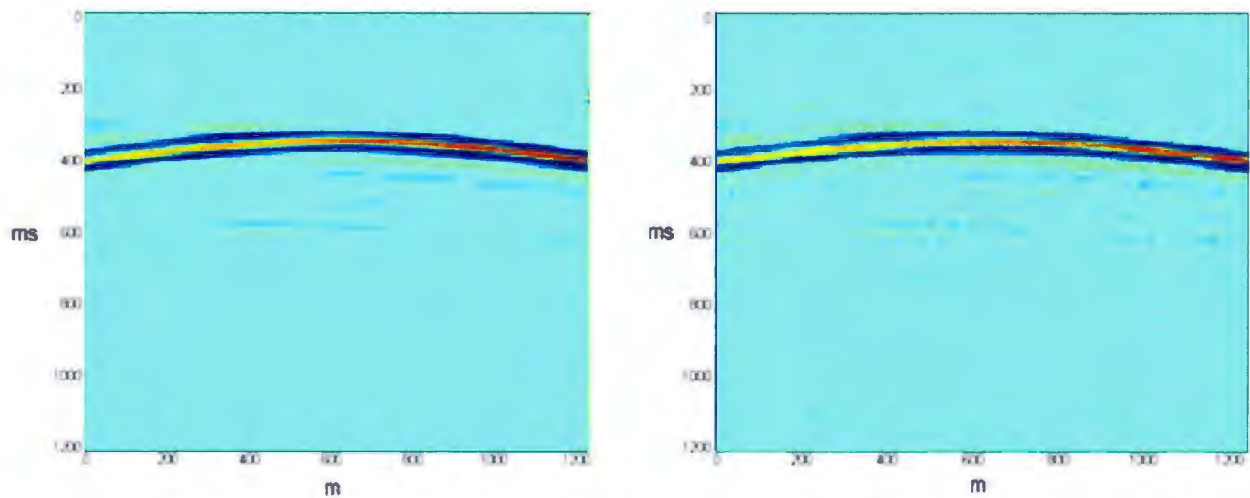


Figure 81: Model before adding Gaussian noise after adding Gaussian noise

4.3.7.2. Signal-to-Noise Ratio

In many of the published studies on this topic (Jeng et.al., 2009), the author mentions the addition of Gaussian noise without adequately explaining its purpose or meaning. To determine the signal-to-noise ratio, the following formula has been used:

$$\text{Signal to Noise Ratio} = \frac{P_{\text{signal}}}{P_{\text{noise}}} = \frac{\sum \text{signal amplitude}^2}{\sum \text{noise amplitude}^2} \quad 8$$

For calculating the signal-to-noise ratio, we need to determine the noise section without the signal. To do that, the signal will be subtracted from the data after adding the Gaussian noise.

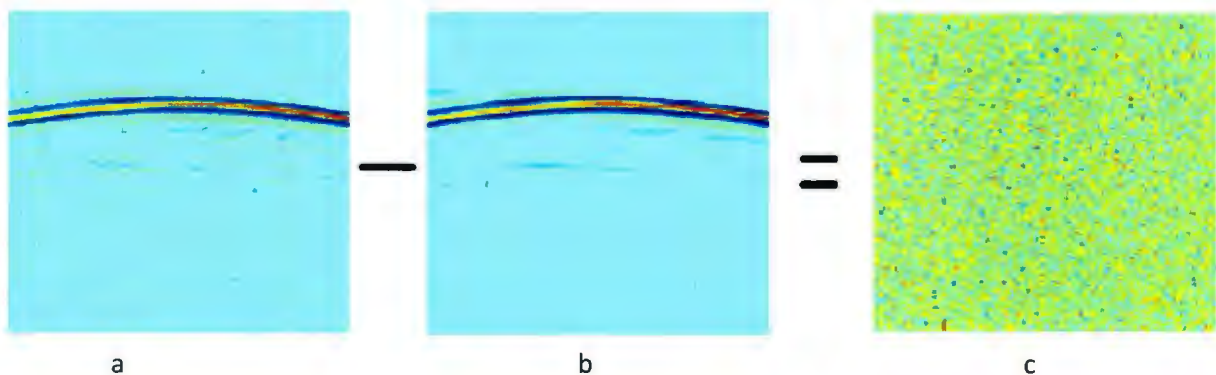


Figure 82: a) signal plus Gaussian noise b) Signal c) Noise

This calculation is made on the same defined window for all examples in MATLAB (Appendix C). The window used to determine signal-to-noise ratio is consistent for all examples and is 180 ms in time axis and 1196 m in length. The chosen window includes the signal completely.

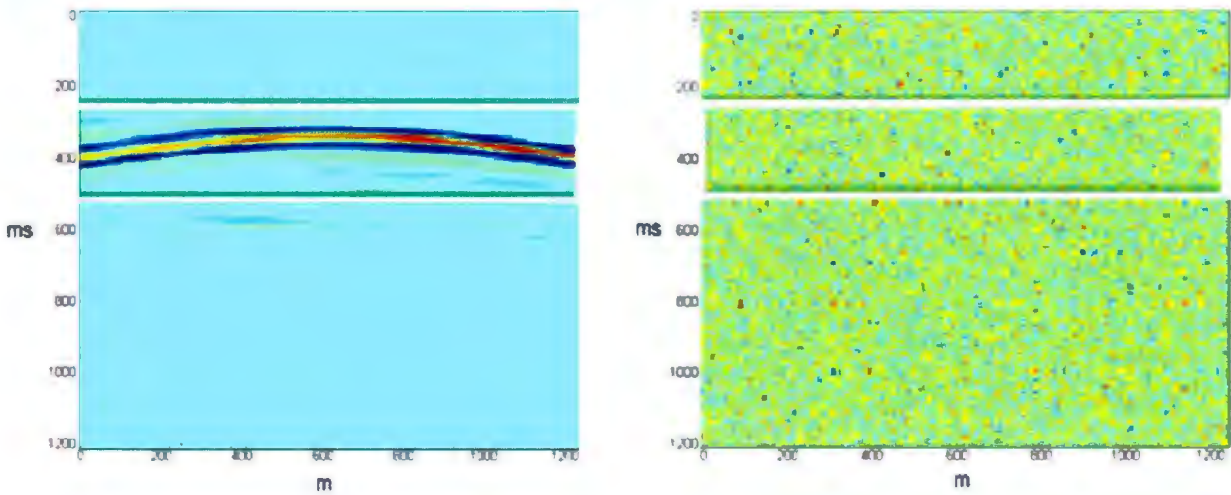


Figure 83: Trough white windows signal calculated from left figure and noise calculated from right figure. The window used to determine signal-to-noise ratio is consistent for all examples and is 180 ms in time axis and 1196 m in length. The chosen window includes the signal completely.

For this specific case the calculated signal-to-noise ratio is 16.9. This method of signal-to-noise estimation provides an internally consistent estimation for comparing the models in this study but is not an indicator of global signal-to-noise ratio.

4.3.7.3. Beam-former Performance on Data with Noise

In this section we demonstrate beam performance on a range of examples with decreasing signal-to-noise ratio. The model in which the source and the target are at the centre of the array was chosen for these examples. The square scatterer by dimensions of 50 by 50 m at a depth of 250 m has been analyzed. To have a better visualization of the beam-former, one-dimensional beams on the top and bottom of the detected target were given.

4.3.7.3.1. Test 14

For this example, the Signal-to-noise ratio equals 5.8.

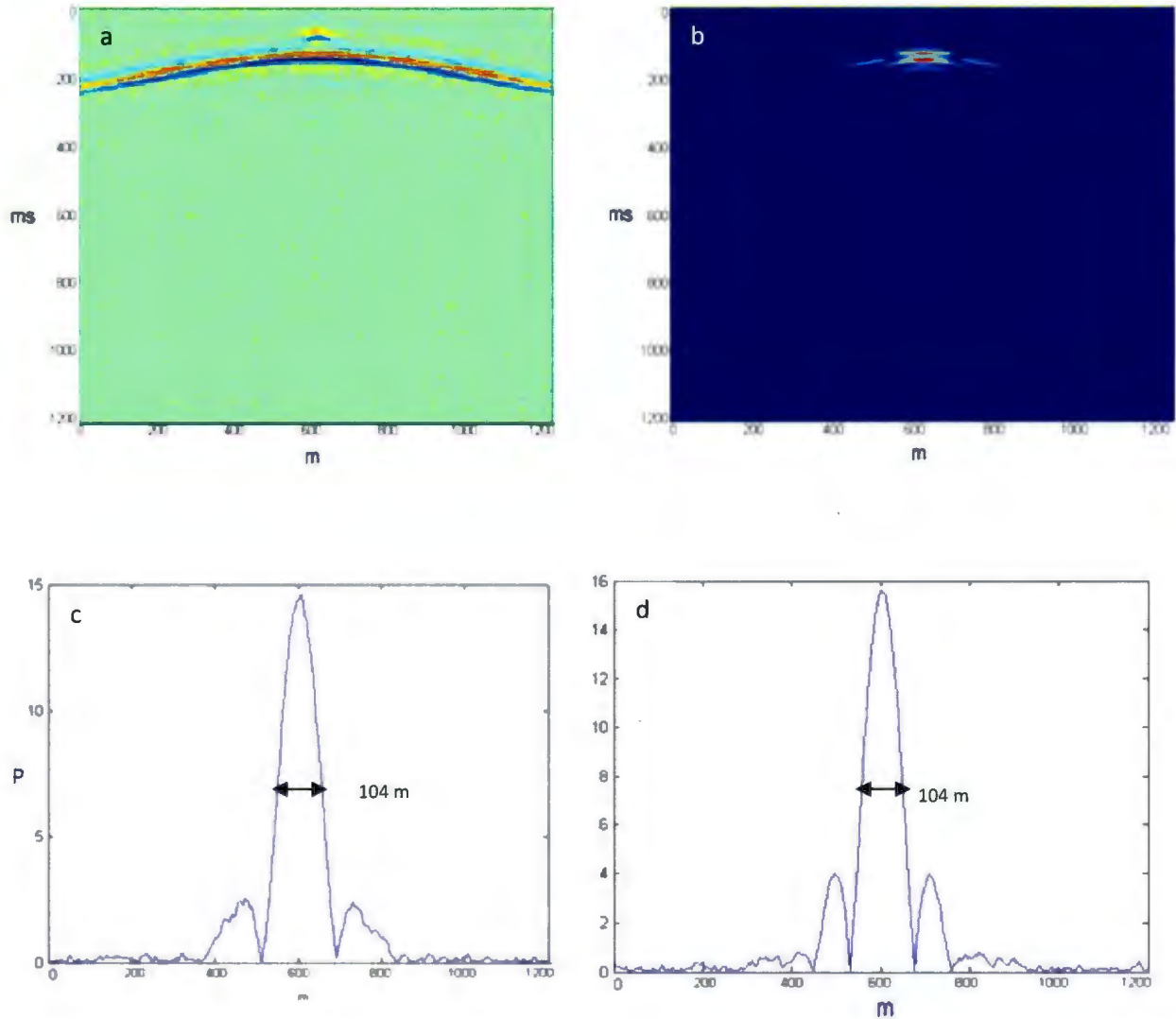


Figure 84: (a) shot gather (b) beam-former image (c) & (d) 1-D representation of beam from top and bottom of target respectively.

The $\frac{1}{2}$ down point of the main-beam for the beam from the top is 104 m and from the bottom is 104 m.

4.3.7.3.2. Test 15

Here the signal to noise ratio is 1.6.

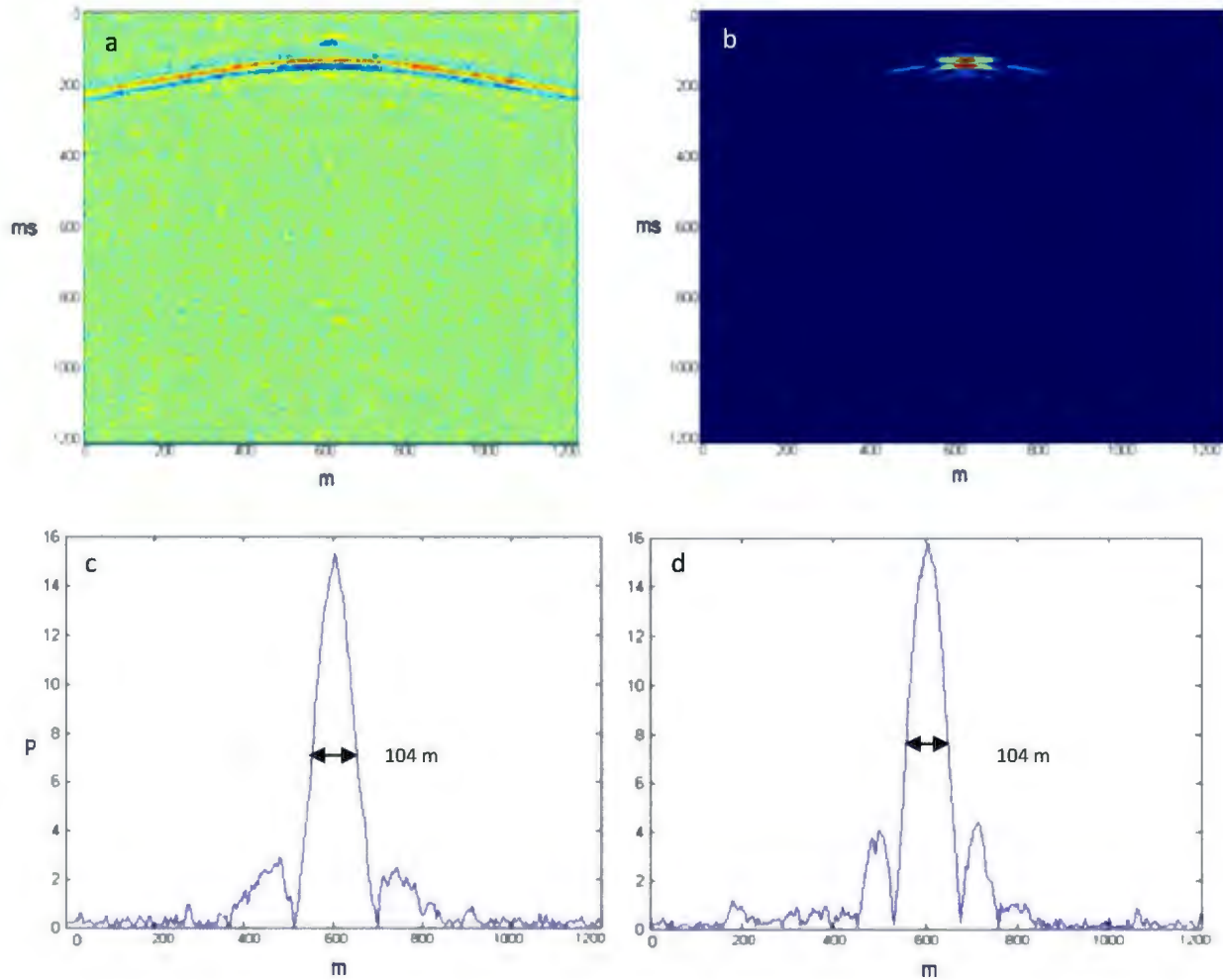


Figure 85: (a) shot gather (b) beam-former image (c) & (d) 1-D representation of beam from top and bottom of target respectively.

The $\frac{1}{2}$ down point of the main-beam for the beam from the top is 104 m and from the bottom is 104 m. Some fluctuation on side-lobes can be seen which is because of the noise.

4.3.7.3.3. Test 16

The signal-to-noise ratio decreased to 0.5 in this model.

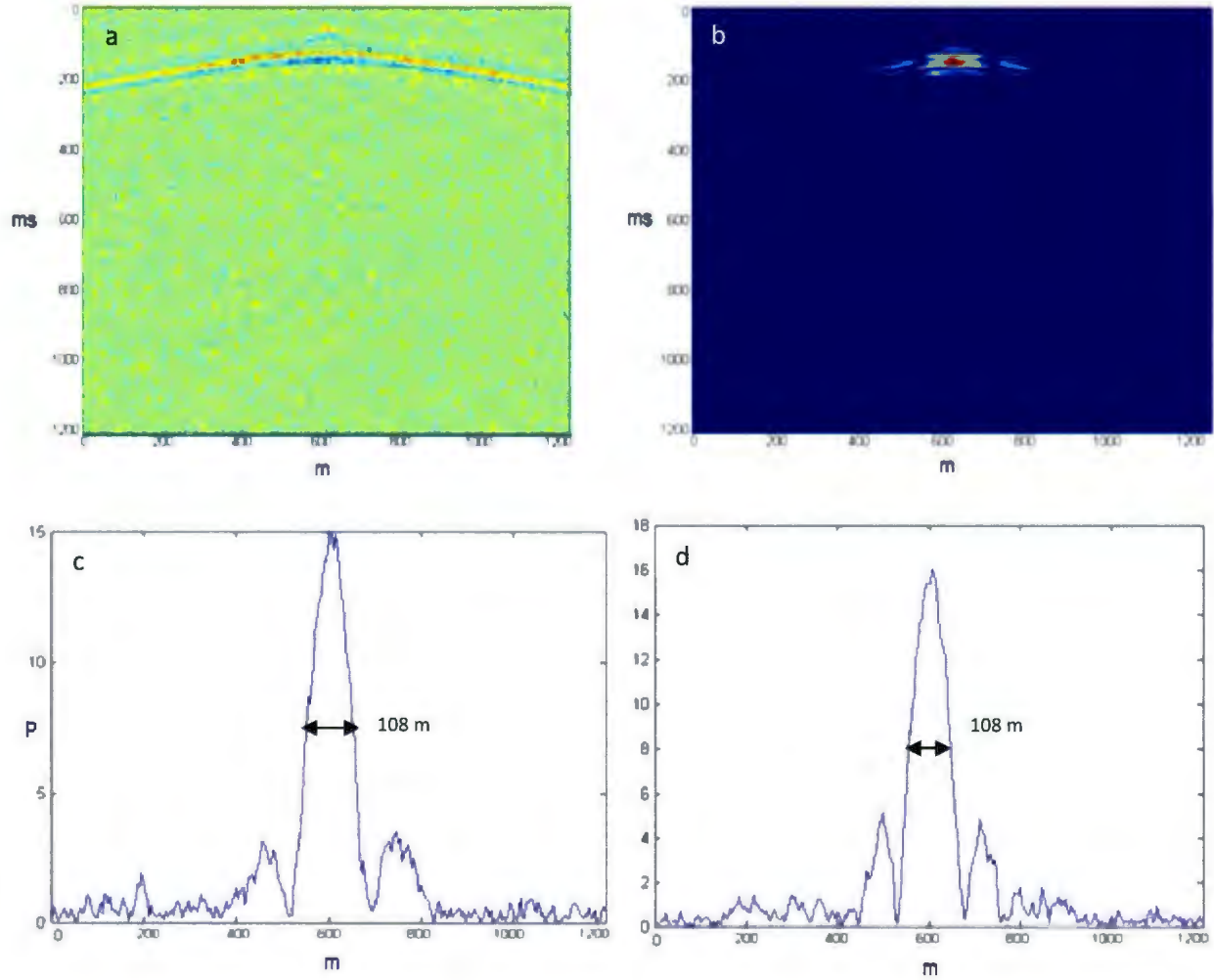


Figure 86: (a) shot gather (b) beam-former image (c) & (d) 1-D representation of beam from top and bottom of target respectively.

The $\frac{1}{2}$ down point of the main-beam for the beam from the top is 108 m and from the bottom is 108 m.

4.3.7.3.4. Test 17

More noise was added to this model. 0.28 is the signal-to-noise ratio here.

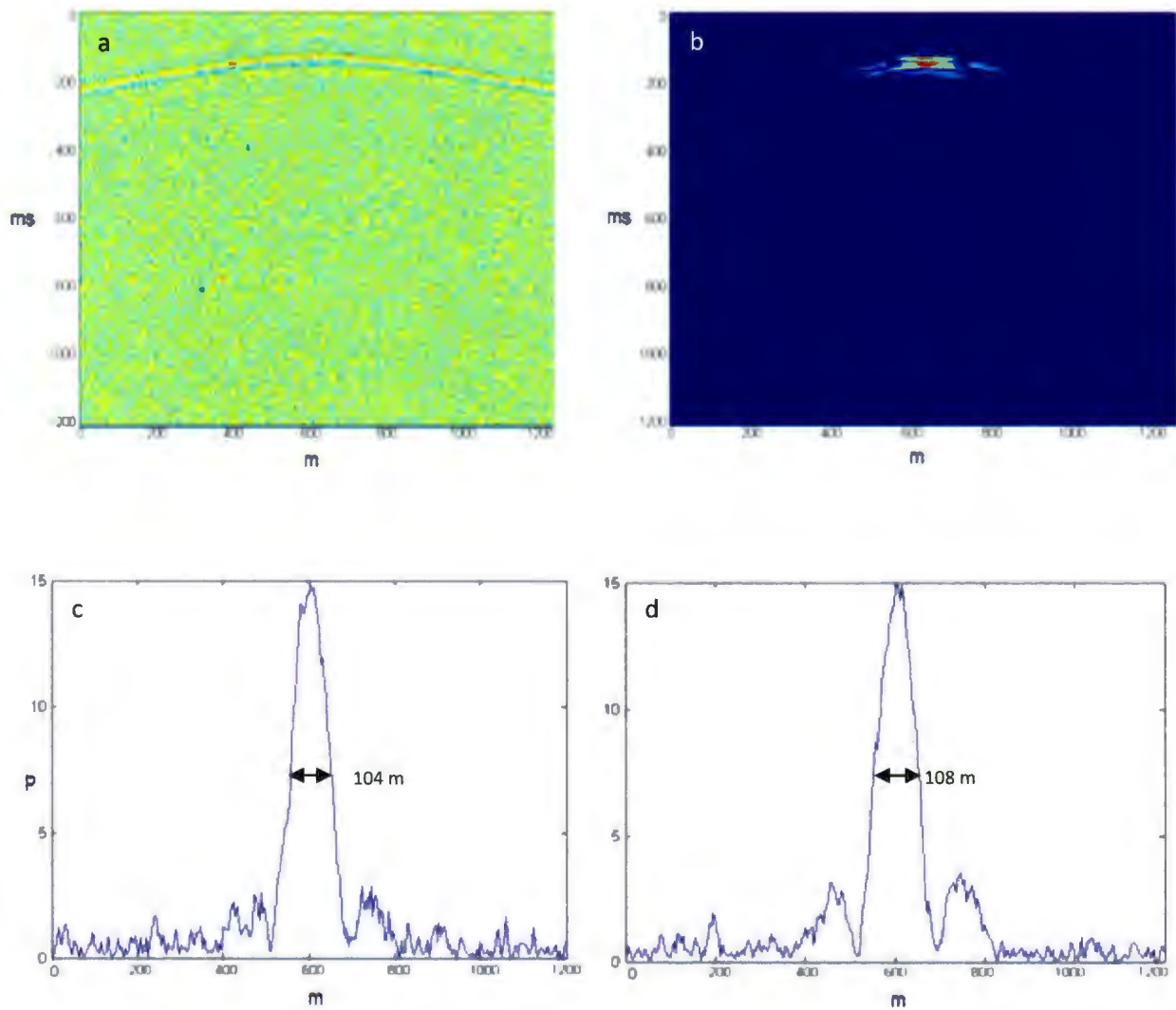


Figure 87: (a) shot gather (b) beam-former image (c) 1-D representation of beam from top of target (d) 1-D representation of beam from top of target.

4.3.7.3.5. Test 18

0.14 is the signal-to noise ratio for the sixth example.

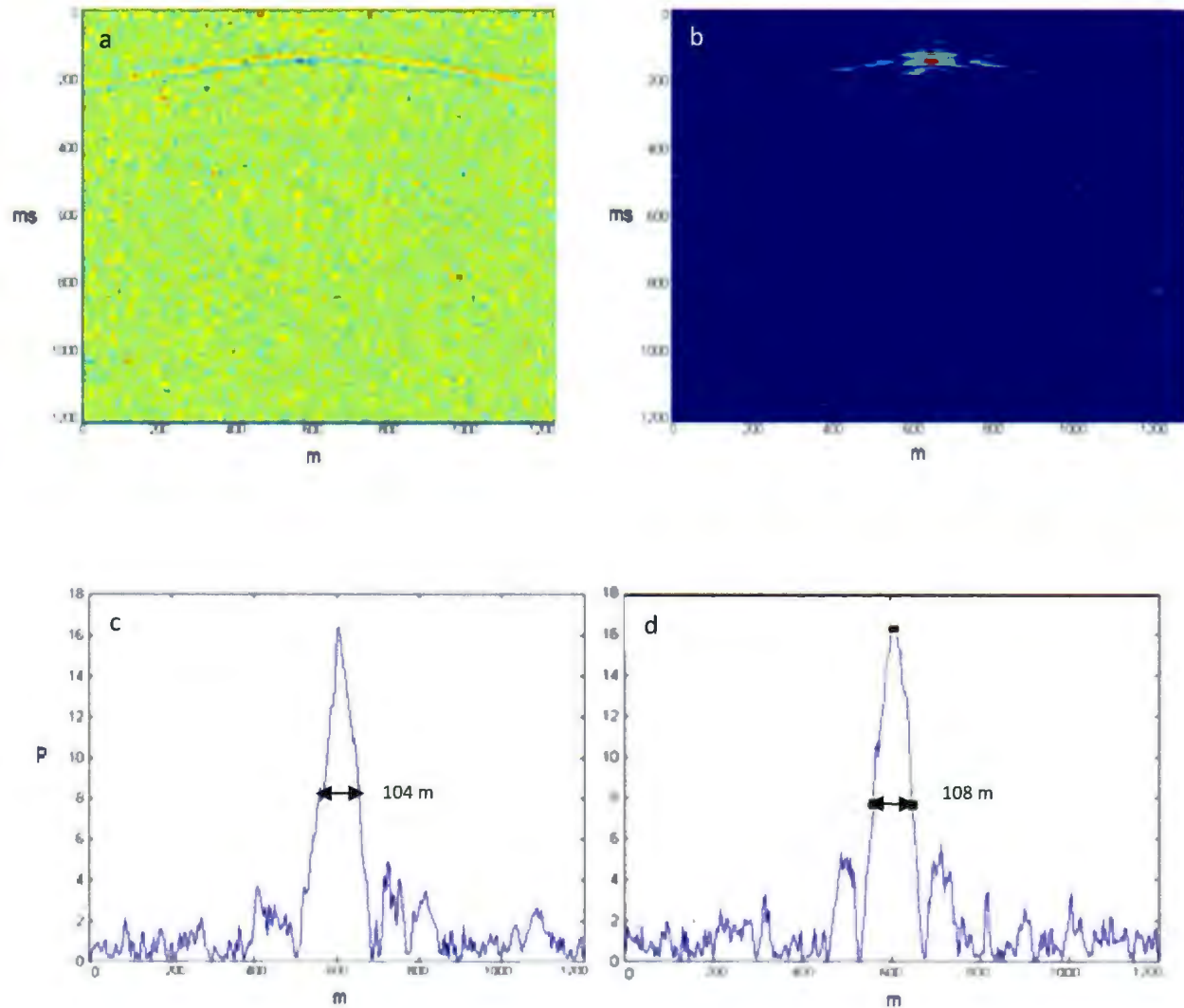


Figure 88: (a) shot gather (b) beam-former image (c) & (d) 1-D representation of beam from top and bottom of target respectively.

4.3.7.3.6. Test 19

In the last example of this section, the signal-to-noise ratio 0.02 was chosen. This ratio is fairly small. Even in Figure 89 (a) it is really hard to find the hyperbola visually, but the beam-former was very effective in locating the target in a highly noisy environment.

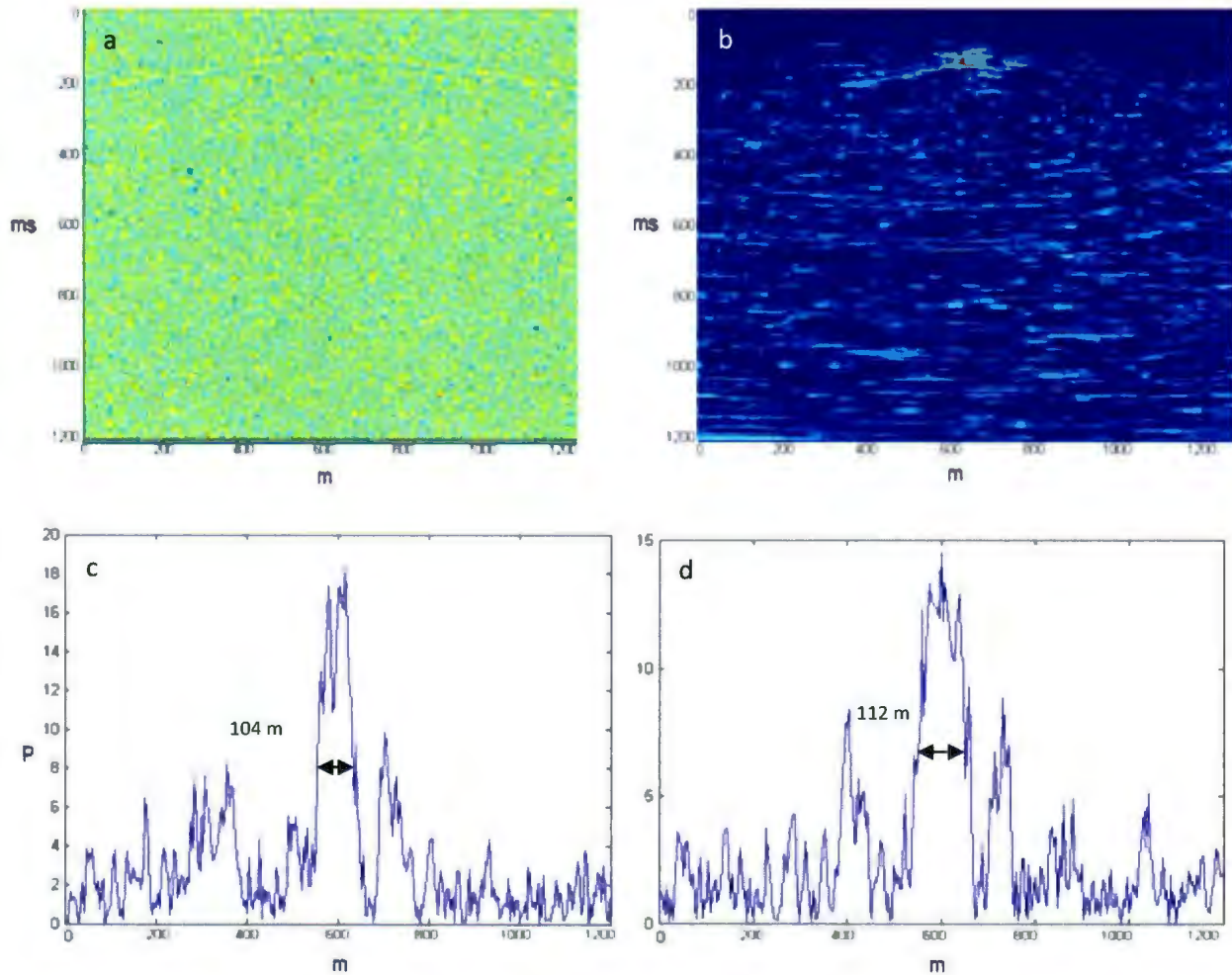


Figure 89: (a) shot gather (b) beam-former image (c) & (d) 1-D representation of beam from top and bottom of target respectively.

More fluctuations appear on both main-beam and side-lobes and is difficult to find the $\frac{1}{2}$ point down the main-beam and peak position. Smearing of noise by the beam-former can be seen in the area beneath the target.

According to the noise analysis, by adding noise:

- The fluctuations on the beam increased.
- Picking the maximum of the peak is going to be more difficult in noisier data.
- Smearing in the data especially in the deeper area could be seen.

4.3.8. Shifts Along Hyperbola

In land-data, the near-surface part of the earth could harshly degrade the quality of seismic data. Because of lateral velocity variations within the near-surface, the data is distorted close to the source and receivers (Hindriks, 2007). Time shifts and amplitude changes are observed if these variations are strong. Therefore, a need to remove these effects exists. Commonly used strategies, such as static correction, help to remove these effects by applying time shifts and amplitude corrections. In real data, the hyperbola would not be as smooth as the synthetic data. To study the accuracy of our method in this situation, both systematic and random shifts through the hyperbola were made.

4.3.8.1. Test 20

In this example, every other ten traces shift one unit along the y-axis. The one unit shift equal to 4 ms is equal to an 18 m shift, which is smaller than a quarter of the wavelength. Figure 90 demonstrates the results of the beam-former under these conditions.

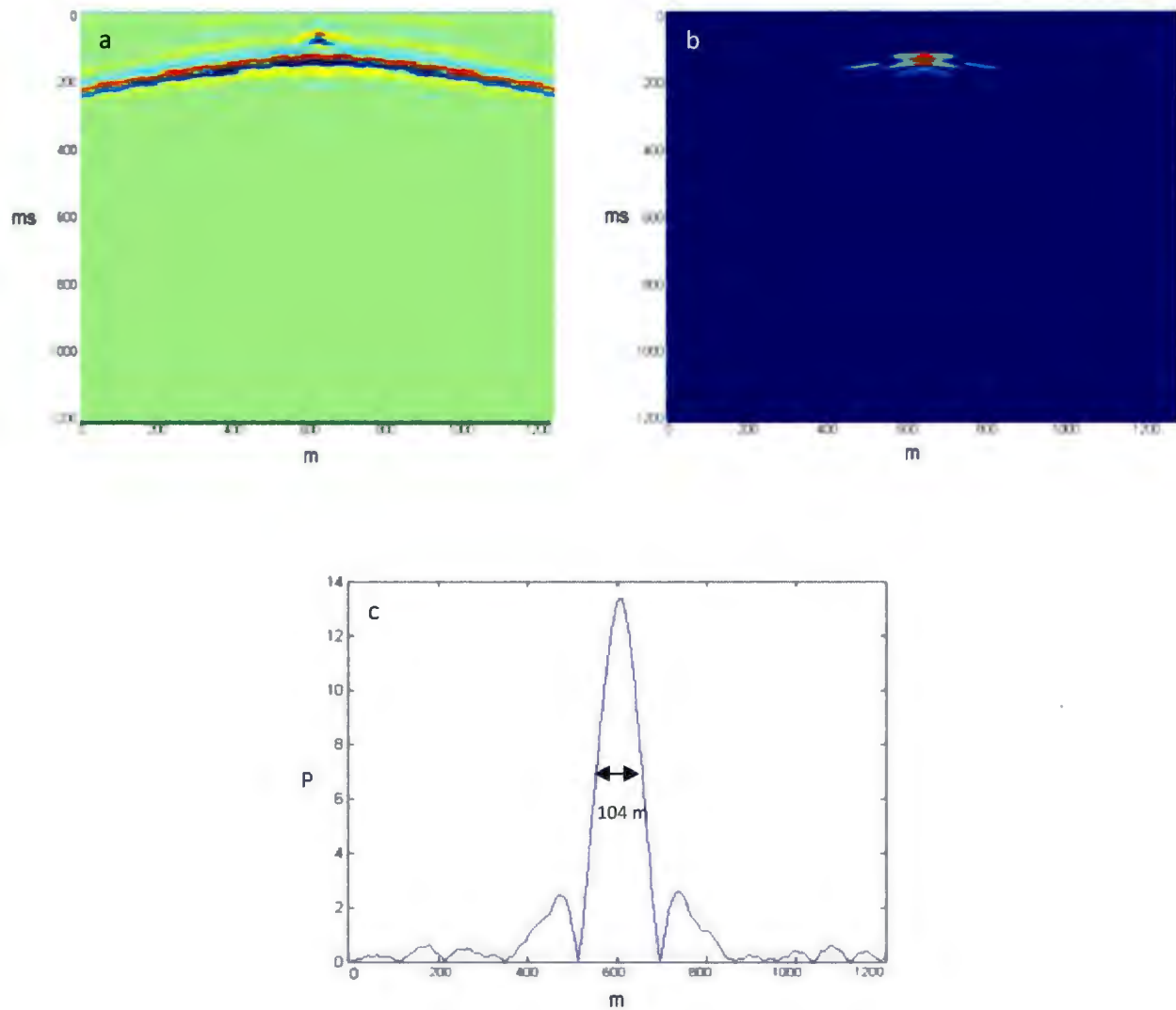


Figure 90: (a) shot gather (b) beam-former image (c) 1-D representation of beam from top of the target.

4.3.8.2. Test 21

In this example, every other ten traces shift two units along the y-axis. The two unit shift equal to 8 ms is equal to a 36m shift, which is bigger than quarter of the wavelength. Then the beam-former is applied to the model to examine how it effects (Figure 91).

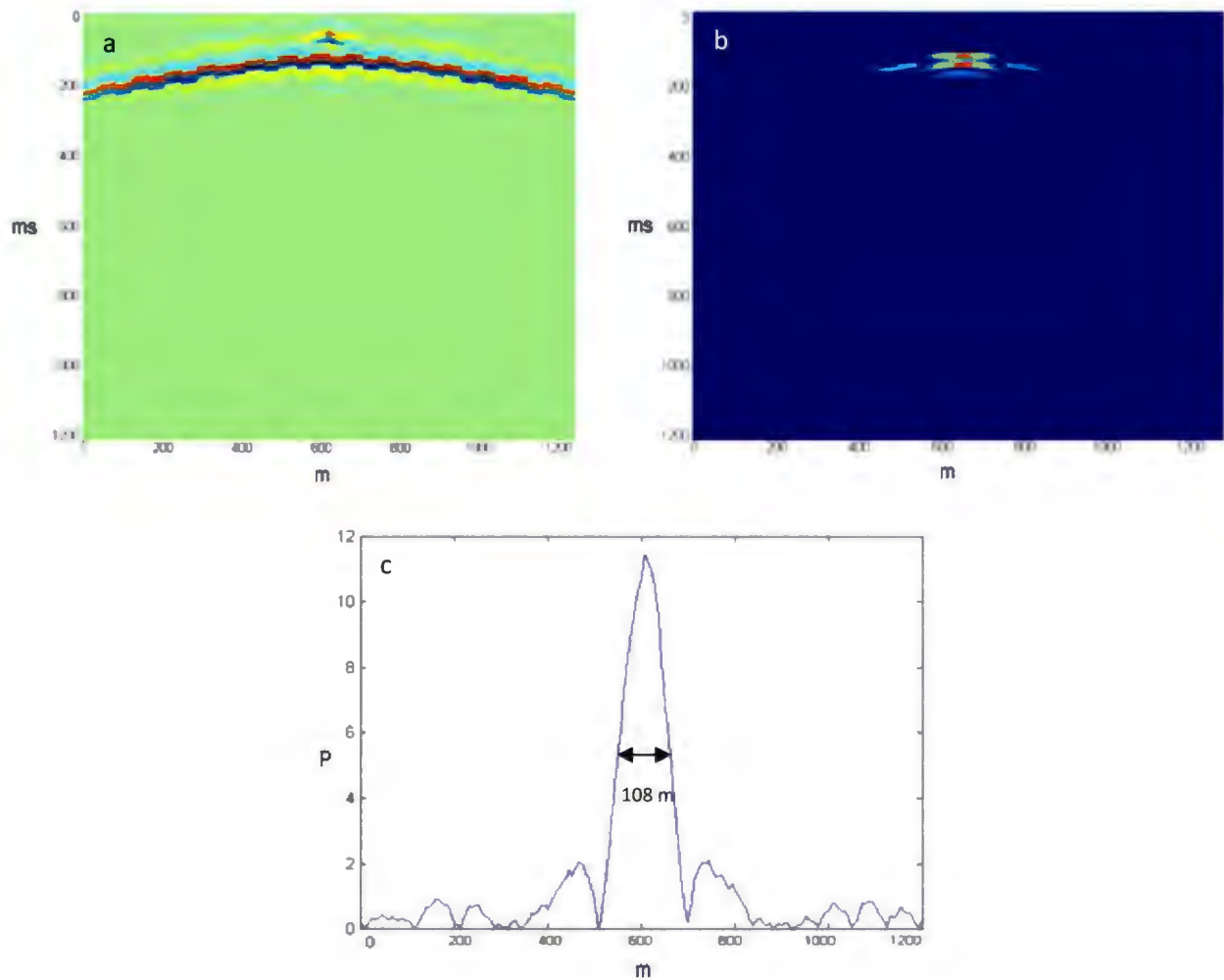


Figure 91 : (a) shot gather (b) beam-former image (c) 1-D representation of beam from top of the target.

4.3.8.3. Test 22

In this example, random shifts (1-4 shifts) have been applied to the traces along the y-axis. The result of the beam-former shows the side-lobes are bigger in comparison with the last example, but it can still locate the target successfully (Figure 92).

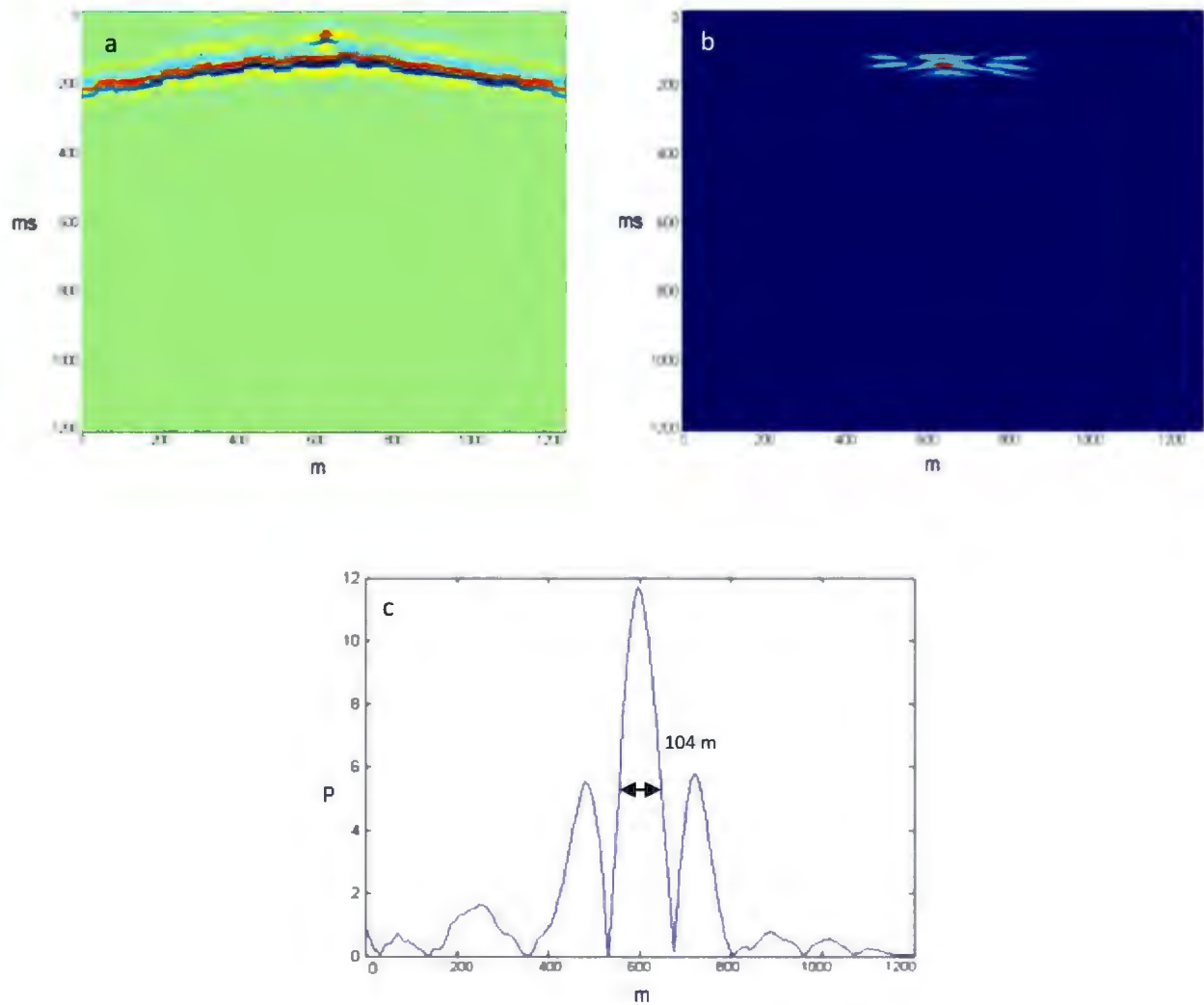


Figure 92: (a) shot gather (b) beam-former image (c) 1-D representation of beam from top of the target.

4.3.8.4. Test 23

In this example the target is offset from the source which is at the centre of the array. The target is a square scatterer with dimensions of 50 by 50 m at the depth of 250 m. Random shifts have been applied to the traces along the y-axis.

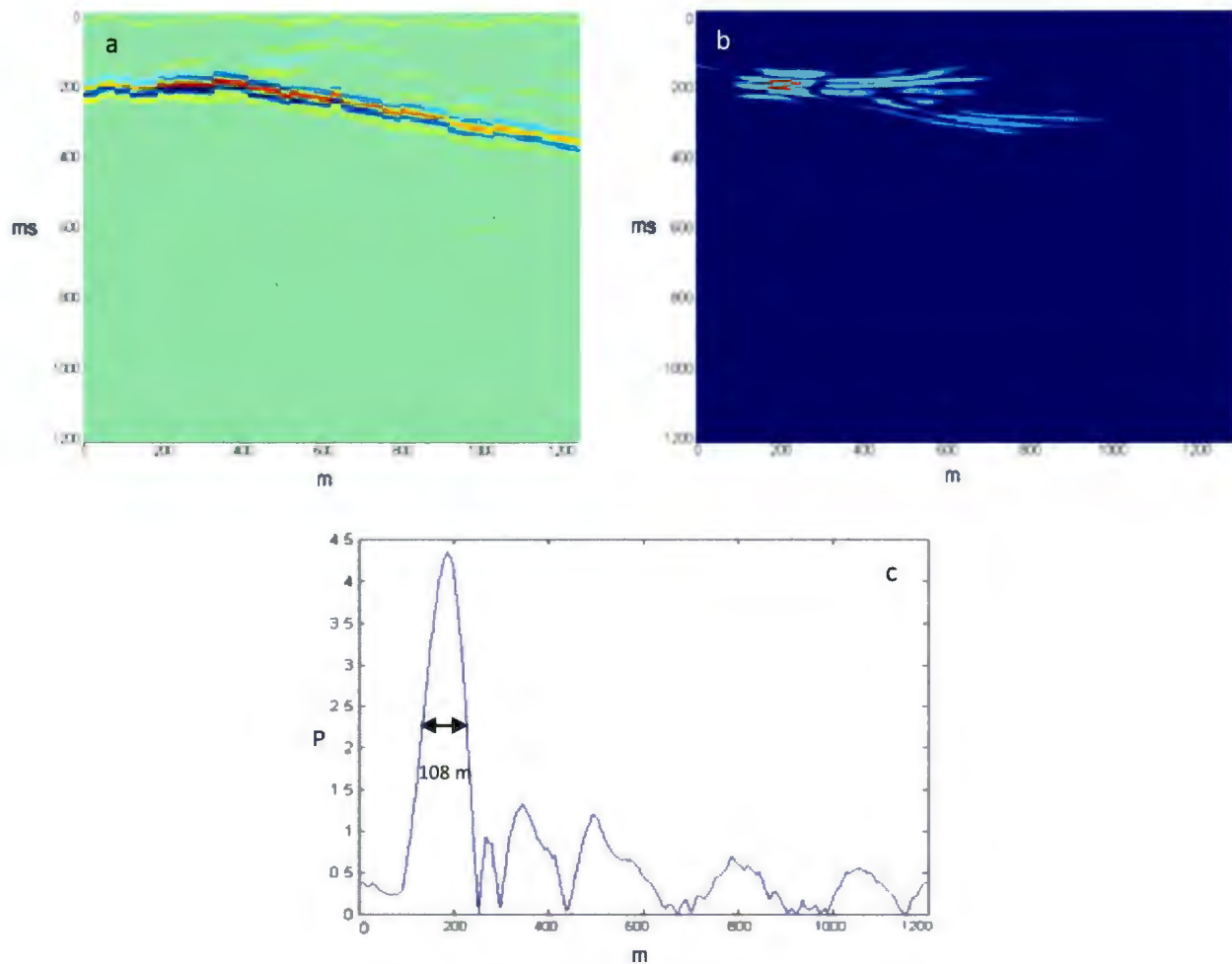


Figure 93: (a) shot gather (b) beam-former image (c) 1-D representation of beam from top of the target.

As can be seen in the beam-former image Figure 93, some parts of the result smear out, and the beam-former produces false events which could be because of the big shifts at the middle of the array.

4.3.9. Test 24: Combination of Shift and Noise

In this section, we combined what has been done in sections 4.3.7 and 4.3.8. This means Gaussian noise is added to the data, and random shifts to the shot-gather are applied to give a more complicated model. The signal-to-noise ratio for this example is 0.28 (the main reason for choosing this S/N is because it is not as noisy as test 18 & 19 and not as clean as tests 14 & 15). Shot-gather and the beam-former result can be seen in Figure 94.

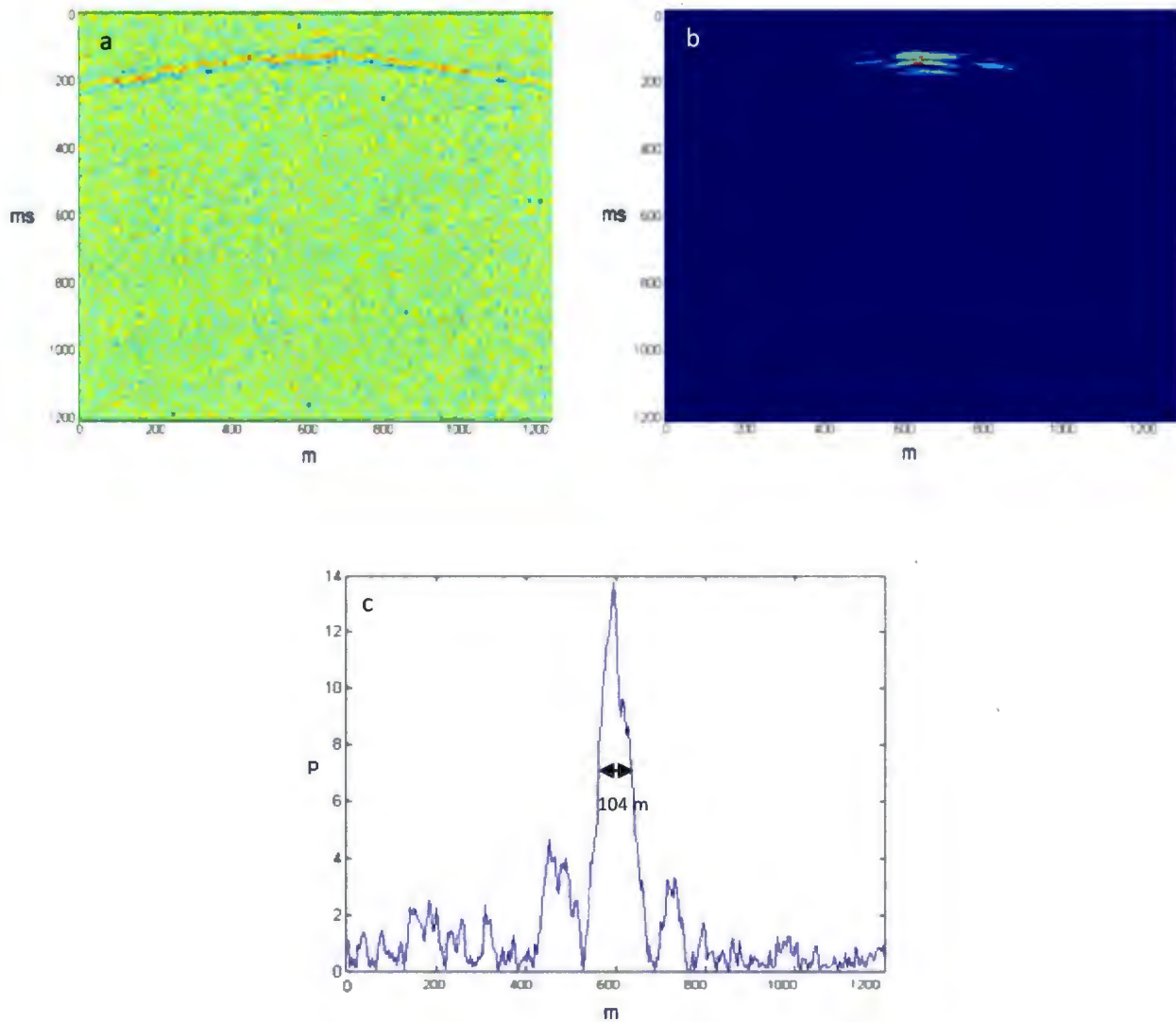


Figure 94: (a) shot gather (Noise added to data) (b) beam-former image (c) 1-D representation of beam from top of the target.

4.3.10. Test 25: When There Are Obstructions Along the Line

In this section, the situation and model is the same as the model in last section; the only difference being there are some random gaps along the array (similar to what has been discussed in section 4.3.6). Situations that occurred in section 4.3.6, 4.3.7 and 4.3.8 have been combined. Gaussian noise added to the data, and random shifts applied to the shot-gather to give more realistic results. The signal-to-noise ratio for this example is 0.28. Shot gather and the beam-former result can be seen in Figure 95.

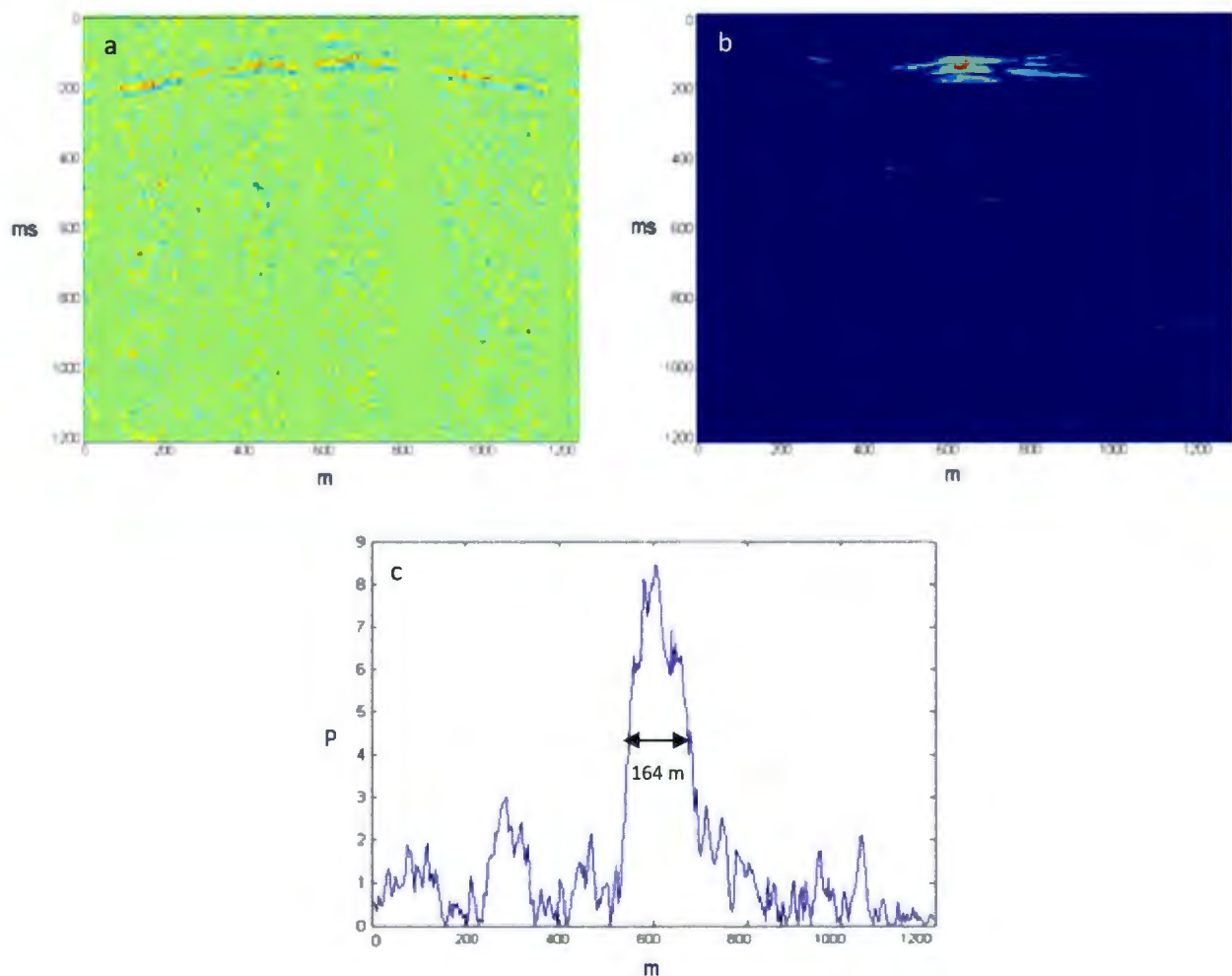


Figure 95: (a) shot gather (Noise added to data) (b) beam-former image (c) 1-D representation of beam from top of the target.

Comparison between Figure 94 and Figure 95 indicates that by having obstructions along the array the beam resolution has changed.

4.3.11. Test 26: Closest Model to Real Situation

The last model in this chapter is the most complicated model that we have considered. There are five scatterers in the model at different depths and offsets. There is no preference to making the model, the goal is to have shallow and deep targets with different shapes and examining all the discussed situations in this chapter in one model.

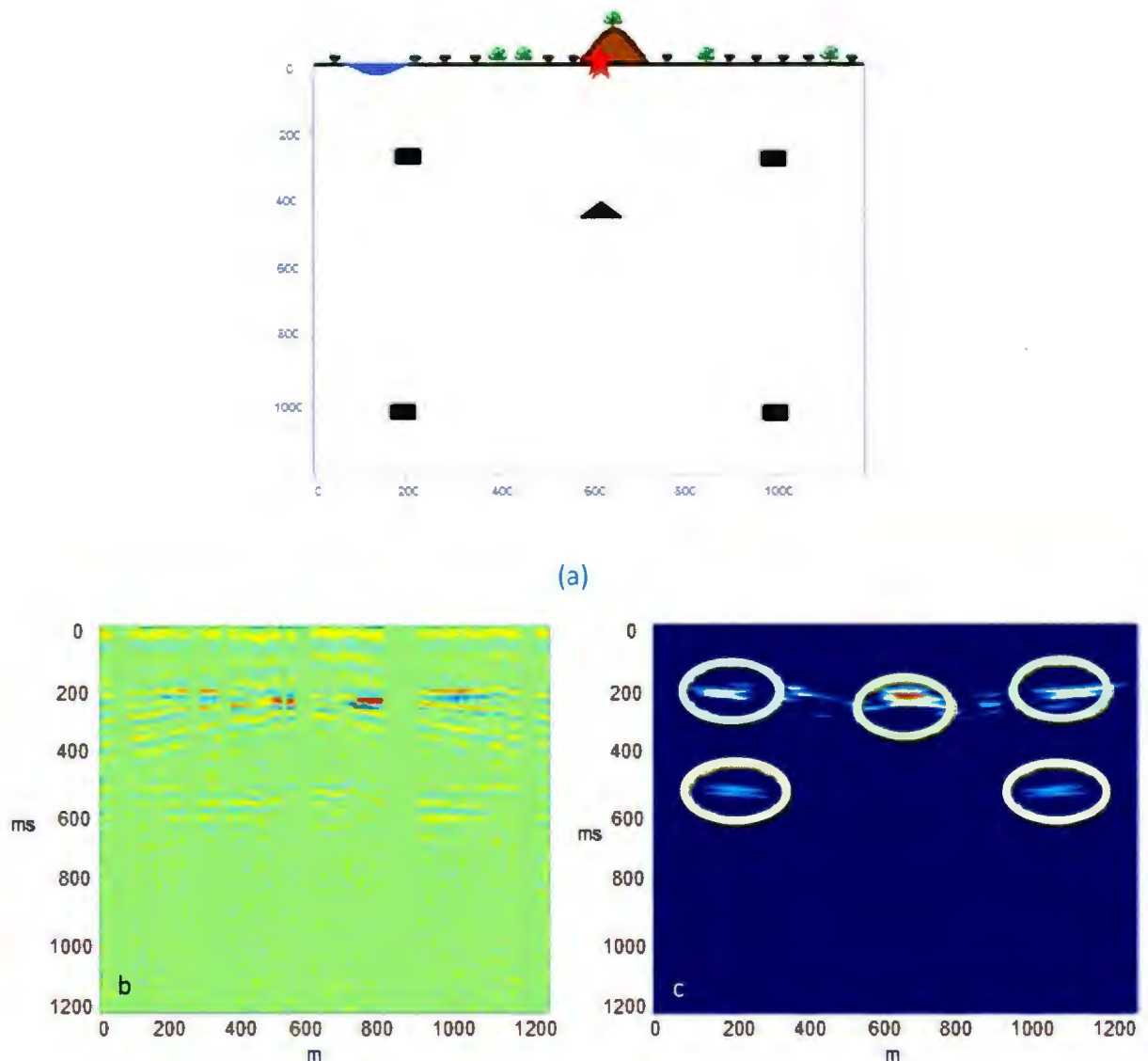


Figure 96: (a) Primary model (b) shot gather after adding noise (c) Beam-forming image. Five targets could be detected in this figure.

4.4 Experimental Results on Vertical Seismic Profiling Data

Vertical Seismic Profiling (VSP) is the link between geology and geophysics (Hinds and Kuzmiski, 2001). VSP is a specific type of borehole seismic recording where receivers (geophones or hydrophones) are lowered down a well, and seismic sources are located on the surface at different offsets (depending on what kind of VSP survey is used). The VSP and surface seismic data invariably match in character, due to the common source and receiver type used in both surveys. In addition, a VSP survey will record energy reflected and diffracted from steeply-dipping faces that would not ordinarily return to the surface. VSP data commonly have better resolution than surface data because of the smaller Fresnel zone and larger bandwidth, and the seismic energy travels through the distorting overburden only once (Payne et al., 1994). The combination of surface reflection profiles and VSPs provide the best spectral coverage (Wu and Toksoz, 1987). In Figure 98, the VSP data is shown. Furthermore, a zero-offset VSP geometry was used for this study.

4.4.1 Test 27: Beam-former Performance on VSP Data

In this example, the target is the 50 by 50 m square target. The target is at the depth of 375 m and the shot position is shown by the red star in Figure 97.

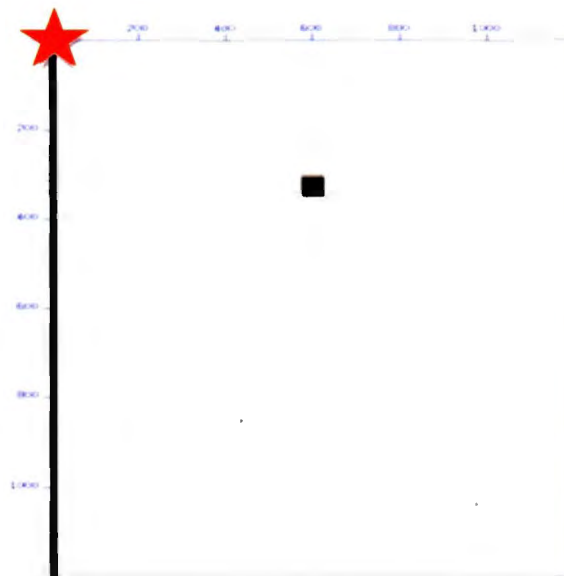


Figure 97: In this example target's dimension is 50 by 50 m. The black line represents borehole. The receiver spacing is 4 m.

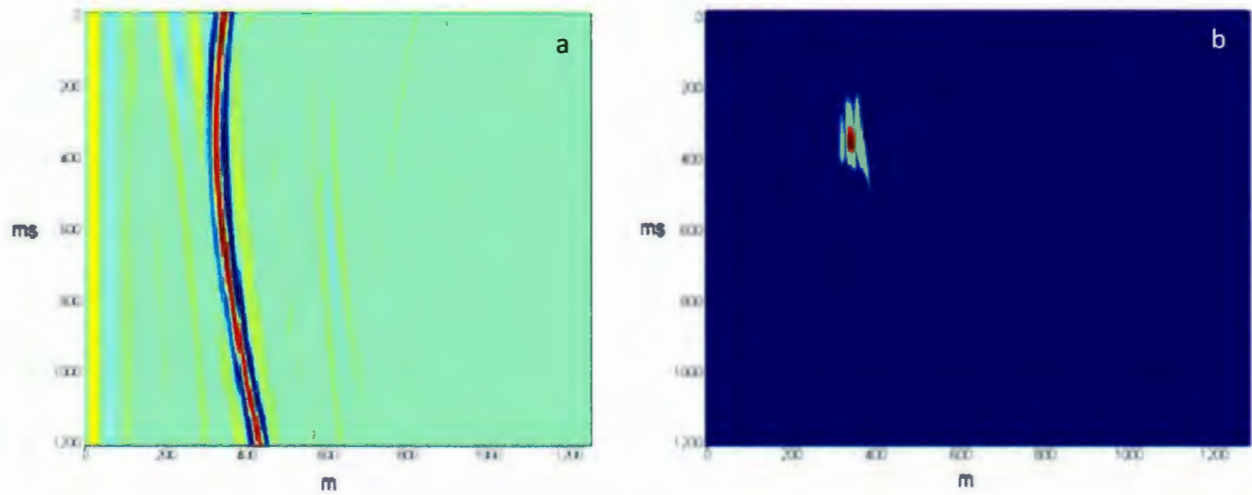


Figure 98 (a) Shot gather (b) This figure is the result of beam-forming on the VSP data. The high power can be seen on left and right of the target. To find the location of the target, it is better to look at the two dimensional spectrum on left and right of the target.

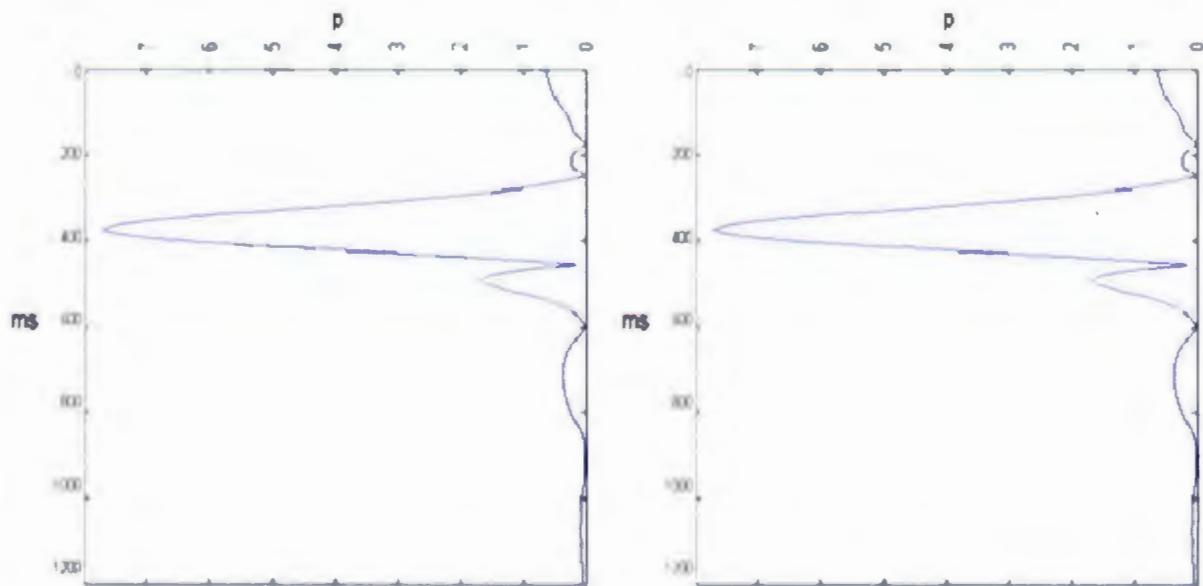


Figure 99: The ratios of main-lobe to side-lobes are fairly acceptable and there is no problem to find the maximum position of the main-lobe.

As we discussed earlier, by applying the beam-former on the surface profiling, we could locate the target horizontally. For detecting the target vertically, applying the beam-former on VSP data would help. Therefore, combination of these solves the localization issues.

4.5 Field Data Example

The experiments using synthetic data provide a characterization of the beam-former performance under various conditions. The real test of the beam-former is on real seismic data. If this technique works for real field data, it provides validation as a useful tool. In most techniques there is often a disparity between the synthetic models and real field data. One of the most important reasons for the real data test is the existence of both coherent and incoherent events and noise in this data. The method is applied on both shot-gather data and stacked section.

4.5.1 Velocity Analysis

Before applying the method on the real data, it is required to mention one issue. Velocity information is required for the beam-former. There are two options for defining and importing the velocity profile to the beam-former:

- Using other tools such as Semblance Velocity or Constant Velocity Analysis for defining the velocity profile
- Or
- Running the beam-former for a range of constant velocities

In this thesis, we choose the second option because other methods like Semblance Velocity Analysis are based on the specular reflection while our goal is scatterer detections. A range of velocities is chosen based on the media we are performing the beam-former. This process can be considered as a velocity analysis tool. After iterating over a range of velocity values for each subsurface point, we retain the velocity that produced the highest beam power.

4.5.2 Test 28: Shot Gather from VSP Data

The data used in this section is a VSP survey from Voisey's Bay. The receiver spacing is 2 m and time sampling is 2 ms. The VSP is shown in Figure 100. By looking at the data, even though the signal-to-noise ratio is low, it is expected to detect the targets in 2 areas.

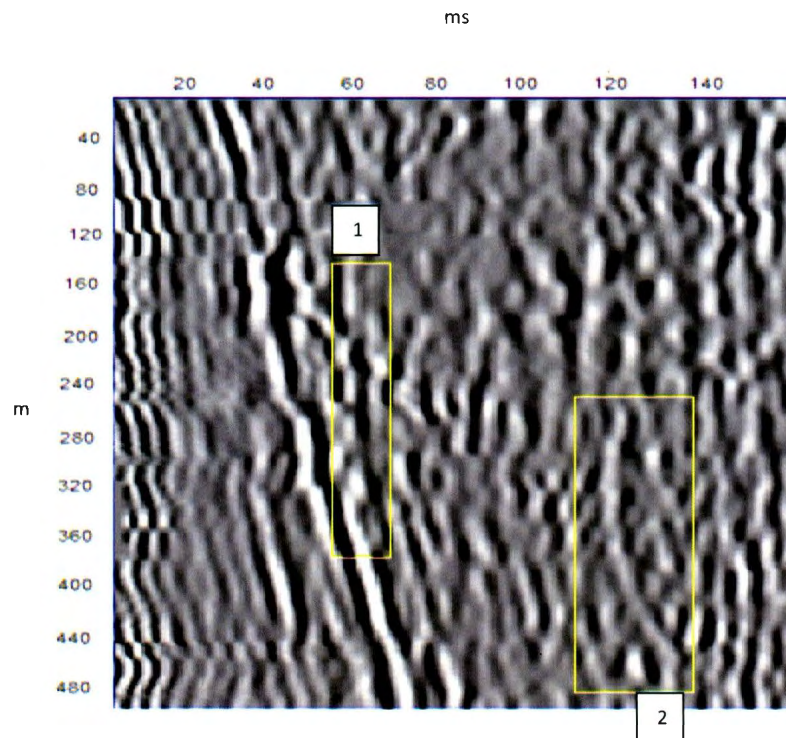


Figure 100: VSP Shot gather

Because the beam-former requires velocity information, in order to detect the targets fine velocity searches from 1000 m/s to 4500 m/s (with 100 m/s intervals) are applied. We can choose the velocity for specific target based on the velocity at which the beam-forming produces highest power. In Figure 101, the results of beam-former for velocities of 2000, 3100, 3400 and 4400 m/s are shown.

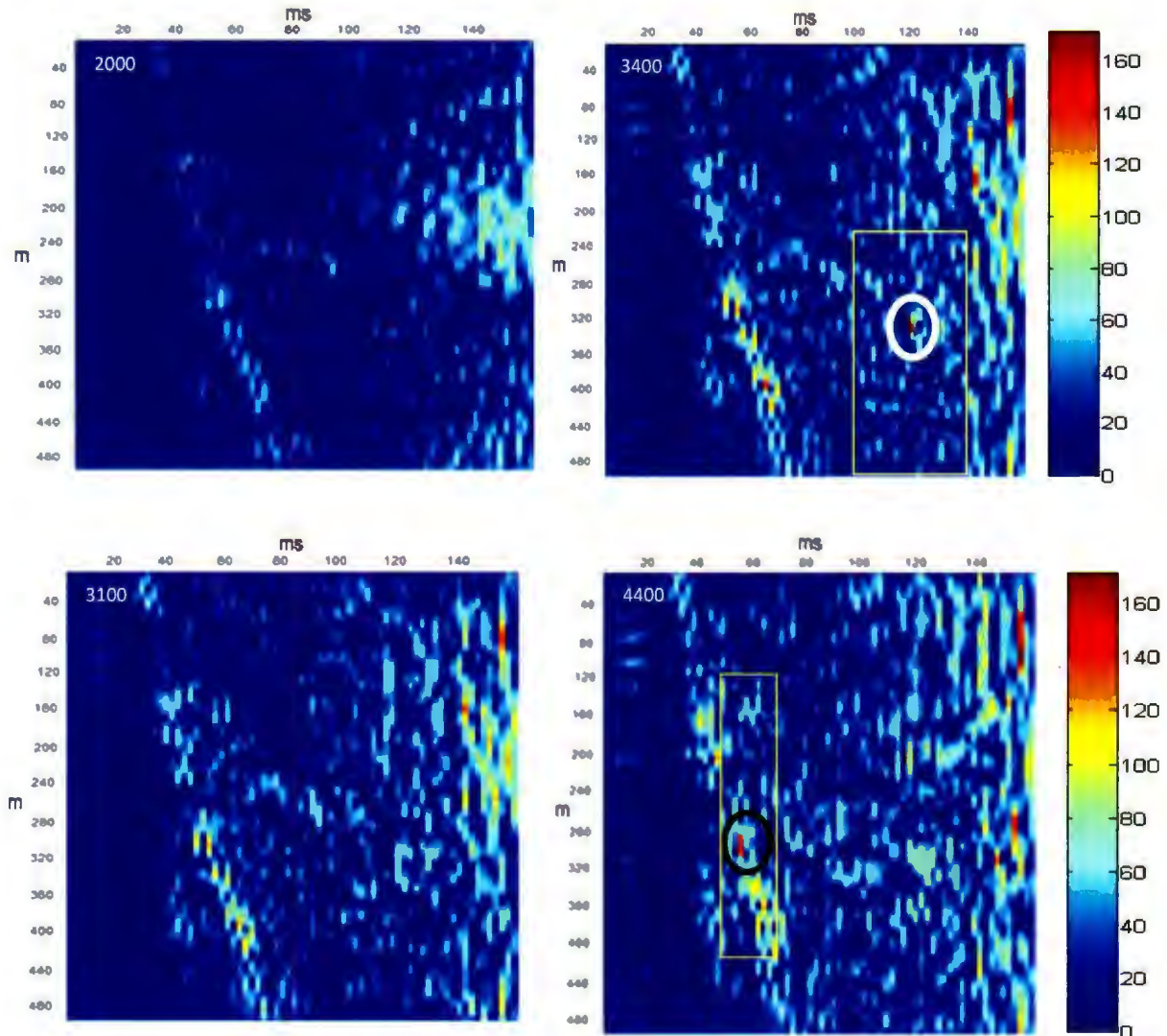


Figure 101: In this set of Figures, the results of beam-former on the VSP data with the velocities of 2000, 3100, 3400, and 4400 m/s are shown

As can be seen, for low velocity (2000 m/s), there is no high amplitude. By increasing the velocity, the events in shallow parts starting to show up. In area 1, as can be seen in Figure 101, the high power show up at the velocity of 4400 m/s, which make sense because if you look at the original data it is flat and it is expected to show up at the higher velocities. The diffraction in the area 2 has the highest power at the velocity of 3400 m/s.

4.5.3 Test 29: Stacked Data Example

The data used in this section is CMP-stacked section over a massive sulphide deposit at Voisy's Bay, Labrador. Shot spacing is 20 m, receiver spacing is 10 m, and CMP spacing is 5 m. The stacked section can be seen in Figure 102. These data provide a controlled test of the beam-former because we are able to identify a low signal-to-noise ratio diffraction event which should be detectable.

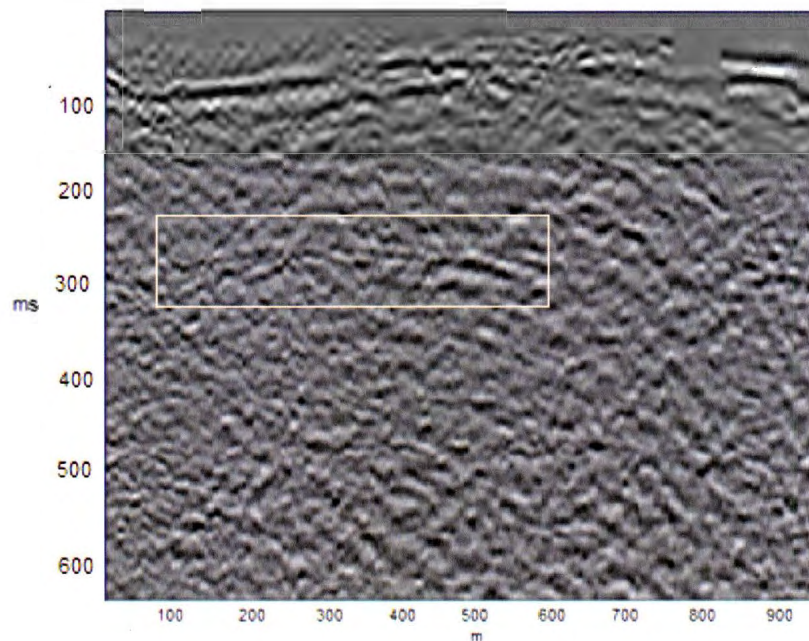


Figure 102: stacked section. The diffraction hyperbola can barely be seen as indicated.

In this example, our method is examined for detecting the known target of very low signal-to-noise. In order to detect the target and saving time, a coarse velocity search followed by a fine velocity search is applied to identify the correct velocity. For the coarse search the beam-former was run using a range of different velocities, 1000 m/s, 1500m/s, 2000 m/s, 3000 m/s, 4000 m/s and 5000 m/s.

In the section which beam-formed by the velocity of 1000 m/s, there is no anomaly with high power. By 1500 m/s, some anomalies started to show up which could be real but in this section we are looking to detect the specified diffraction in Figure 102. For the velocity of 2000 and 3000 m/s, the high powers started to show up at the area we expected to find the diffraction.

While in the 4000 m/s model the diffraction is completely distinguishable and shown up as a single high power event. Therefore, we could say the 4000 m/s could be a velocity for beam-former to detect the target better. Keep in mind the velocity is not the value we are looking for. We just want to detect the target. In following Figures, all results scaled the same and the color bar is provided as well.

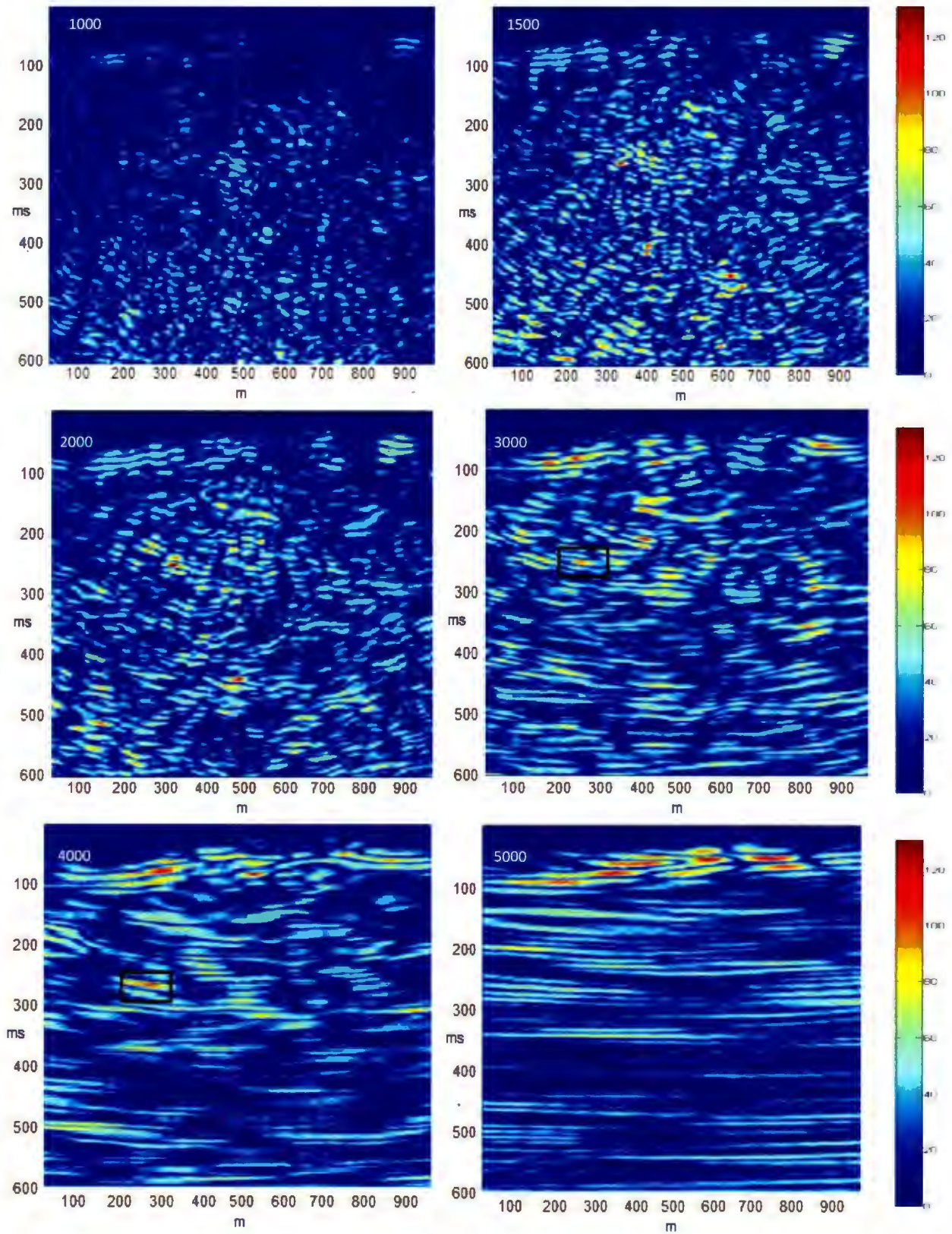


Figure 103: The code was run for various velocities: 1000, 1500, 2000, 3000, 4000 and 5000 m/s.

Based on the results shown in Figure 103, we meet our expectations for detecting the known target by our method in noisy data. There are also other high power potential targets which have high power and they could be true or false target. The main goal in this test is testing our method on real data when the signal to noise ratio is fairly low.

Out of curiosity, to see how sensitive the beamformer is for detecting the target and to examine whether we can trust this method in a blind experiment, the code was run for a fine velocity range. 3700, 3900, 4100 and 4300 m/s are the chosen velocities. The results show that in all five beam-former sections the high power event appeared in a hypothetical square area limited to 200 and 300 ms in vertical direction and 200 and 300 m in lateral direction.

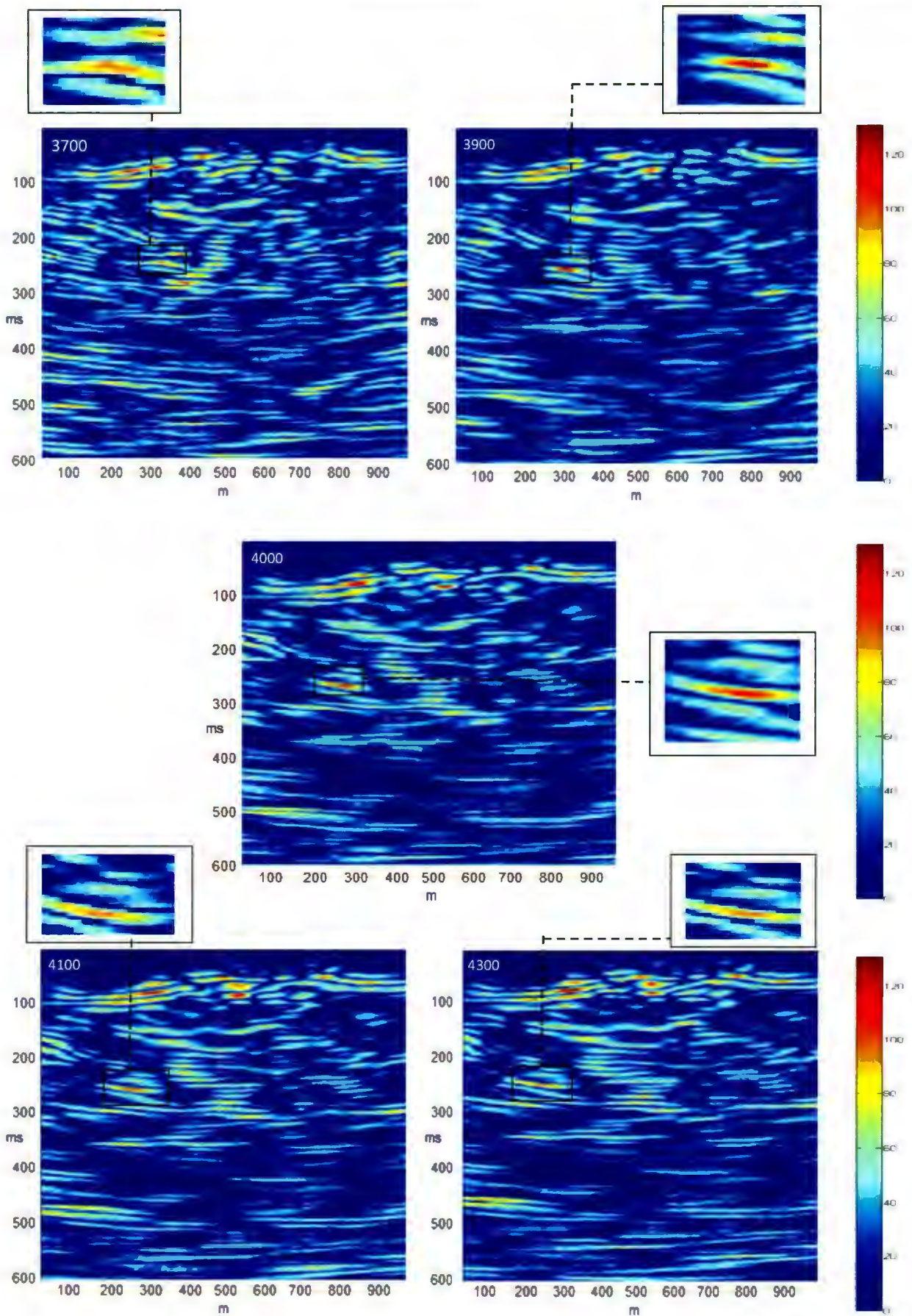


Figure 104: Fine search for finding the best velocity for detecting the target.

The beam-former result for the velocity of 3900 m/s (it gives us the most distinguishable event in comparison with 3700, 4000, 4100 and 4300 m/s) was chosen to compare with the seismic section.

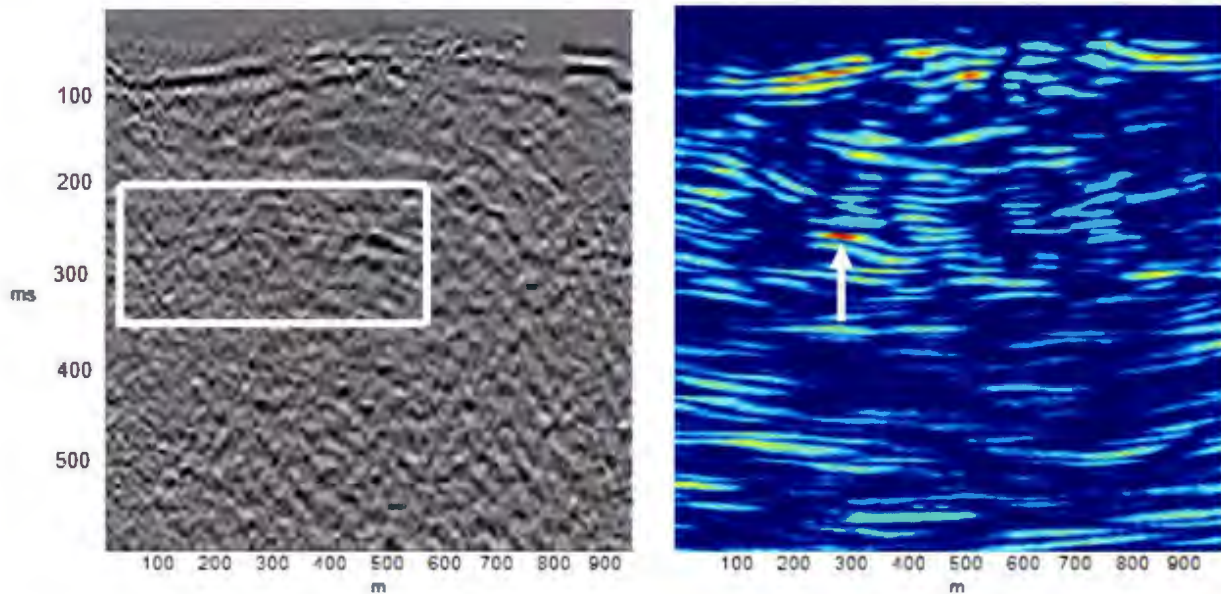


Figure 105: stack data and beam-forming result.

The results indicate that the beam-former is effective for detecting the target under relatively low signal-to-noise conditions. There are some smearing in the deeper part of the data which is the result of both coherent and in-coherent noises which have already seen in the synthetic data in noise analysis section. They could also be a target which has a lower power or even a false target that detected by the beam-former.

The 1-D representation of beam of the target is also shown in Figure 106. Fluctuations on the beam, like those seen in synthetic data, are present, but a clear peak in power is present.

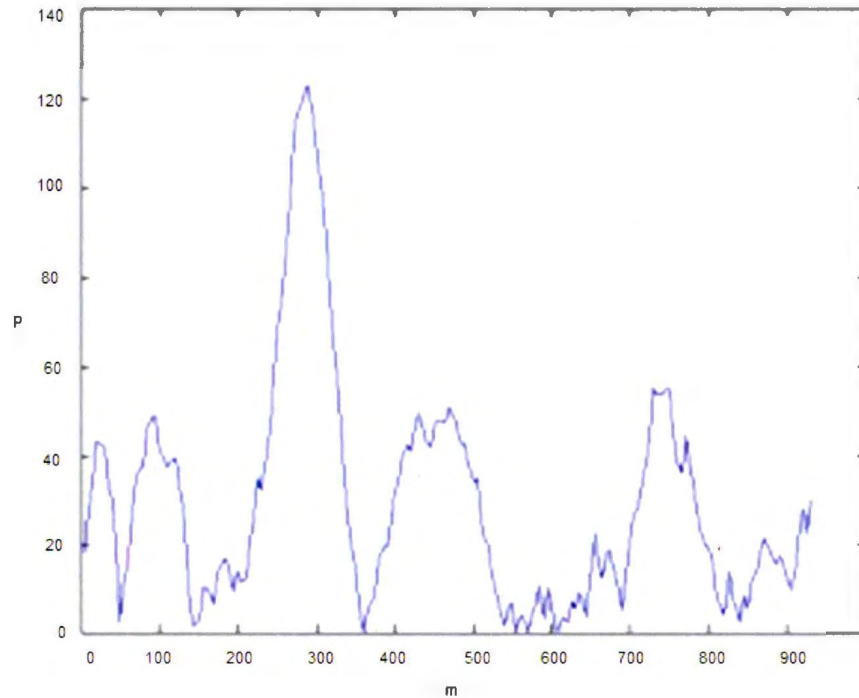


Figure 106: 1-D representation of beam from top of the target.

4.6 Summary

In this Chapter, I present an evaluation of the performance of the conventional beam-former on both 2-D synthetic seismic data and field data. We discussed the capability of the beam-former on targets at the center and offset from the source in various depths. The beam-former was also tested on targets with different shapes and sizes. The beam-former's ability to locate two scatterers vertically and horizontally was assessed in section 4.3.5. Section 4.3.7 shows that in a noisy environment, the beam-former does a good job. The signal-to-noise ratio was calculated using a method explained in section 4.3.7.2. In the rest of this chapter, the synthetic models are changed to be more similar to real data. Then, the beam-forming algorithm is applied over these models. The results indicate that the beam-former is able to detect the targets even in the worst situations. At the end, the real data are also tested and we observed that the beam-former could detect the multiple targets in VSP data and also detect the known target in a seismic survey. The main point extracted from all the tests is that based on the beam we can locate the target, and predict its size properly in the cases the target is larger than F_z .

Chapter 5

Conclusion and Recommendation

5.1. Conclusion

This document describes the potential of using beam-forming to locate mineral deposits cost effectively. The use of beam-forming for locating the scatterers could significantly reduce exploration costs.

This method has following strengths and weaknesses:

- Beam-former works decently to detect various targets at different
 - Depths
 - Offset from the source
 - Noise levels and recording situations.
- In contrast with Moffat's algorithm (Moffat, 2002) which was unable to pick two scatterers in its vicinity when the source was at a point directly between them, our code works really well in all situations independent of the source position.
- Another advantage of this code in comparison with Moffat's method is that it locates scatterers without any primary information about the scatterers location.
- Testing the technique on real field data is demonstrates its effectiveness on real data that include coherent noise.
- Velocity resolution is one of the weaknesses that the presented beam-former has.
- The lack of depth detection is another prominent weakness of this method when the target is unknown and we are applying the method on shot-gather data.

5.2. Recommendation for Future Research

The main recommendation is to expand the MATLAB code for 3-D data. In this case, the search would be placed on a 3-D cubic data to find the three-dimensional object which causes scattering. In order to accomplish this, an understanding of the 3-D plane wave and spherical wave is required.

In this study the target is mostly defined singly as a region with a velocity of 6500 m/s and the background velocity of 4500 m/s. Including the velocity contrast between the target and the background as an additional parameter could be an area for future work.

This method has a potential to be used in the field. To do this we could rewrite the code in Fortran which could be faster than MATLAB for handling much bigger volume of data. It helps us to detect anomalies during the acquisition process; therefore, after detection, there exists the possibility to change the acquisition design, i.e. attempting to record more data in the specific location, or change the receiver spacing or even record 3-D in that position. As a result, we don't need to 3-D survey the entire area and the project could be less expensive.

Bibliography

- Allred, D.J., 2006, Evaluation and Comparison of Beamforming Algorithms for Microphone Array Speech Processing [M.Sc. thesis]: School of Electrical and Computer Engineering, Georgia Institute of Technology.
- Dudgeon, D.E., and Mersereau, R.M., 1984, Multidimensional Digital Signal Processing: Prentice-Hall Signal Processing Series, 400 p.
- Eaton, D.W., Milkereit, B., and Salisbury, M., June 2003, Seismic Methods for Deep Mineral Exploration: Mature technologies adapted to new targets: The Leading Edge, p. 580-585.
- Hindriks, H., 2007, Estimation and Removal of Complex Near-Surface Effects in Seismic Measurements [Ph.D. thesis]: Technical University of Delft.
- Hinds, R.C., and Kuzmiski, R., 2001, VSP for the Interpreter/Processor for 2001 and Beyond: Part 1: CSEG Recorder v. 26 p. 84-95.
- Hurich, C.A., 1996, Statistical Description of Seismic Reflection Wavefields: A step towards quantitative interpretation of deep seismic reflection profiles: Geophysics, v. 125, p. 719-728.
- Iyer, H.M., 1968, Determination of Frequency-Wave-Number Spectra Using Seismic Arrays: Geophysical Journal of the Royal Astronomical Society, v. 16, issue. 2, p. 97-117.
- Jeng, Y., Li, Y., Chen, C., and Chien, H., 2009, Adaptive Filtering of Random Noise in Near-surface Seismic and Ground-penetrating Radar Data: Journal of Applied Geophysics, p. 36-46.
- Johnson, D.H., and Dudgeon, D.E., 1993, Array Signal Processing: Prentice Hall, 512 p.
- Juhlin, C., 1990, Interpretation of the Reflection in the Siljan Ring Area Based on Results from the Gravberg-1 borehole: Tectonophysics, v. 173, p. 345-360.
- Kelly, K.R., Ward, R.W., Treitel, S., and Alford, R.M., 1976, Synthetic Seismograms: A Finite Difference Approach: Geophysics v. 46, no. 1, p. 2-27.
- Kerekes, A.K., 2001, Seismic Array Design by Spatial Convolution: Geophysics v. 66, no. 4, p. 1195-1207.
- Lanslots, J., Deblauwe, F., and Janssens, K., 2010, Selecting Sound Source Localization Techniques for Industrial Applications: Sound and Vibration p. 1-9.

- Lundstrom, T., 2008, Matched Field Beamforming Applied to Sonar Data [M.Sc. thesis]: Department of Electrical Engineering, Linkopings Universitet.
- Malehmir, A., and Bellefleur, G., 2011, Reflection Seismic Studies of Mineral Deposites and Their Host-rock Structures: two case studies from Sweden and Canada: Geophysical Research Abstract EGU 2011-71-1, v. 13, p.1.
- Manolakis, D.G., Ingle, V.K., and Kogon, S. M., 2000, Statistical and Adaptive Signal Processing: Spectral estimation, signal modeling, adaptive filtering and array processing: The McGraw-Hill Science/Engineering/Math, 816 p.
- Milkereit, B., Eaton, D., and Salisbury, M., 2003, Hardrock Seismic Exploration: Society of Exploration Geophysics, 276 p.
- Moffat, L., 2002, Location of Sub-Fresnel Scale Mineral Targets In The Subsurface [M.Sc. thesis]: Memorial University of Newfoundland.
- Payne, M.A., Eriksen, E., and Rape, T.D., 1994, Considerations for high-resolution VSP imaging: The Leading Edge, v. 13, issue. 3, p. 173-180.
- Salisbury, M.H., and Snyder, D., 2007, Application of seismic methods to mineral exploration, in W. D. Goodfellow, ed., Mineral deposits of Canada: A synthesis of major deposit types, district metallogeny, the evolution of geological provinces, and exploration methods: Geological Association of Canada, Mineral Deposits Division, Special Publication 5, p. 971-982.
- Sheriff, R.E., and Geldart, L.P., 1995, Exploration Seismology: Cambridge University Press, 590 p.
- Tu, Y., 2009, Wavenumber-Frequency Spectrum Estimation of Ambient Seismic Noise [M.Sc. thesis]: Delft University of Technology.
- Van Trees, H. L., 2002, Optimum Array Processing: Part IV of Detection, Estimation and Modulation Theory: John Wiley & Sons, 1472 p.
- Wu, R., and Toksoz, M.N., 1987, Diffraction Tomography and Multisource Holography: Geophysics v. 52, issue. 1, p. 11.

Appendix A

A1: The following code was used to generate *Figure 4*.

Array1D.m

```
% Program to calculate 1-D array response through FFT

Clear all
num=5; % Number of geophones
gspace=5; % Geophone spacing
fnum=64; % number of values in the FFT

period=1/gspace;
kn=1/(2*gspace);

ksamp=period/fnum;

A=[1,1,1,1,1,1,1,1,1,1];
C=A;
t = 1:1:num;

figure(1)
plot(t,C,'y')
hold on

Y = fft(C,fnum);
Pyy = Y.* conj(Y)/ fnum ;
Pyymax=max(Pyy);
NormPyy=Pyy ./Pyymax;

f=(0:ksamp:2*kn);

figure(2)
plot(f(1:(fnum/2)+1),NormPyy(1:(fnum/2)+1),'b')

hold on
```



```

1 0 0 0 0 1 0 0 0 1 0 0 1 0 0 0 0 0 1 0 0 1 0 0 0 1 0 0 0 0 1
1 0 0 0 0 1 0 0 0 1 0 0 1 1 1 1 1 1 1 0 0 1 0 0 0 1 0 0 0 0 1
1 0 0 0 0 1 0 0 0 1 0 0 0 0 0 0 0 0 0 0 0 1 0 0 0 1 0 0 0 0 1
1 0 0 0 0 1 0 0 0 1 0 0 0 0 0 0 0 0 0 0 0 1 0 0 0 1 0 0 0 0 1
1 0 0 0 0 1 0 0 0 1 1 1 1 1 1 1 1 1 1 1 1 1 0 0 0 1 0 0 0 0 1
1 0 0 0 0 1 0 0 0 0 0 0 0 0 0 0 0 0 0 0 0 0 0 0 0 1 0 0 0 0 1
1 0 0 0 0 1 0 0 0 0 0 0 0 0 0 0 0 0 0 0 0 0 0 0 0 1 0 0 0 0 1
1 0 0 0 0 1 0 0 0 0 0 0 0 0 0 0 0 0 0 0 0 0 0 0 0 1 0 0 0 0 1
1 0 0 0 0 1 1 1 1 1 1 1 1 1 1 1 1 1 1 1 1 1 1 1 1 1 0 0 0 0 1
1 0 0 0 0 0 0 0 0 0 0 0 0 0 0 0 0 0 0 0 0 0 0 0 0 0 0 0 0 1
1 0 0 0 0 0 0 0 0 0 0 0 0 0 0 0 0 0 0 0 0 0 0 0 0 0 0 0 0 1
1 0 0 0 0 0 0 0 0 0 0 0 0 0 0 0 0 0 0 0 0 0 0 0 0 0 0 0 0 1
1 0 0 0 0 0 0 0 0 0 0 0 0 0 0 0 0 0 0 0 0 0 0 0 0 0 0 0 0 1
1 1 1 1 1 1 1 1 1 1 1 1 1 1 1 1 1 1 1 1 1 1 1 1 1 1 1 1 1 1];

```

```

C=Sr2; %Input the Array
figure(1)
for i=1:N
for j=1:N
if C(i,j) == 1
plot(j,i, 'r')
axis([0 N+1 0 N+1])
hold on
elseif C(i,j)==2
plot(j,i, 'g*')
axis([0 N 0 N])
hold on
end
end
end

Y = fft2(C);
Pyy = Y.* conj(Y)/ fnum ;
Pyymax=max(Pyy);
pmax= max(Pyymax);
NormPyy=Pyy/ pmax;
figure(2)
[f,h]=meshgrid(0:F:N*F-F/2,0:F:N*F-F/2);
plot3(f,h, NormPyy);
surf(f,h, NormPyy);
grid on;
d=max(max(f));

y = fft2(C);
Z = fftshift(y);
Pzz = Z.* conj(Z)/ fnum ;
Pzzmax=max(Pzz);
pzmax= max(Pzzmax);
NormPzz=Pzz/ pzmax;

s=max(max(f));
figure(3)
[x,y]=meshgrid(-s/2:F:s/2, -s/2:F:s/2);

```

Appendix B

This appendix gives the main code for beam-forming in this thesis.

Beamformer.m

--Shervin Azad 2010--

```
%%%%%%%%%%%%%%%%%%%%%%%%%%%%%%%%%%%%%%%%%%%%%%%%%%%%%%%%%%%%%%%%%%%%%%%%%
%%%%%%%%%%%%%%%%%%%%%%%%%%%%%%%%%%%%%%%%%%%%%%%%%%%%%%%%%%%%%%%%%%%%%%%%%
%      Conventional beamforming for a Uniform Linear Array (ULA) of Seismic
data
%%%%%%%%%%%%%%%%%%%%%%%%%%%%%%%%%%%%%%%%%%%%%%%%%%%%%%%%%%%%%%%%%%%%%%%%%
%%%%%%%%%%%%%%%%%%%%%%%%%%%%%%%%%%%%%%%%%%%%%%%%%%%%%%%%%%%%%%%%%%%%%%%%%

% Note - The program beamforms the whole diffraction curve

clearvariables
home

% *****
% ----- INPUT DATA INFO -----

fid = fopen('vsp375600.bin');      % Name of DATA FILE eg. 'filename'

rows = 300;                        % Number of time samples
cols = 300 ;                       % Number of traces
thevel = 4500;                     % aver. Vel. for calculation of theoretical
                                % diffractionhyperbols (m/s)

% ----- END OF INPUT INFO -----
% *****

% ----- Some Calculations -----
% time of diffraction apex in seconds
seglens = seglen/tracespace;      % segment length in samples
numsegs = round((cols/seglens)-.5); % number of segments
kn = 1/(tracespace*2);           % nyquist wavenumber
fn = 1/(sr*2);                   % nyquist frequency
% ----- GET THE DATA -----

[A,count] = fread(fid,[rows,cols],'float32');

% ----- CALCULATE THE THEORETICAL DIFFRACTION MOVEOUT -----

xb = 1*tracespace;                % x-value where the hyperbola begins
xo = aloc*tracespace;             % x-value at normal incidence
a=0;
for f=1:300
    a=a+1 ;
```

```

b(1)=0;
t0= 0;
b=0;
t0=t0;
    t1=t0+1;
        t0t = t0*sr;
        t1t=(t1)*sr;

for k=1
for j=1:300
    b=0;

xoff=-a;
xoff= xoff+1;

    t0=t0+1;
    t1=t0+1;
        t0t = t0*sr;
        t1t=(t1)*sr;
        col=300;

fori = 1:col
teta=0
        Dt(i)= t0+(t0t +
0.20*(xoff*xoff*cos(teta)*cos(teta))/(2*thevel*((thevel*t0t)/2))/sr);%top of
        the window

        Dbt(i)= t1+(t1t +
0.20*(xoff*xoff*cos(teta)*cos(teta))/(2*thevel*((thevel*t1t)/2))/sr);%bottom
        of the window
xoff=xoff+1;
        DT(i)= round(Dt(i));
DTb(i)= round(Dbt(i));
        h=DTb(i)-DT(i);

if h>0
for g=1:h
if DT(i)+(g-1)>300
        DT(i)=300 -(g-1);
end
        x(i)=(A(DT(i)+(g-1),i));

        b= b+x(i);
end
        S(i)=b; %sum along the trace

end
end
;
        total(j)=b;

end

```

```
        B(:,f)=total;
    hold on
end

    G=abs(B);
    figure(1)
    pcolor(G)
    shading flat
    hold on
```

Appendix C

The following is a code for determining signal-to-noise ratio.

Signaltonoise.m

--Shervin Azad 2011--

```
clear variables
home

% *****
% ----- INPUT DATA INFO -----

fid = fopen('mm250.bin');           % Name of DATA FILE eg. 'filename'

rows = 300;                         % Number of time samples
cols = 300 ;                        % Number of traces
sr = .00044;                         % aver. Vel. for calculation of theoretical
thevel = 4500;
diffraction hyperbols (m/s)
tracespace = 1;
[A,count] = fread(fid,[rows,cols],'float32');

figure(1);
pcolor(A);
shading flat
hold on
D=awgn(A,25);
figure(2)
pcolor(D)
shading flat
hold on

F=D-A;
figure(23)
pcolor(F)
shading flat
hold on
sum=0;
fori=25:70;
for j=1:300
    sum=(A(i,j))^2+sum;
end
end
noise=0;
fori=25:70;
for j=1:300
    noise=(F(i,j))^2+noise;
end
end
SNR=sum/noise
```

Appendix D

```
#!/bin/sh
#2D (2nd order) finite difference modelling

shotx=600
velfile="VelMod.bin"
shotfile="ShotMod1.bin"
dataname="test2.su"

# Finite difference modeling

    echo Start FD modeling
    echo

#   sufdmod2 < $velfile > /dev/null \
sufdmod2 < $velfile > Wavefile.su \
dx=4 dz=4 \
nx=300 nz=300 \
fmax=50 \
xs=$shotx \
mt=8 \
zs=4 \
hsz=0 \
tmax=2 \
abs=1,1,1,1 \
hsfile=$dataname \
verbose=1
    echo
    echo FD modeling complete
    echo

#   cat $shotnum.su >> movie.su

# Resample the seismogram
suresamp < test1.su nt=600 dt=0.001 | sushw key=tracr a=1 b=1 >
test.resamp
#   suchw < $shotnum.resamp key1=ns a=600 > temp.su
    echo resample complete
    echo

# Convert to segy
#segyhdrs < movie.su
#segywrite endian=0 tape=VSPData.sgy < movie.su

date
suxmovie < Wavefile.su n2=300 title="frame=%g" loop=1 clip=0.05
exit 0
```





